1168

Microstructural Design and Thermal Stability of Rapidly Solidified, High Strength, High Conductivity Copper Alloys

Thesis submitted in suplication for the degree of Docteur ès Sciences

At the Institute of Structural Metallurgy,
University of Neuchâtel

By
Emad EL BATAWI
ing. Matériaux EPFL

Thesis director: Prof. D.G. Morris
Jury: Prof. W. Benoit
Prof. W. Form
Prof. B. Ilschner
Dr. P. Isler

Feb. 1991

Microstructural Design and Thermal Stability of Rapidly Solidified, High Strength, High Conductivity Copper Alloys

Thesis submitted in suplication for the degree of Docteur ès Sciences

At the Institute of Structural Metallurgy,
University of Neuchâtel

By
Emad EL BATAWI
ing. Matériaux EPFL

Thesis director: Prof. D.G. Morris
Jury: Prof. W. Benoit
Prof. W. Form
Prof. B. Ilschner
Dr. P. Isler

Feb. 1991

IMPRIMATUR POUR LA THÈSE

Conception et stabilité thermique des microstructures d'alliages cuivreux de haute résistance mécanique et haute conductivité préparés par la solidification rapide

de Monsieur Emad El Batawi

UNIVERSITÉ DE NEUCHÂTEL

FACULTÉ DES SCIENCES

La Faculté des sciences de l'Université de Neuchâtel sur le rapport des membres du jury,

Messieurs D.G. Morris, W. Form, W. Benoît (EPF-Lausanne), B. Ilschner (EPF-Lausanne) et P. Isler (Reconvilier)

autorise l'impression de la présente thèse.

Neuchâtel, le 26 septembre 1991

Le doyen :

Cl. Mermod

To My Friends and Family

...a friend is one who knows, without having to ask, that you need help

Table of Contents

CHAPTER 1
Preamble

1. Preamble

Copper and its alloys are widely used for their high electrical and thermal conductivity, good formability and high corrosion resistance. During the past fifty years there has been a steady demand for high conductivity alloys that show high strengths at room temperature as well as retain their strengths and ductility when exposed to elevated temperature. Such alloys, destined for applications in the microelectronics, electrical, nuclear and aerospace industries are being developed and new production methods are being tested.

Alloying additives impair the conductivity of copper, depending on the solute. Strengthening mechanisms which do not considerably alter the conductivity are based on dispersion or precipitation strengthening, grain refinement or cold working. Commercially available alloys having the required combination of strength and conductivity are either thermomechanically treated precipitation hardened or oxide dispersion strengthened materials. Figure I.1 illustrates the electrical and mechanical properties of some of these materials.

Rapid solidification of alloys may result in: a) a metastable extension of solid solubility of alloying elements which may be subsequently employed to create a high volume fraction of finely distributed precipitate particles, b) refinement of the scale of segregation cell structure, producing a homogeneous distribution of poorly soluble dispersoid particles, c) refined grain size by which strengthening may occur and; d) the production of metastable phases.

Rapidly solidified products are in the form of powder, flake, ribbon or fibre. The production of monolithic materials from these products requires a consolidation procedure, for example extrusion. The precipitation and coarsening kinetics of the strengthening particles during this processing step, generally carried out at intermediate or elevated temperatures, will determine the thermal stability of the material. These particles play a direct role in determining mechanical properties as obstacles to dislocation motion and indirectly by impeding grain boundary movement and thus maintaining a refined microstructure. Consequently it is the stability or coarsening resistance of these strengthening particles that is of great interest.

The purpose of this study is to characterize the rapid solidification of copper alloys, with particular attention to the mechanisms which control the microstructure and thermal stability. Furthermore, this work attempts to develop criteria for the choice of alloying element additions for high strength and conductivity, bearing in mind the demands imposed by rapid solidification processing. The nature and distribution of the strengthening phase, the casting conditions and the alloy composition may synergistically affect the overall behaviour of the alloy.

Figure I.2 shows an organization chart for this research work. Basic metallurgical models that enable the understanding of rapidly solidified microstructures, hardening mechanisms and thermal stability are used to choose

alloying additions. Analysis of the data obtained from the microstructural and mechanical property characterization, of the different rapidly solidified experimental alloys, will determine the applicability of the models initially employed and promote the understanding of these new materials. Reevaluation of these metallurgical models will also enable the establishment of new criteria for solute choice and casting conditions.

The specific topics of interest are: (a) solute distribution, where depending on the solute and the casting conditions, either a metastable solid solution or a microsegregated microstructure may be obtained, (b) grain structure, where casting conditions and solute additions modify the nucleation and growth kinetics of the grains, resulting in different growth morphologies in different portions of the rapidly solidified ribbon, (c) mechanical properties, where the grain and particle size and distribution determine the strength of the material; and (d) thermal stability, where dislocations and grain boundaries as well as the size and distribution of second phase particles influence the evolution of the microstructure with temperature.

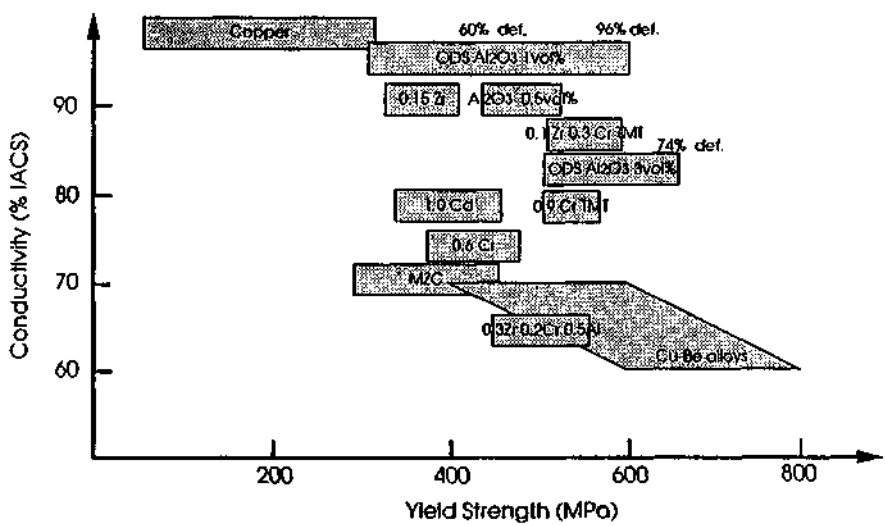

Figure I.1 Conductivity* and strength of some high strength, high conductivity copper alloys.

*International Annealed Copper Standard- where the conductivity of annealed pure copper is taken as 100% IACS (resistivity of $1.72 \times 10^{-6}\ \Omega$ cm).

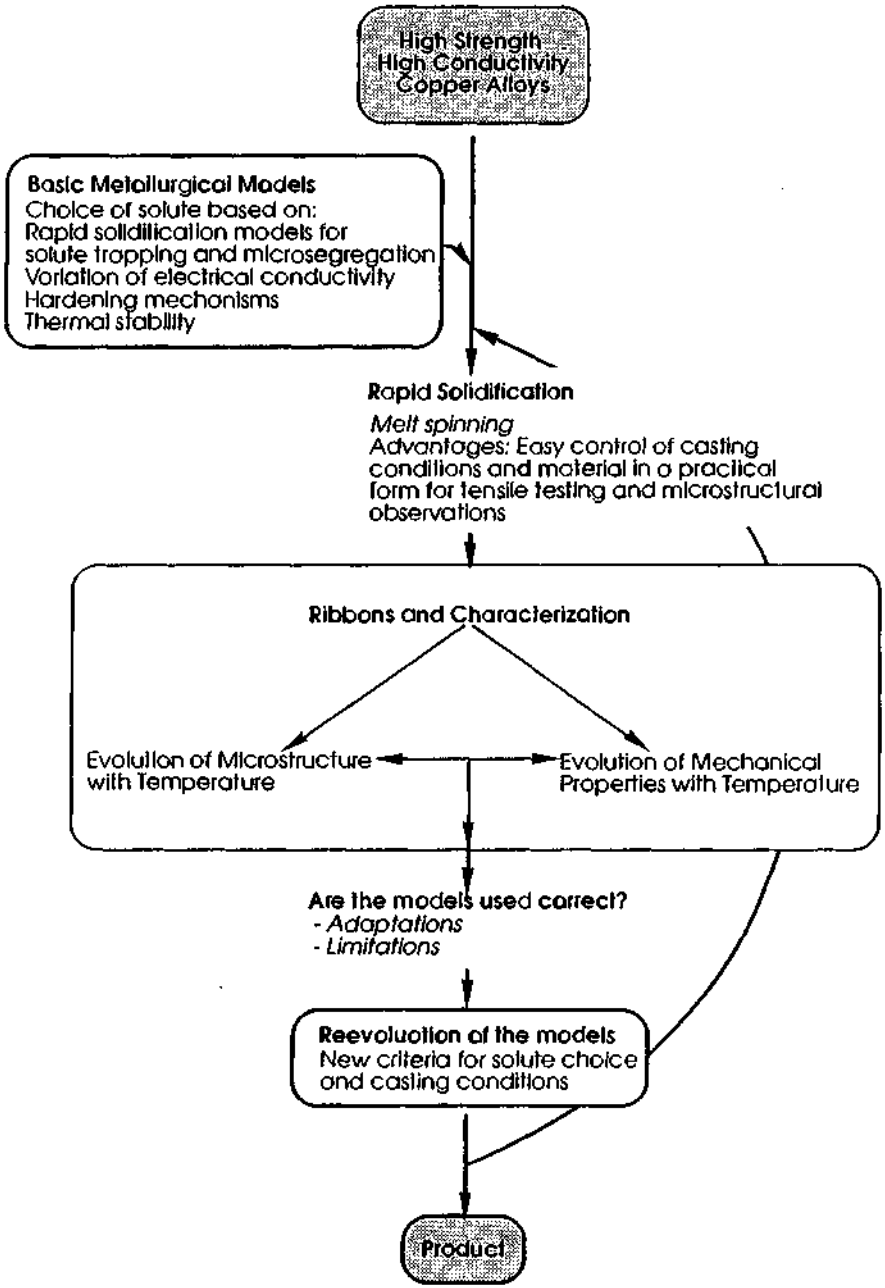

Figure I.2 Organization chart for this research work

CHAPTER 2

Introduction and Literature Review

2. Introduction and Literature Review

The opportunities offered by rapid solidification call for a reevaluation of the criteria of solute choice. Alloying element additions avoided in conventional ingot metallurgy because for example of marked segregation may be used when rapidly solidified. The choice and concentration of solute will depend on the conductivity and the strength desired, the type of strengthening mechanism, the consolidation conditions available and the rapid solidification process envisaged. The material characteristics selected here were conductivities and room temperature flow strengths of final material better than 80% IACS and 500 MPa; with strengthening predominantly by precipitation or dispersion hardening. Industrial requirements for consolidation at temperatures above 600°C meant that the thermal stability of the rapidly solidified material should be reasonable.

Melt spinning will be used as a means of obtaining small quantities of rapidly solidified material, allowing the behaviour of different solutes to be evaluated. This technique will help determine the rapidly solidified microstructures that might be obtained by other rapid solidification techniques such as powder atomization. Microstructural examination and tensile testing after heat treatment of rapidly solidified ribbons will be used to asses the thermal stability of the alloy.

This chapter reviews previous findings on the development of high strength, high conductivity copper alloys. This will help present a preliminary assessment of rapid solidification as a new production method for such materials. This will be followed by a review of the criteria necessary for the development of such materials, which include: (a) restricting effects of solutes on conductivity of copper, (b) solubility extension by rapid solidification, (c) mechanisms determining the strength of dispersion hardened alloys and; (d) thermal stability.

2.1 High strength high conductivity copper alloys

Copper-rich alloys have had increasing applications in the microelectronic, mechanic, electric and aerospace industries where high strength and conductivity are required. Resistance welding electrodes, wires or leadframes for microcircuits, high voltage switches, motor commutators, continuous casting molds and heat exchangers are some of the important applications [1,2]. New applications for these alloys such as fusion reactor walls [3], water cooled gas turbine blades [4] and targets for neutron irradiation [5] are also being pursued.

This wide range of applications requires performances that many of the available copper alloys may not satisfy (figure I.1). There is therefore a need for the development of such alloys by production techniques offering opportunities that classical metallurgy does not. Rapid solidification can be used for its ability to refine microstructure and extend solubility. Thermal stability is clearly important in this case since the high strengths procured by the strengthening particles, finely

dispersed by rapid solidification, must resist the temperatures involved during the necessary hot consolidation of the rapidly solidified material.

Traditional high strength copper alloys produced by conventional ingot metallurgy rely on precipitation hardening for their strength. While this method can provide exceptional strength levels after intermediate (~400°C) temperature anneals, the solutes generally employed do not provide the necessary thermal stability for the high temperatures encountered during consolidation of rapidly solidified material. Because of the advantages of rapid solidification, a wider variety of solutes with the potential of producing thermally stable microstructures can now be examined, such as solutes avoided in ingot metallurgy because of their segregation during casting. Classical solutes introduced in higher volume fractions can also be tried. In the latter case it is hoped that the loss in strength resulting from consolidation is more than compensated by the larger volume fraction of dispersion introduced by rapid solidification.

In addition to precipitation strengthening, oxide dispersion strengthening has been applied to the production of high strength high conductivity copper. Dispersions such as Al_2O_3, Be_2O, SiO_2, TiO_2 and ZrO_2 have been introduced by internal oxidation of either the binary alloy powders or bulk material. Oxide dispersion strengthening has been used alone or in combination with precipitation strengthening to attain high strength and conductivity levels. However the processing of these materials requires long, delicate and costly internal oxidation of the solute. Rapid solidification may offer the possibility of finely distributing dispersions having stabilities approaching to those obtained by internal oxidation.

2.1.1 Precipitation hardened alloys

Beryllium, cadmium, chromium, cobalt, iron, magnesium and zirconium have been used, alone or in combination, as alloying additions for the precipitation hardening of copper. Their solid solubility varies with temperature such that a reasonable volume fraction can be dissolved at high temperatures. A fine dispersion of precipitated particles can be obtained by quenching and aging the solutionized material.

The maximum solubility of chromium, quoted by Chakrabarti and Laughlin [6], is 0.89^{at}% at 1076.6°C, its solubility decreases with temperature to 0.03^{at}% at 400°C. Conventional ingot metallurgy has been used to produce high strength, high conductivity copper-chromium alloys with up to 0.9^{at}% chromium. These alloys are generally thermomechanically treated. Solutionizing is carried out at 950-1050°C. After quenching they are work hardened and aged between 300-500°C to obtain the best combination of strength and conductivity [7].

The precipitation of chromium from supersaturation has been extensively studied by several authors. Williams [8], using X-ray diffraction, suggested that the first stage of precipitation consisted in the formation of thin chromium plates

coherent on $(111)_{Cu}$ planes. Thereafter competitive growth of the particles, partial loss in coherency and transformation to a bcc crystal structure took place. These transformations all occurred near peak aging. Suzuki and Kanno [9] showed that if deformation was carried out after solutionizing, precipitation kinetics were modified because of heterogeneous nucleation on dislocation lines.

The addition of other alloying elements to the binary copper-chromium system has been envisaged in order to refine the microstructure by influencing grain size or precipitation. Through conventional ingot metallurgy techniques, it was found that the addition of magnesium, arsenic, or zirconium, alone or in combination, enhanced the age hardenability of the binary system [10-13]. Many of the recent studies have been done on the most promising copper-chromium-zirconium alloys. Zirconium additions can be solutionized at 980°C, and during subsequent aging can contribute to the strengthening by supplementary precipitation of zirconium rich particles. It was found that under the same conditions, the zirconium and chromium-rich precipitates were finer and more densely distributed in the ternary alloy than the individual precipitates in each of the binary alloys [14], proving some type of synergism between the alloying elements and leading to superior strengths. The mechanical properties of these alloys were also found to be sensitive to different thermomechanical treatments. Prior deformation in the solutionized state increased considerably the peak hardness of the alloy, while aging in the undeformed state with zirconium additions had little effect on age hardenability [15].

Commercial AMAX-MZC (Cu-Cr 0.5^{at}%-Zr 0.1^{at}%-Mg 0.13^{at}%) is produced by conventional ingot metallurgy as an age hardenable alloy having a conductivity of 80% IACS and a tensile strength of 550-620 MPa [16]. Even though the mechanical properties of most of these alloys can be improved by various alloying additions or by thermomechanical treatment, their strengths are limited by the volume fraction of dispersion that can be put into solution. To the extent that the volume fraction can be increased by rapid solidification, experiments will be carried out that demonstrate this effect.

The effect of rapid solidification by melt spinning on the enhancement of solid solubility of chromium in copper has been studied by Morris and Morris [17] and by Tenwick and Davies [18] for binary alloys containing up to 5^{at}% chromium. Both studies showed that the solubility of chromium could be extended. Depending on the ribbon thickness the maximum solubility extension observed was approximately 3^{at}%. At higher chromium concentrations, in 30 µm thick ribbons, primary chromium particles were found. These particles were deduced to arise by a uniform, primary solidification mode prior to, and independent of, the nucleation and growth of the copper crystals. The grain size increased from 0.9-2.1 µm and 0.6-1.2 µm from bottom to top of the 2 and 5^{at}% chromium ribbons respectively [17]. On annealing, the concentrated ribbons presented a bimodal

particle distribution of fine precipitates and coarse primary particles. Prolonged heat treatment resulted in the dissolution of the fine precipitates into the larger particles [19]. The flow strength of the peak aged material was measured to be 605 MPa and 760 MPa for the Cu-Cr 2^{at}% and Cu-Cr 5^{at}% ribbons respectively [17]. Conductivities ranging from 50-80% IACS, depending on the solute concentration, were measured by Tenwick and Davies [18]. Microhardness measurements were also carried out, a value of 400 H_v was obtained for peak aged Cu-Cr6.4^{at}% melt spun ribbons.

Rapidly quenched dilute Cu-Cr0.38^{at}%-Zr0.2^{at}% powders were nitrogen gas atomized by Sarin and Grant [15, 20]. The powders 150 μm in size showed a dendritic microstructure with a dendrite arm spacing of 6 μm, corresponding to a cooling rate of 10^3 to 10^4 Ks^{-1}. They were degassed, compacted in copper cans and hot extruded with a reduction ratio of 25:1 at 650°C. A yield strength of the consolidated material of 240 MPa and a conductivity of 82% IACS was obtained. The material also showed good thermal stability, retaining most of its room temperature properties after exposure at 400 to 800°C. This was partially attributed to grain size stabilization due to grain boundary pinning oxide particles.

It is clear from the above findings that chromium-containing systems might offer improved strength and conductivity when processed by rapid solidification. However detailed consideration of the microstructural changes of these rapidly solidified alloys have not been studied.

The copper-zirconium phase diagram is reasonably well established [21]. The composition of the first intermediate phase in copper-rich alloys, Cu_5Zr, forms peritectically from the congruently melting Cu_4Zr. The solubility of zirconium varies rapidly with temperature, at 950°C its maximum solubility is 0.11^{at}%, dropping to 0.038^{at}% at 838°C [21]. In rapidly solidified copper-zirconium microcrystalline alloys other nonequilibrium precipitates were found in the as cast condition, such as Cu_9Zr_2, $Cu_{3.6}Zr$ and Cu_8Zr_3 [23]

Saarivirta [24] obtained tensile strengths of 405 to 480 MPa and electrical conductivities of 80 to 93%IACS on Cu-0.035 to 0.11^{at}% Zr alloys that have been solution-annealed, cold worked 90% and aged 1 h at 400°C. The high temperature properties of the zirconium-containing alloys processed by classical ingot metallurgy were found to be superior to the binary chromium-containing alloys [25]. These alloys were also shown to maintain most of the strength derived from cold working at temperatures up to 400-450°C.

The precipitation of the copper-zirconium intermetallic was studied by Phillips [26]. Heterogeneous nucleation of fine particles on stacking faults generated during aging at 500°C in partially recrystallized areas occurred. No faults were observed in samples that were heavily cold rolled before aging. Very fine precipitate platelets formed at dislocations and recrystallization was significantly retarded. TEM

observations showed that the precipitate platelets were parallel to $\{111\}_{Cu}$ and showed no evidence of coherency strain fields.

The rapid solidification of copper-zirconium alloys was studied by several authors. Arnberg *et al.* [22] showed that the solubility of zirconium can be extended to 0.35^{at}% by ultrasonic helium gas atomization while Tenwick and Davies [18] showed that by melt spinning the metastable solubility of zirconium could be extended to 1.3^{at}%. The yield strength of the canned and extruded powder (at 600°C) was found to be 406 MPa with an electrical conductivity of 91% IACS [22], while the microhardness of peak aged melt spun ribbons reached 340 H_V after 1 h at 400°C with conductivities of 45% IACS [18].

Spray formed copper-zirconium deposits containing up to 0.6^{at}% zirconium have been studied by Cheng *et al.* [27], and, Singh and Lawley [28]. Because of the finer and greater homogeneity in microstructure obtained by the spray forming process, these materials showed superior properties with respect to similar compositions processed by ingot metallurgy. A grain size of less than 40 μm was obtained, with 2 μm Cu_5Zr particles decorating the boundaries. This phase was unaltered during thermomechanical treatment. After aging the deposited material at 400°C for 15 min a yield strength of 524 MPa and a conductivity of 82% IACS was measured [28].

As for the copper-chromium, copper-zirconium systems processed by rapid solidification show great promise.

Rapid solidification of copper-beryllium-based alloys has shown to be detrimental to strength. Nishi *et al.* [29, 30] reported that in a commercial grade of copper-beryllium-cobalt alloy the peak aging time for the rapidly solidified material was longer than for conventionally quenched alloys. The primary strengthening phase in copper-beryllium-based alloys is the metastable γ' phase. The γ phase is the stable ordered bcc precipitate. In the rapidly solidified material the formation of γ' was found to be suppressed and that of γ, enhanced. The reasons were: (a) large concentrations of quenched-in vacancies which prevent the cobalt atoms from accelerating the precipitation of γ' and; (b) large γ precipitates in the as cast material denuding their immediate surrounding of alloying elements. If the rapidly solidified material is solution treated, quenched and aged, the hardness values obtained were superiour.

Köster and Caesar reported that alloying additions decreased the grain size and the thickness of melt spun ribbons under identical processing conditions [31]. For copper-nickel and copper-iron alloys [23] the microstructure was dependent on the velocity of the quenching substrate as well as the melt ejection temperature. For velocities of 20-30 ms^{-1}, or low melt temperatures, large equiaxed grains were observed in the transverse section of the ribbons. At intermediate velocities three types of grains were seen: (a) a zone of chill crystals on the wheel contact side, (b) a central zone of columnar grains and; (c) a layer of equiaxed crystals near the top

surface. Wheel speeds of 40 ms^{-1} resulted in columnar grains extending throughout the ribbon cross section.

Table II.1 gives the maximum metastable solubility extensions obtained by rapid solidification of some binary alloys. The extension of solubility were found to vary with quench rate and dimensions of the rapidly solidified product as reflected by the lower values of solid solubility extension reported for chromium (2^{at}% [17]) and zirconium (0.5^{at}% [22]).

Table II.1 Solid solubilities of some elements in conventionally and rapidly solidified (melt spun) condition in copper

Alloy system	Max. equilibrium solubility (^{at}%)	Temperature (°C)	Metastable solubility (^{at}%)	references
Cu-Co	5.1	1112	15	21, 33
Cu-Cr	0.89	1077	3.32	6, 18
Cu-Fe	4.8	1094	20	21, 31, 34
Cu-Sn	9.1	586	15	21, 35
Cu-Ti	8	885	9	21, 32
Cu-Zr	0.1	977	1.33	21, 18

2.1.2 Dispersion hardened alloys

Dispersion strengthening offers a means of strengthening at temperatures where precipitation hardened materials become ineffective. Schilling and Grant [36] showed that oxide dispersions in copper are effective to temperatures up to 1000°C. The process involves making a homogeneous alloy containing the stable oxide-forming solute usually in solid solution (*e.g.* aluminium, beryllium, silicon) and precipitating the oxide as oxygen is diffused into the material [37]. Because of economic considerations, the time during which internal oxidation takes place must be limited. It is for this reason that the powder metallurgy route has proven to be the only practical method of manufacturing oxide dispersion strengthened copper. Wire or strip thicker than 0.25 mm are unpractical [38, 39].The internal oxidation of various binary solid solution copper alloys was studied in detail by Rhines [37]. Copper-alumina and copper-silica internally oxidized alloys containing 3.5^{vol}% and 2.1^{vol}% oxide had a room temperature yield strengths of up to 490 MPa and 240 MPa respectively and conductivities of 65% IACS [40]. The softening of these oxide dispersion strengthened materials was found to be pushed to higher temperatures as shown by the tensile strengths of cold worked ZrO_2-containing alloys containing 1.3^{vol}% dispersion, where the strength of the as drawn material was 600 MPa, and after 1 h at 800-1000°C, decreased to 450 MPa [39]. The electrical conductivity of the material was 90% IACS.

Grant *et al.* [1] studied rapidly solidified powders which contained alloying elements that permitted the combination of both precipitation and oxide dispersion

strengthening. Because the powders were rapidly quenched, they attained both extended solid solubilities as well as highly homogeneous and refined structures. The former advantage being quite important due to the limited solid solubility of some of the alloying elements used associated with high conductivity copper alloys. The high surface area of the rapidly solidified powders made them susceptible to surface oxidation even at room temperature. Surface oxidation during processing was good enough to oxidize the reactive elements such as aluminium, titanium or zirconium. Any copper oxide formed during processing was reduced in hydrogen before consolidation. Surface oxidized copper-chromium-zirconium-aluminium alloys showed remarkable thermal stability. The yield strength of the as extruded material was 476 MPa, after annealing at 950°C for 1 h the drop in strength was only of 20 MPa. Its conductivity was measured as 60% IACS.

The structural refinement associated with rapid solidification permits the use of elements which normally result in segregation by conventional ingot metallurgy. Dispersoids that are soluble in the liquid can be introduced in a microsegregated manner in the solid, resulting in a dispersion hardened material. The copper-manganese-boron system which was recently studied [41], showed that several manganese borides formed depending on the composition of the alloy. The dispersions were fine in size and were distributed on the solidification cell boundaries of the melt spun material. The flow strength of the as cast ribbons ranged from 280-680 MPa for 0.76-5.50^{vol}% dispersion. Copper-intermetallic dispersion hardened systems have also been studied. Melt spun ribbons of copper containing Cr_2Nb intermetallic particles were cast, chopped and compacted before hot rolling to produce fully dense sheet product [42]. The tensile strengths were tested over a temperature range of 25-850°C. Yield and ultimate tensile strengths were in excess of 250 MPa at 25°C and remained in excess of 100 MPa up to 750°C. Other microsegregated dispersion hardened copper alloys based on the copper-boron system produced by melt spinning have been studied. The solid solubility of boron was increased to approximately 4^{at}% in the wheel contact side of the melt spun ribbons where the microhardness reached 600 H_v after annealing 2 h at 600°C [43]. Ribbons having a near eutectic composition (13.3^{at}% boron) consisted of three zones: (a) a microstructure which was thought to be the result of devitrification during solid state cooling of an amorphous structure near the wheel side, (b) a cellular and; (c) a dendritic microstructure on the top portion of the ribbon. Concentrated copper-nickel-metal-boron alloys containing 20-40^{at}% solute were melt spun by Panchanathan [44]. In the as cast state the ribbons were fragile, after heat treatment at 760°C for 2 h their ductility increased, different metal borides formed and hardness values, ranging from 200-500 H_v were measured. Yefinov *et al.* studied the influence of cooling rate and subsequent annealing on the microstructure and hardness of copper alloys containing 1-60^{at}% solute [45]. Critical cooling rates were necessary to suppress peritectic and monotectic reactions.

At higher cooling rates, the mutual solubility of the components increased. The microhardness of the as cast material increased with quench rate and decreased with increasing annealing time at 400°C (all but the Cu-Zr3^{at}%, Cu-Cr6^{at}% and Cu-Si12^{at}% ribbons where microhardness increased with annealing time up to 150, 200 and 300 H_V respectively after 5-10 h at 400°C).

Stable dispersions have been introduced in copper by either blending [46] or mechanically alloying mixtures of copper and dispersoid powders [47-49]. Mechanical alloying of slightly soluble additions such as chromium and niobium were found to be more quickly and finely dispersed than the stable less reactive additions such as diboride particles. Some of these materials showed fairly good resistance to softening. The yield strength of mechanically alloyed, compacted and extruded at 700°C Cu-Nb 5^{at}% was 1250 MPa; after annealing for 1 h at 1000°C the strength dropped to 940 MPa. It was suggested that the mechanical alloying of copper-dispersion systems is capable of distributing larger quantities of poorly soluble materials, the scale of refinement depending on the ease of particle break-down. Rapid solidification was found to be in some cases limited by the non-uniformity in particle distribution once a critical solute concentration is exceeded.

The mechanical properties, means of production and electrical conductivity of some rapidly solidified alloys are given in table II.2. It is apparent that copper-chromium and copper-zirconium precipitation hardened alloys exhibit better mechanical strengths and conductivities. The multiple strengthened alloys exhibit very high strength characteristics, however, their conductivities are relatively low.

2.2 Solute choice

This section establishes guide-lines that may help in the choice of solute for high strength high conductivity alloys. The solutes chosen should have the following characteristics:

(a) a low equilibrium solubility and a minimal effect on the conductivity of copper.

(b) the potential of producing a large volume fraction of finely dispersed particles in the consolidated material, by either:

(i) Precipitation hardening*; solutes will be chosen in order to achieve solubility extension by rapid solidification. The time temperature treatments during consolidation are equivalent to an aging treatment, however, it is hoped that the resultant microstructure will have a sufficiently large volume fraction of particles to compensate for the loss in strength due to over-aging, or;

*In the context of this study, rapidly solidified precipitation hardened alloys are materials where the strengthening phase is the result of precipitation from a metastable solid solution.

Table II.2 Mechanical and electrical properties of some rapidly solidified copper alloys

Alloy comp. in at%	Y.S. MPa	T.S. MPa	%IACS	Process route	ref.
Cu	167	177	-	Taylor wire, wire diameter 10 μm and grain length 1.15 mm	50
Cu-Cr 2	568	605	-	Tensile testing of melt spun ribbon in the peak aged state	17
Cu-Cr 5	760	760	-	Tensile testing of melt spun ribbon in the peak aged state	17
Cu-Cr 5	415	490	70	Extrusion at 700°C of rapidly solidified flake	19
Cu-Zr0.35	406	460	91	Extrusion at 600°C of ultrasonic helium gas atomized powder	22
Cu-Zr0.56	324	417	91.2	Extrusion at 650°C of nitrogen gas atomized powder	20
Cu-Ni 5.4-Ti 3.3 (1vol% TiO_2)	745	815	25	powder atomized, attrited, surface oxidized, hot extruded, solutionized at 950°C and aged at 575°C	1
Cu-Zr 0.2-Cr 0.27-Al 1.2 (1vol% Al_2O_3)	455	503	64	powder atomized, attrited, surface oxidized, hot extruded, solutionized at 950°C and aged at 575°C	1
Cu-Al 1.4 (2.9vol% Al_2O_3)	471	486	-	gas atomized, internally oxidized and extruded at 760°C	36

(ii) Dispersion hardening# ; the solutes will be chosen such that rapid solidification results in a fine distribution of microsegregated stable particles. The particles should be sufficiently stable to enable hot consolidation with minimal microstructural changes.

(c) Low diffusivity to ensure reasonable thermal stability.

The effect of solutes on conductivity is presented in section 2.2.1. Solute diffusivity in copper will be reviewed in section 2.2.2. The prediction of solubility extension in view of the production of precipitation hardened materials is covered by section 2.2.3 and solute choice for the production of dispersion hardened materials is discussed in section 2.2.4.

2.2.1 Conductivity

Electrical conductivity of alloys depends on type and the concentration of solute in solid solution, the lattice strains due to defects such as vacancies, dislocations

Rapidly solidified dispersion hardened alloys are materials where the strengthening phase (dispersoid) is the result of microsegregation during solidification.

and grain boundaries, and the volume faction of second phase particles. The spatial distribution of these particles and the nature of their interface also play an important role. It has been shown that grain refinement and cold working provide strengthening with little decrease in conductivity [51, 52]. For this reason the final process usually carried out in strengthening copper alloys is cold working. Solutes, such as zinc have been added to reduce the stacking fault energy of the material thereby promoting its work hardening characteristics, however, the presence of such elements decreases conductivity [53].

Figure I.1 showed that strength and conductivity are inversely related. Precipitation and dispersion hardening provide better possibilities than solute hardening when considering strengthening mechanisms that do not affect conductivity. The solute and its solubility in the matrix as well as the nature and the volume fraction of strengthening phase will play an important role in determining the conductivity of the material. An incoherent particle-matrix interface will be preferred since matrix strains will be reduced, and if the volume fraction of second phase particles is limited to less than 5^{vol}%, the conductivity of the alloy will only be slightly affected.

Table II.3 lists the solubilities at 200°C [21] and the increase in resistivity per atomic percent solute in copper [54] for various alloying elements. The last column shows the product of the solubility and increase in resistivity. It is clear that the linear approximation of the increase in resistivity does not hold for concentrated solid solutions. However, the value of this product gives an idea on the solutes to be avoided in developing high conductivity alloys. For a given admissible increase in resistivity due to solute solubility in the matrix, for example 0.2 μΩcm which corresponds to a drop in conductivity of 10% IACS, alloying elements can be chosen. Under these conditions it is shown that all insoluble solutes may be used without much modification in conductivity. Solutes such as selenium and sulphur are known to be detrimental to the ductility of the alloy, resulting in brittle grain boundary fracture and should therefore be avoided. Lead, silver, boron and chromium can be used as alloying additions because of their low equilibrium solubility and effect on conductivity of copper. The increase in resistivity due to zirconium additions is small and it may also be considered a possible alloying addition (section 2.1.1, page8). It should also be noted that the solubility of an element can be greatly modified by the formation of a stable dispersoid. For example, the solubility of nickel can be reduced by addition of another solute such as boron. Nickel boride is precipitated, this compound has a lower solubility in copper and reduces the concentration of nickel in solution.

Because of the difficulty in measuring conductivity of thin melt spun ribbons, no conductivity measurements were carried out in this study. However, if the conditions established above are followed, the conductivity of the alloys studied in this work can be expected to be close to 80% IACS.

Table II.3 Solubility and the increase in resistivity per atomic percent of solute in solid solution

Solute	Solubility at approx. 200°C (at%)	Increase in resistivity ($\mu\Omega cm/at\%$)	Product (see text)
Ca	(0.0)*	(0.3)	(0.0)
V	(0.0)	(0.6)	(0.0)
Te	(0.0)	(8.4)	(0.0)
Se	(0.0)	(10.5)	(0.0)
Q	0.001	5.3	0.005
S	0.001	9.2	0.009
Pb	0.01	3.3	0.033
Ag	0.06	0.6	0.036
B	0.06	1.4	0.084
Cd	0.3	0.3	0.09
Cr	0.03	4.0	0.12
Fe	0.1	8.5	0.85
Be	1.4	0.65	0.91
Co	0.24	6.9	1.66
Sn	0.7	3.1	2.17
Mg	4	0.8	3.2
P	1.2	6.7	8.0
Zn	30	0.3	9.0
Sb	2.0	5.5	11
Ti	1.0	16	16
Al	18	0.95	17.1
Si	8	3.1	24.8
As	7	6.7	46.9
Mn	24	2.9	69.6
Ni	100	1.1	110

2.2.2 Diffusivity

Analogous to self diffusion, impurity diffusion can be written as an Arrhenius type relation:

$$D_2 = D_{o2}\, exp\left(\frac{-Q_2}{RT}\right) \qquad (1)$$

where D_{o2}, is the frequency factor, Q_2, is the activation energy, R is the universal gas constant and T is the temperature [55]. During the past twenty years numerous models for the calculation of Q_2 have been proposed. Many of the models are

*The values in parentheses represent experimentally insoluble solutes.

derived from the initial models developed by Swalin [56] Turnbull [57] and Lazarus [58], respectively based on the elastic, thermodynamic and electrostatic properties of the diffusing species and the solute atoms. Lazarus' model, modified by LeClaire [59] to include the interaction effects between solute atoms, proposes that the activation energy for transport is based on the electrostatic interaction between an impurity and a vacancy. Q was related to the electrostatic interaction between the excess charge of the impurity and the two half vacancies which flank it at the saddle point. The effective charge difference between solute and solvent ions is the central parameter of the model. Turnbulls' model for the determination of Q_2 is based on thermodynamic parameters of the solute and solvent atoms. With these ideas, Neumann and Hirschwald [60] proposed a model based on the melting points of the pure solute and solvent metals.

Swalin, used the elastic properties of the solvent and solute to develop a model for vacancy controlled solute diffusion [56]. The enthalpy of movement of a solute atom from a normal lattice site into the saddle-point position adjacent to the vacant site is calculated. The solute atom is considered to behave as an elastic sphere, and thus, part of the enthalpy of movement is assumed to result from the hydrostatic compression of the solute atom and part from the dilatation of the constriction at the saddle point. An equation is derived for Q_2 in terms of the Goldschmidt radius of the solute and the compressibilities of the solute and solvent. Neumann and Beke [61] proposed another half empirical model which permits the calculation of Q with the aid of the bulk moduli of the pure solvent and solute metals.

All the models described above permit to estimate the activation energy for transport of the solute atoms in close packed structures where the diffusion is controlled by a vacancy mechanism. These models are in close agreement with experimental results for some solutes and not for others, the solutes being different for the different models. In this work, Swalins' model based on the Goldschmidt radii and bulk moduli to predict the activation energy for bulk diffusion is used, for it was demonstrated that the calculated and experimental activation energies of many solutes in copper were in good agreement [56]. Figure II.1 shows the results of the calculation as well as the experimentally observed [62, 63] activation energies as a function of atomic number. It can be seen that the periodic trend of the elements is observed. In all cases, except for the activation energy of cerium (atomic number 58), the calculated and the predicted values are within close to 20 $kJmol^{-1}$. It was observed by Badrinarayanan and Mathur [64] that the diffusion of rare earth metals in copper takes place with unusually low diffusion coefficients. The low diffusivities were primarily due to remarkably low frequency factors; $2x10^{-12}$ m^2s^{-1} as compared with the generally observed $(0.1\text{-}1)x10^{-4}$ m^2s^{-1} for bulk diffusion in any metal. The low value of the activation energy that they measured, found in figure II.1, as well as the frequency factor for cerium would suggest that the diffusivity measured by the authors is due to pipe and not bulk diffusion.

Since the frequency term for most solutes in copper can be predicted to one order of magnitude, the diffusivity of any alloying element can be estimated with reasonable accuracy. As will be shown in section 2.4, page 26, particle growth depends on the diffusivity of the rate controlling solute. Considering various properties of solutes such as diffusivity, solubility and effect on conductivity, calcium, cerium, chromium, niobium, yttrium and zirconium were selected as solute additions for precipitation hardening.

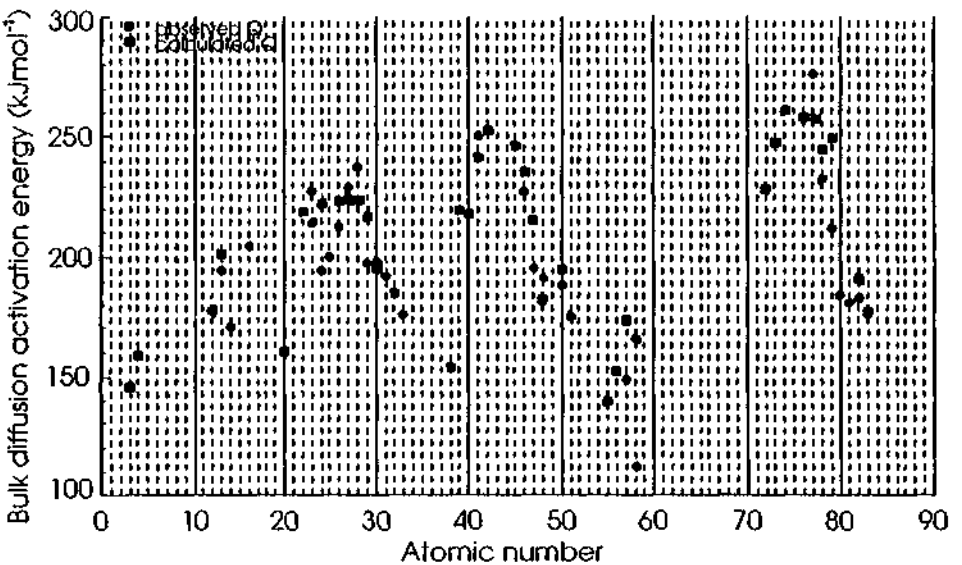

Figure II.1 Activation energies of bulk diffusion of various solutes in copper; calculated (using Swalins' model) and experimental [62, 63]

2.2.3 Solubility extension

Solubility extension by means of rapid solidification depends on the kinetics of rapid solidification and will occur under specific thermodynamic constraints. The following sections will review these conditions.

2.2.3.1 Thermodynamic conditions for partitionless solidification

There are thermodynamic conditions which must be satisfied in order to have a solid with the same composition as the liquid. These conditions were first described by Baker and Cahn in 1971 [65]; the temperature of the interface between the

homogeneous, unsegregated solid and liquid during solidification must be below a critical temperature, T_o. At this temperature both the solid and liquid phases have the same free energy. It is regarded as the highest temperature at which the solid can form with the same composition as its melt. The next section shows that such interface temperatures are not necessary to obtain solute trapping, but the evolution of the T_o line with composition can help determine the ease at which solubility extension may occur.

For a given composition if the liquidus and T_o lines are close, solid solution extension is thermodynamically possible, provided that the melt is undercooled below T_o during solidification. However, when the T_o curve plunges at low solute concentrations, solubility extension becomes thermodynamically impossible. This is usually encountered in systems where the liquid shows large positive deviations from ideal behaviour [66].

Calculation of T_o curves requires the knowledge of thermodynamic properties of the phases in competition at concentrations and temperatures where some of them are not stable. Assuming rapid interface kinetics, solute trapping, a constant partition coefficient and a dilute solution, Boettinger and Coriell [67] showed that T_o line can be approximated by:

$$T_o = T_f + \frac{X\, m\, ln\, (k_o)}{k_o - 1} \qquad (2)$$

where T_f is the melting point, m, the liquidus slope, k_o, the equilibrium partition coefficient and X the mole fraction of solute at the solid-liquid interface. This approximation helps determine the characteristics of the T_o line and will be used in this study to explain some of the possible solubility extensions.

2.2.3.2 Kinetics of rapid solidification

In addition to chemical and thermodynamic considerations, the kinetic conditions necessary to obtain solute trapping by rapid solidification should be considered. At high solidification rates, dendrites or cells no longer form and a homogeneous solid is produced. By rapid solidification, complete supersaturation of the crystal can be obtained either by planar front growth of the solid-liquid interface at the limit of absolute stability [68] or by partitionless solidification due to loss of local equilibrium [69], section 2.2.3.1.

The conditions required for planar growth at the limit of absolute stability were proposed by Coriell and Sekerka [68] who applied the perturbation theory of morphological stability of the interface of Mullins and Sekerka [70] to rapid solidification rates. For growth at high velocities, surface tension restabilizes the solidification front when the heat flow is towards the solid, as is most often

encountered in melt spinning. The threshold velocity V_a that must be exceeded to result in absolute stability is given by:

$$V_a = \frac{\Delta T_0 D}{k\Gamma} \qquad (3)$$

where ΔT_0 (not to be confused with T_o defined in the previous section) is the alloy freezing range, given by:

$$\Delta T_0 = \frac{mC_o(k\text{-}1)}{k} \qquad (4)$$

and D is the solute diffusivity in the liquid, k is the solute interface partition coefficient and Γ is the Gibbs-Thomson coefficient $\gamma/\Delta S$, m is the liquidus slope, defined so that the product (k-1)m is always positive. C_o is the alloy concentration, γ the solid-liquid interfacial energy, and ΔS the entropy of fusion.

It was shown by Aziz [71] that the solute distribution coefficient deviates from its equilibrium value as the velocity of the interface increases:

$$k_v = \frac{k_o + a_o V/D}{1 + a_o V/D} \qquad (5)$$

where k_v is the kinetic partition coefficient, k_o the equilibrium partition coefficient, a_oV/D is related to the interfacial peclet number where a_o is the atomic jump distance at the solid-liquid interface, and V the interface velocity. It is important to note that under conditions of absolute stability solute trapping occurs, the composition of the solid being determined by k_v which is not necessarily unity.

The transition to partitionless solidification occurs when the velocity of the interface surpasses the diffusive speed of the solute in the liquid (the interface peclet number reaches unity). At this point there is a rise in the partition coefficient from the value given by Aziz ($k_v = (k_o+1)/2$) towards unity [72]. The velocity of the interface under these conditions is determined by V_i thus:

$$V_i = \frac{D}{a_o} \qquad (6)$$

Equations 3 and 4 show that V_a increases with solute concentration. In such cases solidification without segregation will occur by partitionless solidification rather than absolute stability beyond a critical concentration $C_o^{crit.}$ at which V_a has reached

V_t [73]. If the condition is set that $V_a = V_t$ the following equation for $C_o^{crit.}$ is obtained:

$$C_o^{crit.} = \frac{k^2 \Gamma}{m\,(k\text{-}1)\,a_o} \qquad (7)$$

$C_o^{crit.}$ is therefore the theoretical composition below which supersaturation is obtained by absolute stability and above which loss of local equilibrium will control the supersaturation. In the latter case the condition $k_v = 1$ can only be obtained when the interface temperature falls below T_o as shown in the previous section.

For values of the equilibrium partition coefficient close to unity and with a small ΔT_0, V_a will increase slowly with concentration and will never reach V_t. For such systems, solubility extension is relatively easy, and the segregation free solid is obtained by growth at the limit of absolute stability. For partition coefficients very much less than unity, V_a will rise steeply with C_o and will reach $C_o^{crit.}$ at low concentrations. Solubility extension is thereafter controlled by partitionless solidification which necessitates a faster growth velocity, V_t. The value of $C_o^{crit.}$ can therefore be regarded as a means of assessment of the ease of solubility extension.

$C_o^{crit.}$ should in real terms be calculated using the kinetic partition coefficient, which itself is a function of the interface velocity, and a solute diffusivity, which is a function of the interface temperature. If these kinetic terms ($k_v(V)$ and $D(T)$) are introduced into the equation of V_a, absolute stability occurs at speeds smaller than those predicted by the equilibrium parameters, which would push $C_o^{crit.}$ to higher concentrations [74]. Analysis of solubility extension in the light of the $C_o^{crit.}$ criterion will be described later for the solutes employed in this study.

2.2.4 Dispersoid stability

The combination of solutes to produce a stable dispersion in the solid state by microsegregation requires that the solutes and dispersion be soluble in the liquid before rapid solidification. Oxides and nitrides are difficult dispersions to introduce due to the poor solubility of oxygen and nitrogen in liquid copper. Dispersions composed of phosphides, silicides, and arsenides are not suitable because of the strong effect of phosphorus, silicon and arsenic on the conductivity of copper. Boron has a good solubility in liquid copper, a minor influence on conductivity and a wide range metal-boron compounds with different stabilities. Ternary copper-metal-boron systems could therefore be interesting microsegregation dispersion hardened alloys to explore. Table II.4 summarizes the melting points [21] and heats of formation [62, 75] of various metal borides. It can be seen that melting point and heat of formation of the borides are related and when the heat of formation is not known, the melting point may be used to assess stability.

For the purpose of this study different borides were envisaged. In the lower range of stabilities, assuming that the stability of Ni_3B is sufficiently high to limit the solubility of nickel in the copper-Ni_3B system, this pseudo-binary system was interesting to study. Intermediate stability and stable borides such as those of chromium, cobalt, iron, nickel, titanium, yttrium and zirconium, were also studied as possible microsegregated dispersions.

Table II.4 Melting points and heats of formation of various metal borides.

Boride	Melting point (°C)	Standard heat of formation ΔH_f[298] ($kJmol^{-1}$)
Ni_3B	1156	
FeB	1650	71
Fe_2B	1389	71
CrB_2	1900	94
YB_6	2300	100
AlB_{12}	2000	201
VB_2	2400	205
NbB_2	3000	251
TiB_2	2980	281
ZrB_2	3040	324
CeB_6	2550	352

2.3 Mechanical properties

It is of interest to explore the mechanisms which determine the flow strength of rapidly solidified dispersion hardened alloys. In the presence of a uniform distribution of particles the shear stress increase due to the bowing of dislocations between particles can be calculated using the equation proposed by Kocks for Orowan looping [76]:

$$\tau_{edge} = \frac{1}{1.18}\frac{2A}{\lambda_p} \qquad (8)$$

where

$$A = \frac{\mu b^2}{4\pi} ln\left(\frac{\phi}{2b}\right) \qquad (9)$$

and λ_p is the centre to centre planar interparticle spacing, b the Burgers vector, μ the shear modulus of copper and ϕ is the obstacle size. It must be noted that this

relationship describes the strengthening achieved by randomly distributed non-shearable particles.

It was shown in several works [19, 41, 47-49] that the flow strength of mechanically alloyed or rapidly solidified and aged, dispersion hardened, copper alloys could be explained by an equation similar to that proposed by Kocks. Introducing the appropriate values in equation 8, considering a Taylor factor of 3 and an equivalent number of edge and screw dislocations taking part in particle bypassing, the contribution to strength brought about by the presence of a uniform distribution of non-shearable particles in copper can be written as [47]:

$$\Delta\sigma = \frac{6}{\lambda_p \cdot \phi} ln\left(\frac{\phi}{2b}\right) \qquad (10)$$

In a composite approach to strengthening, Kocks [77] suggested that the experimental flow stress, σ_{exp}, could be expressed as the sum of volume fraction-weighted contributions of each of the strengthening mechanisms. Morris and Morris [41] showed that for rapidly solidified copper-manganese-boron alloys the flow strengths (taken at 0.2% deformation) can be explained by:

$$\sigma_{exp} = f_{v_{gb}}\sigma_{gb} + \left(1-f_{v_{gb}}\right)\left[f_{v_c}\left\{\sqrt{\bar{\sigma}_{p_v}^2+\bar{\sigma}_{p_c}^2} + \sigma_m\right\} + \left(1-f_{v_c}\right)\left(\bar{\sigma}_{p_v}+\sigma_m\right)\right] \qquad (11)$$

where $f_{v_{gb}}$ is the volume fraction of grain boundaries, σ_{gb}, the local flow stress at the grain boundary, f_{v_c} is the volume fraction of cell walls in the interior of the grains. The term in curly brackets represents the contribution to the flow stress at the walls of the solidification cell given by the bimodal distribution of particles which is composed of: (a) the particles present only at the cell boundary contributing to strength by $\bar{\sigma}_{p_c}$, and (b) those uniformly distributed throughout the volume giving a strength contribution of $\bar{\sigma}_{p_v}$, and; (c) the strength, σ_m, the flow stress of the soft matrix.

Strengthening by grain refinement has been studied on many occasions in rapidly solidified materials. The exponent n, of grain size dependence can assume values anywhere between -1/3 and -1 in the equation:

$$\sigma = \sigma_o + Kd^n \qquad (12)$$

where σ is the flow stress and K and σ_o material parameters. Morris and Morris [41] showed that the matrix stress was inversely proportional to the grain size. This was achieved by subtracting the contribution of stress due to particles given by equation 10 from the experimental flow stress, in rapidly solidified copper-manganese-boron ribbons of 0.5-5 μm grain size. They determined that the matrix stress followed the relation:

$$\sigma_m = 60\ [MPa\mu m]\ \frac{1}{d} \qquad (13)$$

where d is given in microns. Chokshi *et al.* [78] using microhardness measurements determined a Hall-Petch relationship for OHFC copper for grain sizes ranging from 5-25 μm to be:

$$H_v = 52 + 60\ [\mu m^{\frac{1}{2}}]\ \frac{1}{\sqrt{d}} \qquad (14)$$

where H_v is the Vickers hardness (in H_v) and d the average grain size (in μm).

In order to achieve a yield strength of 500 MPa, the value chosen as desirable in this study, the established theories can be used to determine the particle size necessary for a given volume fraction. As a crude approximation, grain size strengthening will be neglected for the moment. Particle strengthening requires a particle size of approximately 8 nm and 20 nm if a volume fraction of dispersion of 2 and 5% is considered.

2.4 Particle coarsening

A knowledge of the kinetics of microstructural change is important for ensuring maintenance of fine microstructure both during consolidation as well as during usage of the material. The coarsening rate will depend on three major terms: the particle-matrix interfacial energy and the solubility and diffusivity of the rate controlling element. The rate of change in microstructure can be predicted using established models based on different rate controlling solute transport mechanisms for comparison with experimental observations.

The driving force for particle coarsening is the reduction of the total particle-matrix interfacial energy in the system. The growth originates from the concentration gradients around the particles caused by the thermodynamic equilibrium between the curvature of the interface and the chemical potential at the interface, represented by the Gibbs-Thomson equation. The solute concentration at the surface of large particles is lower than that at smaller particles. Solute flows through the concentration gradients from the surface of the smaller particles to the surface of larger particles. During this process, the average radius of the particles increases. For bulk transport controlled coarsening size is related by $r^3 \propto t$. If the transfer is controlled by pipe diffusion, established models predict that growth will follow either a $r^4 \propto t$ or $r^5 \propto t$ relation depending on the arrangement of the dislocations and their density in the material. If transfer is grain boundary controlled, growth follows a $r^4 \propto t$ dependance. If the rate determining step in coarsening is transport across the interface growth will follow a $r^2 \propto t$ relationship [79, 80].

The problem of growth of particles by diffusion of solute in a matrix was first treated by Greenwood in 1956 [81]. The basic equations on which the analysis is based come from the Gibbs-Thomson relation for the concentration of solute in equilibrium with a particle of radius, r. For a regular solution the solute solubility X_∞ (in atom fraction), of a particle of infinite size can be approximated by:

$$X_\infty = exp\left(\frac{-(\Delta G + \Omega)}{kT}\right) \qquad (15)$$

where ΔG is the ideal free energy of mixing and Ω is the regular solution interaction coefficient. For spherical particles with a finite radius r, the solubility X_r becomes:

$$X_r = exp\left(\frac{-\left(\Delta G + \Omega - \frac{2\gamma V_m}{r}\right)}{RT}\right) \qquad (16)$$

where γ is the interfacial energy and V_m the particle molar volume. From equations 15 and 16, the solubility at a particle of radius r can be approximated by:

$$X_r = X_\infty\left(1 + \frac{2\gamma V_m}{RTr}\right) \qquad (17)$$

Ficks' law for the diffusion flux, j, can be written:

$$j = -D\left(\frac{\partial C}{\partial \xi}\right) \qquad (18)$$

where D is the diffusivity C the solute concentration (in mol m^{-3}) and ξ the distance ahead of the particle. The combination of equations 17 and 18 establish the rate of growth of the particle.

The theory of particle coarsening was further developed by Lifshitz and Slyozov [82] and independently by Wagner [83] to model the kinetics of particle growth. The Lifshitz, Slyozov and Wagner (LSW) theory is based on a zero volume fraction approximation which does not correspond to real situations. Because of this, considerable work was undertaken to modify the basic equations to avoid the approximation. The theory of particle coarsening depends on the solution of three basic equations, these are: (a) the kinetic relation, derived from the flux and the Gibbs-Thomson equations which gives the growth rate of an individual particle (b) the continuity equation which establishes competitive growth between particles

having a size different from the critical radius# and must obey the particle size distribution and; (c) the conservation equation which presupposes that the quantity of matter in the system remains constant and for which the solution of (a) and (b) must be satisfied.

Many factors have been found to influence the coarsening kinetics of particles in different degrees depending on the system under study. The major factors dealt with in this study are: (a) volume fraction and; (b) short circuit diffusion paths such as surfaces, grain boundaries and dislocations.

2.4.1 Volume fraction effect

As mentioned earlier, the LSW theory is applicable only when the volume fraction of particle is essentially zero and the rate determining mechanism is transport through the bulk. It predicts that the average volume of spherical particles increases linearly and that the particle size distribution reaches asymptotically a stable theoretical distribution with time. Experimental measurements in systems where the volume fraction is non-zero show similar behaviours, but the size distributions observed are broader than that predicted by the theory.

The difficulty of including the effect of volume fraction in the theory of particle coarsening lies in the choice of the cut-off point or the size of the sphere of influence when considering the flux equation. The solution for steady state diffusion through concentric spheres of radii r and r' is given by [84]:

$$\left[\frac{dX}{d\xi}\right]_{\xi=r} = \frac{X' - X_r}{r\left(1 - r/r'\right)} \qquad (19)$$

where X' is the concentration at ξ=r'. This equation was simplified in the LSW treatment by taking the cut-off distance as infinity (*i.e.* the interparticle spacing is infinitely larger than the size of the particle), therefore letting $r'=\infty$ equation 19 becomes:

$$\left[\frac{dX}{d\xi}\right]_{\xi=r} = \frac{X_\infty' - X_r}{r} \qquad (20)$$

As long as the concentration gradient is given by equation 20 neither modeling of the effect of volume fraction nor the diffusion geometry around the particle can be taken into account, since the parameter r' is no longer present [85].

#The critical particle radius, r_c, is the radius of the particle in a given particle distribution where $dr_c/dt = 0$

Ardell [86] considered the radius of the sphere of influence to be one-half the centre to centre interparticle spacing. The result showed that the coarsening rate increased with volume fraction and the theoretical size distribution broadened rapidly with the increasing volume fraction of the second phase. Growth nevertheless followed the $r^3 \propto t$ relationship. Tsumuraya and Miyata [85] gave six other alternative diffusion geometries for r', their models predicted that the particle size distribution changes in skewness as the volume fraction increased. Several other contributions [87-95] dealt with the volume fraction by either modifying the diffusion geometry, using computer simulation techniques or a statistical approach. These models all showed that: (a) $r^3 \propto t$ is followed for bulk diffusion controlled coarsening, (b) the rate constant increased with volume fraction (the precise value varies considerably with the model) and; (c) the particle size distribution broadened with the rise in volume fraction of second phase. For these theories, the variation of the ratio of the theoretically predicted, to the LSW rate constant, is approximately 1.5 for all but Ardells' model which predicts a ratio of 3 for 5vol% of dispersion.

In reality, the absolute values of the predicted rate constants cannot easily be compared with experimental values because of the lack of precise information on the interfacial energy, γ, and diffusivity, D. In fact, many investigations [96-99] have not clearly demonstrated a volume fraction dependence. Ardell [100] recently showed, for a significant range of volume fractions and within the limits of experimental error, the rate constant for diffusion controlled coarsening of γ' precipitates in nickel alloys is independent of volume fraction.

2.4.2 Short circuit diffusion paths

For particles lying on grain boundaries or connected by dislocations, solute diffusion paths can be the grain boundaries or dislocations, although solute can still flow to the particle directly from the volume. Theories developed incorporating the above factors are along the lines of the LSW development. They all result in equations of the type:

$$r^n - r_o^n = \kappa_n t \qquad (21)$$

where κ_n is the rate constant and n the rate exponent. Depending on the precise diffusion geometry and the assumptions made κ_n has different values.

For bulk diffusion controlled coarsening, under the LSW assumptions, the following equation applies:

$$\kappa_3 = \frac{8}{9} D_{bulk} \frac{\gamma X_\infty V_m}{RT} \qquad (22)$$

where D_{bulk} is the bulk diffusion coefficient. If the possible effect of a finite volume fraction is to be considered, the rate constant can be written as $\alpha(f_v)\kappa_3$.

For grain boundary controlled growth, the rate constant initially proposed by Speight [101] was:

$$\kappa_4 = \frac{4}{3} D_{gb} \frac{\gamma X_\infty V_m \delta}{ABRT} \qquad (23)$$

where the rate exponent n is equal to 4, D_{gb} the grain boundary diffusivity, δ the grain boundary thickness and A and B material constants for a given system, depending on interfacial energy and volume fraction of second phase particles on the boundary, thus:

$$A = \frac{2}{3} \cdot \frac{\gamma_{gb}}{2\gamma} + \frac{1}{3}\left(\frac{\gamma_{gb}}{2\gamma}\right)^3 \qquad (24)$$

where γ_{gb} is the grain boundary surface energy, and; $B \approx 0.5\ ln(m/f)$ where f is the area fraction occupied by m particles on the boundary. Modifications of κ_4 for grain boundary diffusion controlled growth with respect to the diffusion geometry were proposed by other authors [102, 103]. However these result in only slight modifications of the numerical values of equation 23.

Similarly several relations have been proposed for the rate constant of pipe diffusion controlled coarsening. Kreye [104] established, for a three dimensional network of dislocations, that the size of the particle raised to the fifth power was proportional to the annealing time and that the rate constant could be written as:

$$\kappa_5 = \left(\frac{4}{5}\right)^5 \frac{5}{4\pi} N q D_{pipe} \frac{\gamma X_\infty V_m}{RT} \qquad (25)$$

where N is the average number of dislocations reaching a particle, q the cross section of a dislocation pipe and D_{pipe} the pipe diffusivity of the solute. Ardell [103] proposed a similar relation for a two dimensional network of dislocations as long as the dislocation spacing was larger than the particle size. When the dislocation spacing came close to the particle size, a fourth power law was observed.

It is clear that in real situations particles within the matrix have a certain number of connecting dislocations. The relative importance of these dislocations on the coarsening of the particles will obviously depend on their number and on the annealing temperature. No systematic method based on microstructural observations, has been established that identifies which of the transport paths will

dominate during coarsening. An attempt to establish a method to determine the rate controlling transport path will be carried out in this study.

CHAPTER 3

Experimental Conditions and Methods of Analysis

3. Experimental Conditions and Methods of Analysis

Different elements were chosen as alloying additions to copper in accordance with conditions outlined in section 2.2 based on conductivity, solubility, diffusivity and ease of handling. Assessment of the alloys was carried out in two stages. Initially, alloys were cast and their homogeneity was examined optically. Metallographically homogeneous ingots were melt spun. The ribbons were chemically analyzed. They were then annealed for 30 min at different temperatures and mechanically tested. The evolution of mechanical properties and optical microstructure with temperature for a given ribbon was used to characterize the thermal stability of the microstructure. Ribbons showing fairly high strengths after elevated temperature treatments, or good thermal stability, were selected for further study. In the second stage, quantification of the microstructural evolution on annealing was carried out. Analysis of the rate of change clarified the mechanisms which controlled the observed stability, thus making it possible to suggest improved alloys. The following sections will describe the experimental methods used in preparing the rapidly solidified materials and for analyses of microstructure and mechanical properties.

3.1 Preparation of Ingots

Experimental alloy ingots weighing two hundred grams were prepared by induction melting elements in the form of pieces 2-10mm in size in quartz tubes.* Reactive elements such as calcium, cerium, yttrium and zirconium, were introduced by means of copper-rich master alloys close to the eutectic composition which were initially cast and chemically analyzed. Solute loss or contamination was thereby limited. Melting was done under a protective atmosphere of helium. Before fusion, the mixtures were initially degassed to remove any adsorbed contaminants. Table III.1 lists the binary and ternary alloys cast in this study.

Table III.1 Chemical compositions (in atomic percent) of the experimental alloys cast

Binary compositions			
Cu-Ca 0.5			
Cu-Ce 1.23			
Cu-B 2.7	Cu-B 7.34		
Cu-Y 0.7	Cu-Y 1.5		
Cu-Cr 1.85	Cu-Cr 2.54	Cu-Cr 5.00	
Cu-Zr 0.33	Cu-Zr 0.55	Cu-Zr 0.79	Cu-Zr 1.70

*The purity of the starting elements used was generally above 99.95%. Supplier for Cu, Zr, Cr, Ti, Fe, Co and Si elemental pieces was Balzers A.G., while Ce, Ca, Y, and B came from CERAC Inc.

Ternary compositions

Cu-Co1 B2
Cu-Cr1 B2
Cu-Fe1 B2
Cu-Ti1 B2
Cu-Zr1 B2

Cu-Y0.18 B2.45	Cu-Y0.23 B5.66	Cu-Y0.6 B0.6	Cu-Y2.6 B5.22
Cu-Ni1.98 B0.70	Cu-Ni4.60 B1.25	Cu-Ni7.10 B1.75	Cu-Ni12.6 B4.05
Cu-Ni1.01 B3.05	Cu-Ni3.95 B1.33		
Cu-Cr0.57 Zr0.50	Cu-Cr1.11 Zr0.40	Cu-Cr1.74 Zr0.56	Cu-Cr1.83 Zr0.09
Cu-Cr1.96 Zr0.54	Cu-Cr2.19 Zr0.18	Cu-Cr2.08 Zr0.65	Cu-Cr2.11 Zr0.81
Cu-Cr2.40 Zr0.18	Cu-Cr2.47 Zr0.06	Cu-Cr2.51 Zr0.38	Cu-Cr2.49 Zr0.47
Cu-Cr2.46 Zr0.92	Cu-Cr2.51 Zr0.98	Cu-Cr2.73 Zr0.20	Cu-Cr3.06 Zr1.53
Cu-Cr3.18 Zr0.06	Cu-Cr3.28 Zr0.15	Cu-Cr3.12 Zr0.39	Cu-Cr4.13 Zr0.34
Cu-Cr2.44 Mg0.3	Cu-Cr2.22 Ti0.11	Cu-Cr2.41 Si0.23	

3.2 Melt spinning

In the melt spinning process, as in other rapid solidification techniques, the scale over which heat extraction takes place must be reduced to obtain quench rates ranging from 10^4-10^6 Ks^{-1} [105]. Melt spinning is based on a simple technique whereby liquid metal is expelled by an over pressure of inert gas through an orifice in the bottom of a crucible. The metal stream formed impinges on a rotating cold substrate and produces a ribbon, typically 30-150 µm thick. Heat extraction primarily takes place during the time the metal stream is in contact with the cold substrate. This primary cooling is the most important and is dependent on the metal flux, the wheel speed and the heat transfer coefficients between the cold substrate and the liquid metal [106]. Ribbon thickness has been shown to be related to quench rate [107-110]. Depending on process parameters such as wheel speed, ejection pressure, orifice size and liquid metal viscosity, the thickness of the ribbon produced can be controlled [111, 112] which enables the choice and control of quench rate. Melt spinning therefore offers the possibility of producing ribbons with different quench rates for experimental analyses.

Various studies have related other experimental conditions to ribbon quality, such as the gas pressure and composition of the substrate material, its temperature and roughness [106, 113, 114]. It was clearly shown from these studies that the quality of the ribbon produced is very sensitive to melt spinning parameters.

Melt spinning was carried out on a modified *1M Melt spinner* of Marko Materials inc. This apparatus consisted of a stainless steel chamber connected to a vacuum system permitting evacuation and back filling with helium gas. Twenty grams of the experimental alloy were introduced into a quartz tube having a conical end with an orifice diameter of 0.9 mm. After several purges of the chamber with helium gas, the alloy was induction melted under a chamber partial pressure of 0.5 atm. The conical end of the quartz tube was placed 4-8 mm above a rotating copper-beryllium wheel, 25 cm in diameter, for which the rotation speed could be

controlled from 6-43 ms^{-1}. At a temperature of about 1500°C* an over-pressure was applied to the quartz tube, ejecting the molten alloy onto the rotating wheel, diamond polished to 1μm. For most of the ribbons spun, the over-pressure was 0.9 atm. Experiments at different quench rates were carried out by changing the rotation speed of the copper wheel, keeping all other parameters constant. Under these general conditions, with a peripheral wheel speed of 36 ms^{-1}, ribbons 3 mm wide and 30 μm thick were produced (these dimensions varied, depending on the viscosity of the alloy at ejection). Figure III.1 shows a schematic diagram of the melt spinning apparatus used.

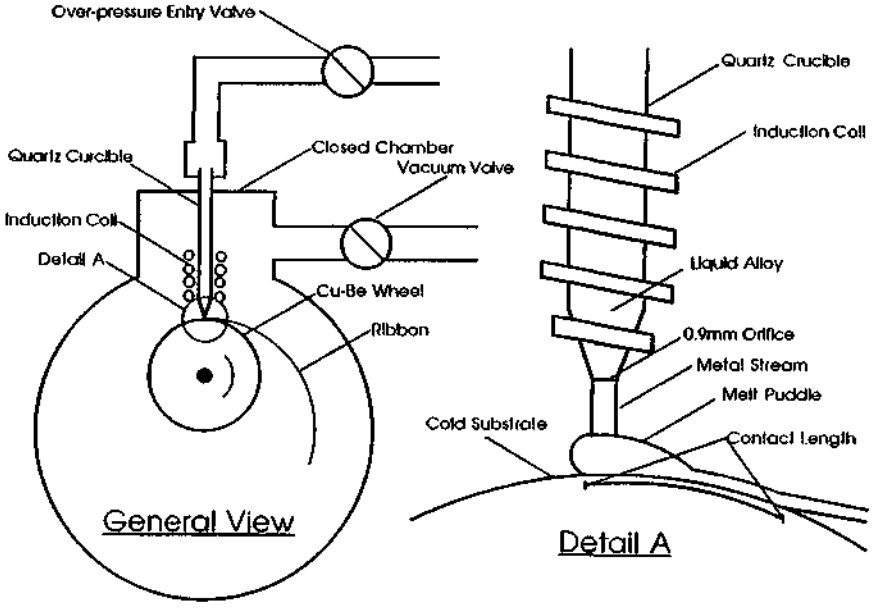

Figure III.1 Schematic diagram of the melt spinning apparatus used. In detail is the crucible-melt puddle region showing ribbon formation

A number of difficulties were encountered when melt spinning boron free copper alloys containing less than the equivalent of 4vol% of second phase. These alloys were viscous at the melt ejection temperature. Melt spinning these alloys at

*Estimated from initial calibration of induction furnace settings against thermocouple readings during the fusion of a similar quantity of copper.

speeds above 26 ms^{-1} resulted in fragmented ribbons with variations in width. This limited the maximum casting speeds of these dilute boron-free alloys to 26 ms^{-1}. Boron-containing alloys were however sufficiently fluid and generally easier to melt spin. For these compositions no limitations on the casting speed were encountered.

3.3 Optical microstructural examinations of ribbons

Optical metallography was carried out on transverse sections of as cast and heat treated ribbons. Ribbons were mounted transversally in hard bakalite, diamond polished and chemically etched using a solution of 100 ml H_2O, 8 ml H_2SO_4, 1.5 g NaCl and 2 g $K_2Cr_2O_7$. The uniformity of the microstructure along the ribbons length was examined. If microstructural heterogeneity was observed, the ribbon was discarded and another sample cast. Microstructurally uniform samples were chemically analyzed by Optical Emission Spectroscopy. This enabled contamination or solute loss to be detected as well as to know the precise composition of the ribbon.

3.4 Heat treatments

Due to the reactive nature of the alloying elements used, all heat treatments were carried out under inert atmospheres. Short anneals, ranging from 10 min to 24 h, were carried out in a muffle furnace under a flow of argon. For heat treatments of several days, the melt spun ribbons were encapsulated in quartz ampoules under argon containing a small quantity of titanium powder as getter which was isolated from the samples by refractory wool.

3.5 Mechanical property assessment

Tensile tests were performed on a Schenck universal tensile testing machine. Without any preliminary preparation, pieces of melt spun ribbon 30-40 mm long were gripped using special flat hydraulic grips. The grip plates were coated with a non-adherent ceramic coating and had rounded edges to prevent any local stress concentrations on the ribbon at the points of attachment. Each sample was placed vertically between the grips so that 5-10 mm of ribbon were held in each grip. The gauge length, determined by the separation between the grips was fixed at 20 mm for all the tests. Several tests were carried out for each heat treated state of the ribbon. The cross head speed was fixed at 1 mm min^{-1}. The load, monitored by a 2 kN load cell, was converted to stress using the average cross sectional area, A, of the sample tested, such that:

$$A = {}^{W}/_{L\,\rho} \qquad (1)$$

where W is the weight, L the length and, ρ, the density taken as that of pure copper (since the volume fraction of second phase usually did not exceed 5^{vol}%, this only

slightly modified the density of the alloy with respect to pure copper). Figure III.2 shows typical force-deformation curves obtained by tensile testing melt spun ribbons after 30 min anneals.

Tensile testing of ribbons provided data on the mechanical properties of the over-all microstructure of the rapidly solidified ribbon. However, some ribbons showed large microstructural variations throughout their thickness. For more precise evaluation of the properties of these different microstructures, microhardness tests were carried out. On ribbons showing distinct wheel and free surface microstructures, Vickers microhardness tests were carried out on each surface. The ribbons were mounted flat on glass slides and polished with 3 μm diamond paste. Indentation loads of 15-25 g were used for most of the microhardness testing.

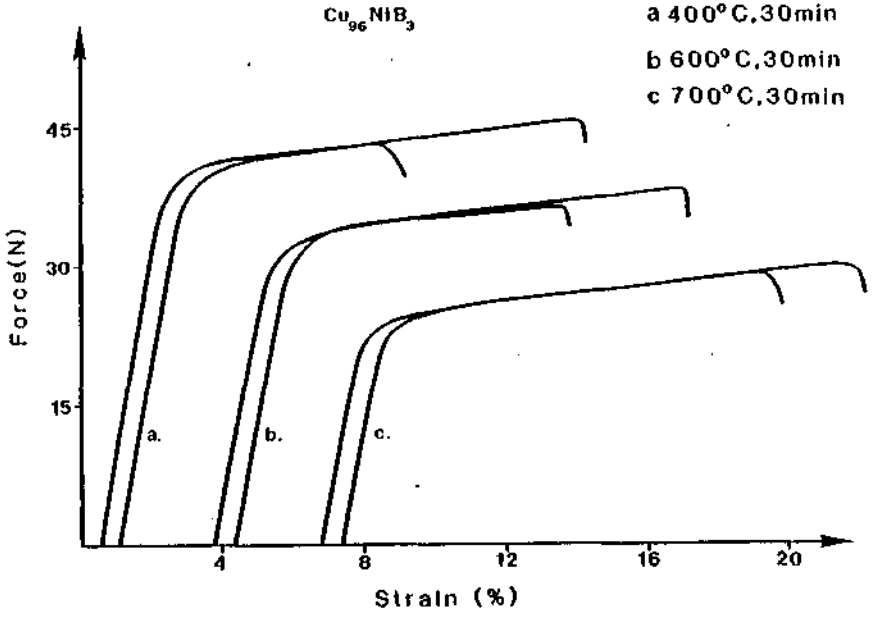

Figure III.2 Typical tensile curves obtained by the direct testing of rapidly solidified Cu Ni1.01at% B3.05at% ribbons spun at 36 ms^{-1} and annealed at 400, 600 and 700°C for 30 min. It can be seen that the flow stress of the ribbons is reproducible, while variations in ductility occur.

3.6 Electron microscopy

Microstructural observations were carried out principally by transmission electron microscopy. For the as cast and heat treated ribbons quantification of the microstructural evolution and crystallographic identification of phases by diffraction analyses was performed using initially a *Philips 300* and subsequently a *Philips CM12* transmission electron microscope. Scanning electron microscopy was carried out on a *Cambridge 250 Stereoscan* scanning electron microscope.

3.6.1 Thin foil preparation

Electron transparent foils for transmission electron microscopy were prepared by twin jet electropolishing using a *Tenupol* system. Two different electrolytes were used depending on the alloy composition. For most boron containing samples, the electrolyte was based on a solution of 50$^{vol\%}$ H_3PO_4 in water. Optimal conditions ranged from 5 to 15°C and from 5 to 25V. For boron free ribbons, electropolishing was carried out using a 30$^{vol\%}$ HNO_3 in methanol solution. Depending on the sample and its heat treatment, thinning conditions varied greatly, ranging from -60 to -15°C and from 3 to 35V. For samples where the dislocation density was to be estimated, care was taken to limit the introduction of any extra dislocations during thin foil preparation. In some cases, such as for the annealed Cu Y0.7$^{at\%}$ ribbons, where large micron-sized yttrium-rich particles formed, no electrolyte, nor temperature / potential condition was found that would simultaneously electropolish the copper and the yttrium-rich phase. Other thinning techniques such as ion bombardment were tried without improvement. For this alloy, electrolytic thinning with a nitric acid / methanol mixture was employed at -60°C, minimizing preferential attack of the yttrium-rich phase.

3.6.2 Phase identification

Crystallographic analyses by electron diffraction of dispersed particles in copper were carried out in some of the rapidly solidified alloys studied. This enabled phase identification, as well as the characterization of possible phase transformations which may result from heat treatment. Depending on the size and nature of the particle to be analyzed, the diffraction patterns were either obtained by direct analysis of the particle in the thin foil (analysis of a particle near the edge of the foil in order to minimize the copper matrix diffraction), or obtained by analysis of the particle extracted on a carbon replica.

Standard techniques were used to obtain replicas [115, 116]: after deep etching and vacuum evaporation of carbon on the ribbons surface, the copper matrix was dissolved in a 10$^{vol\%}$ bromine in methanol solution, leaving behind the

carbon replica which was thereafter rinsed in successive mixtures of methanol and water and mounted on copper or beryllium grids for examination.

The crystallographic analysis of an unknown phase was carried out by tilt experiments in the TEM using a double tilt sample holder. Characteristic zone axes were deduced by selected area diffraction, occasionally the diffraction pattern was obtained by microdiffraction. Knowing the approximate chemical composition of the particle to be analyzed, diffraction patterns obtained were first compared to possible structures. The analysis was based on the angles between the zone axes and the symmetry of the diffraction patterns. For this, the EMS software due to Stadelmann was used [117]. This permitted an identification of the structure. Confirmation of the structure was possible using computer generated diffraction patterns. The different zone axes were obtained either by tilting following Kikuchi lines in diffraction mode, or by tilting in dark field keeping a specific reflection excited and systematically switching to diffraction in order to determine whether the particle was oriented close to a characteristic zone axis.

3.7 Quantitative metallography

Quantification of the microstructures of the rapidly solidified alloys was carried out by optical and electron microscopy. Since optical microscopy presents a two dimensional section through the three dimensional structure, the data on size and size distribution was treated differently from the data obtained by transmission electron microscopy where the image observed was a direct projection of the three dimensional structure of the material (as long as the scale of the features examined is not significantly different from the foil thickness). Quantitative analysis of size and surface fraction was carried out on a *Cambridge Quantimet 970* image analyzer. Analysis was accomplished either by direct optical examination of the structure, or by tracing the features of interest from TEM micrographs onto transparencies for analysis.

3.7.1 Quantitative optical metallography

Quantitative optical metallography was carried out only on boron rich ribbons. These rapidly solidified alloys were characterized by a microstructural instability which occurred upon heat treatment; metastable boron-rich particles present in the alloy dissolved at the expense of a more stable, rapidly growing, equilibrium phase. The precise description of the events leading to this transformation are described later. Quantification of the number density and the size distribution of the stable phase was necessary in order to determine the mechanisms which controlled the rate of transformation.

Figure III.3 shows an optical section of the typical phase formed upon heat treatment. The particle consisted of many branches radiating from a central point. Its size, Φ, was estimated as the diameter of the circle encompassing the particle,

assuming that the shape could be assimilated to a solid sphere. This assumption is only valid for small particle sizes and deviates from reality as the particle size increases and the structure of the particles becomes arborescent. From the number of particles per unit area, N_S, the true particle volume density, N_V, was determined [118] by the equation:

$$N_V = \frac{N_S}{\Phi_{max}} \qquad (2)$$

The maximum size, Φ_{max}, was used, instead of the average size, $\overline{\Phi}$, since it was assumed that all the boron crystals appeared at approximately the same instant, the size distribution being close to monodispersed, *cf.* section 4.1.2, page 51. The volume fraction, f_V, of crystalline boron was determined as the measured area fraction.

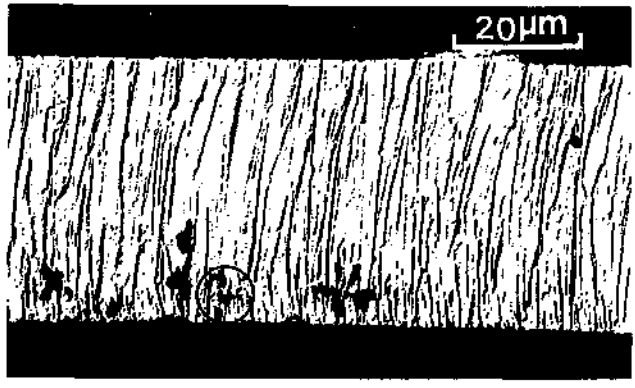

Figure III.3 Optical micrograph of a transverse section of a Cu Y0.23 at% B5.66 at% ribbon after heat treatment (850°C for 1h) showing the shape of the boron crystals and the radius of the encompassing circle used to define the size of the particle.

3.7.2 Quantitative transmission electron metallography

Quantitative measurements from transmission electron micrographs were limited to the determination of size and volume fraction of second phase particles. In some cases, the dislocation density in ribbons before and after heat treatment was estimated. Depending on the size and the nature of the particles, different contrasts were used to evaluate their dimensions. For small coherent (2-4 nm) particles, bright field images taken under two beam conditions were unsatisfactory because of the strong contrast associated with the coherency of the particles. Dark field images using precipitate reflections, or images taken under conditions of phase

contrast were used. For larger incoherent or semi-coherent particles, standard bright field images using two beam conditions were taken. Foil thickness necessary for volume fraction and dislocation density determinations, was estimated using analysis of fringe contrast on the grain or twin boundaries [119].

3.7.2.1 Definition of particle size

The definition of size depended on the application where the size of the particle intervened. For coarsening analysis, the size of the particle was defined differently from the size used in the analysis of Orowan strengthening. The coarsening size of a particle of arbitrary shape and volume, V, was defined by Lifshitz and Slyozov [82] as:

$$r_{eff} = \sqrt[3]{\frac{3V}{4\pi}} \qquad (3)$$

where the size of the particle is the radius of the sphere of equivalent volume. This formulation was not used here. Since coarsening mechanisms are controlled by the curvature of the particle, which depends on the specific shape, Wagner [83] defined a more appropriate effective radius as:

$$r_{eff} = 2\left(\frac{dV}{dA}\right) \qquad (4)$$

where A is the particle surface area. This definition takes better into account the actual shape of the particle.

Particle morphologies encountered in this work ranged from near-spherical to cigar shaped. For nearly spherical particles, the size was defined as the average radius obtained by taking the mean of the smallest and largest diameters. For the cigar shaped particles, Wagners' equation of r_{eff} was used (the development is given Annex 1) where:

$$r_{eff} = \frac{\varpi(3\tau - 2\varpi)}{2\tau} = \frac{\varpi(3\upsilon - 1)}{2\upsilon} \qquad (5)$$

and ϖ is the half width of the particle or the radius of the hemispherical cap, τ, the length, and, υ, the aspect ratio defined as $\tau/2\varpi$. It can be seen that in the above equation, for aspect ratios close to unity, the equation of r_{eff} approaches the radius of the sphere. For other values of aspect ratio, r_{eff} remains close to ϖ which characterizes the curvature of the particle, the important parameter determining the driving force for coarsening.

To define the obstacle size, ϕ, in the Orowan strengthening analysis, over which the dislocation is required to bow, the size of the cigar shaped particles was taken as a weighted average of the length and width of the particle:

$$\phi = \frac{4\varpi + \tau}{3} = \frac{2}{3}\varpi(\upsilon + 2) \qquad (6)$$

3.7.2.2 Inter-particle spacing

The volume number density, N_v, [118] was defined as:

$$N_V = \frac{f_v}{V} \qquad (7)$$

where f_v is the volume fraction deduced from the chemical composition of the alloy as well as the molar volume of the particle phase. The volume of the particle, V, was calculated as:

$$V = \frac{4}{3}\pi r^3 \qquad (8)$$

for nearly spherical particles or as:

$$V = 2\pi\varpi^3\left(\upsilon - 1/3\right) \qquad (9)$$

for the cigar shaped particles. The volume and planar interparticle spacings can thereby be determined respectively as:

$$\lambda_v = \frac{1}{\sqrt[3]{N_v}} \text{ and } \lambda_p = \frac{1}{\sqrt{N_v\phi}} = \sqrt{\frac{V}{f_v\phi}} \qquad (10, 11)$$

It can be seen that the particle spacing, planar or volume, can be related to the average size of the particle for a fixed volume fraction. Assuming nearly spherical particles for simplicity, the particle spacing can be written as $\lambda_i = \alpha_i r$ where r is the average radius of the particle and α_i is the proportionality constant being for volume and planar interparticle spacings respectively.

$$\alpha_v = \sqrt[3]{\frac{4\pi}{3f_v}} \text{ and } \alpha_p = \sqrt{\frac{2\pi}{3f_v}} \qquad (12, 13)$$

In some analyses it is not the centre to centre interparticle spacing which is important, but the free space between particles, defined as the surface to surface particle spacing $\lambda_i - 2r$. The relative error, δ, introduced by using λ_i instead of $\lambda_i - 2r$ can be expressed in terms of the volume fraction as:

$$\delta_i = \frac{\lambda_i}{\lambda_i - 2r} = \frac{\alpha_i r}{\alpha_i r - 2r} = \frac{\alpha_i}{\alpha_i - 2} \qquad (14)$$

Thus, the error can be shown to be about 20% for the planar interparticle spacing at a volume fraction of 2%.

CHAPTER 4
Results

4. Results

The following sections summarize the observations and measurements obtained from the alloys studied. They were classified into two families: the boron-free and the boron-containing compositions.

4.1 Optical assessment of Microstructures

Equiaxed or columnar grains with solid solution, cellular or dendritic solute distributions were observed after rapid solidification of the experimental alloys. The microstructures varied with concentration, casting conditions and type of alloying addition. The modes of solidification and the resultant microstructure were examined optically and the variation through the ribbon thickness noted.

4.1.1 Boron-free alloys

Optical examination of cast ingots of binary copper-calcium, cerium, chromium, yttrium and zirconium as well as ternary copper-chromium-metal alloys showed no microstructural heterogeneity after casting. Copper-niobium ingots were contaminated and difficult to cast. Figure IV.1 shows the microstructures obtained by melt spinning the Cu-Cr1.85 at% alloy under various conditions. The evolution of their optical microstructures upon heat treatment is also shown. In the as cast state at different wheel speeds (figure IV.1.a, b and c) all the ribbons consisted of columnar grains extending from the wheel contact side up to the free surface of the ribbon. This structure was typical of all the chromium-rich ribbons. The columnar grain width and ribbon thickness both decreased with increasing wheel speed. Ribbons cast at a slow speed of 6 ms^{-1} were thicker (≈150 µm) with a columnar width of approximately 5-10 µm, while ribbons cast at 36 ms^{-1} were approximately 30 µm thick, having a columnar grain width of 2-3 µm. Near the wheel surface the size was finer, but quickly reached a constant value through the rest of the ribbon thickness. For ribbons spun at 6 ms^{-1} a eutectic microstructure could be distinguished in some grains (figure IV.1.a). At wheel speeds of 16 ms^{-1} and above no second phase particles were optically visible for ribbons with chromium concentrations up to 2.5 at%, suggesting possible solid solution extension up to this concentration. In concentrations greater than 2.5 at% chromium, primary chromium particles were observed in the as cast state at all casting speeds. For ternary copper-chromium-metal ribbons, at metal concentrations less than 0.3 at% the microstructures were identical to the binary alloys when spun at similar speeds. However, ternary metal additions of zirconium above 0.3 at% presented different microstructures which were similar to the binary zirconium-rich ribbons. Because of the scale of the microstructures obtained, the precise extent of solid solution extension could not be assessed by optical microscopy. In this case electron

microscopy was necessary to survey the distribution of solute in the different ribbons.

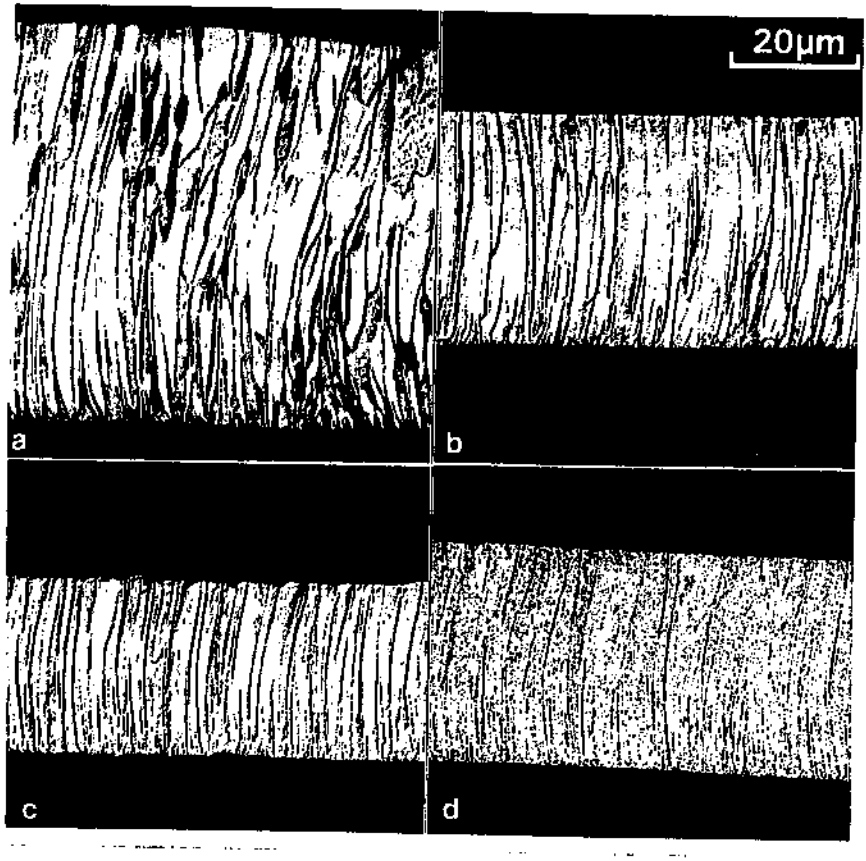

Figure IV.1 Transverse optical microstructure of Cu-Cr1.85 at% ribbons cast at different speeds and after heat treatment. (a) At 6 ms^{-1} the ribbon consisted of columnar grains containing optically visible chromium particles. At faster speeds from 16 (b) to 36 ms^{-1} (c) no particles are visible. Growth of chromium particles occurred on heat treatment (d) spun at 26 ms^{-1}, 800°C, 30 min.

Figure IV.2 shows the variation of microstructure with increasing amounts of solute and after heat treatment in copper-yttrium and copper-zirconium ribbons cast at 43 and 36 ms^{-1} respectively. Equivalent zones in the as cast state are found in the two yttrium-containing ribbons, having 0.7 at% (figure IV.2.a) and 1.7 at%

yttrium (figure IV.2.b). The structure was finer in the concentrated alloy. Near the wheel contact side, the ribbons showed a clear zone less susceptible to chemical etching due to the lack of coarse yttrium-rich second phase particles at grain or cell boundaries. This suggested that the excess yttrium was either in solid solution or that it was finely distributed within the grains as fine precipitation. Fine columnar grains extended from this zone. The level of metallographic etch was greater which suggested the presence of a segregated yttrium-rich phase. The top portion of the ribbons consisted of equiaxed microsegregated dendritic grains. Copper-calcium and copper-cerium ribbons cast at 43 ms^{-1} showed very similar microstructure and behaviour with solute content in the as cast state to the copper-yttrium ribbons; solute rich particles were observed at all casting speeds and concentrations throughout the ribbon thickness, with the exception of a narrow wheel contact zone.

Copper zirconium ribbons behaved midway between the copper-chromium and the copper-calcium, cerium and yttrium ribbons, when casting conditions or composition was changed. Figure IV.2.d and e show the transverse optical microstructure of the copper-zirconium 0.33 at% and 0.55 at% ribbons cast at 36 ms^{-1}. The dilute alloy consisted of columnar grains 1 μm in width. No zirconium-rich particles are optically visible suggesting solid solution extension to approximately 0.3 at%. Optical examination of the concentrated ribbon showed that it consisted of particle-free grains in the bottom half and of dendritic equiaxed grains on the top. Increasing the casting speed above 36 ms^{-1} did not show any lowering in the level of segregation for the concentrated zirconium-containing ribbons.

Growth, or precipitation followed by growth, of second phase particles occurred upon heat treatment in all the ribbons. For the copper-calcium, copper-cerium and copper-yttrium ribbons, the evolution of the microstructure upon heat treatment was faster than that of the copper-chromium or zirconium-containing ribbons. Figure IV.2.c shows the microstructure of Cu-Y0.7 at% ribbon after heat treatment of 30 min at 800°C. The coalescence of the yttrium-rich intermetallic into isolated grains resulted in rapid copper grain growth. The copper grains lost their columnar shape and reached a size of 5-10 μm. No distinction was possible between the different zones found in the as cast structure after 30 min heat treatments above 700°C. The copper-calcium and cerium ribbons showed similar rapid microstructural changes after heat treatment. Cu_5Ca or Cu_6Ce [21] intermetallic particles coalesced in a similar manner to the yttrium-rich phase, which resulted in a coarse duplex microstructure. Due to the similarity in behaviour of the calcium and cerium-containing to the copper-yttrium ribbons, the latter was taken to represent the two other alloys. Growth of the zirconium-rich particles in the copper-zirconium ribbons was slower. After heat treatment the zirconium-rich

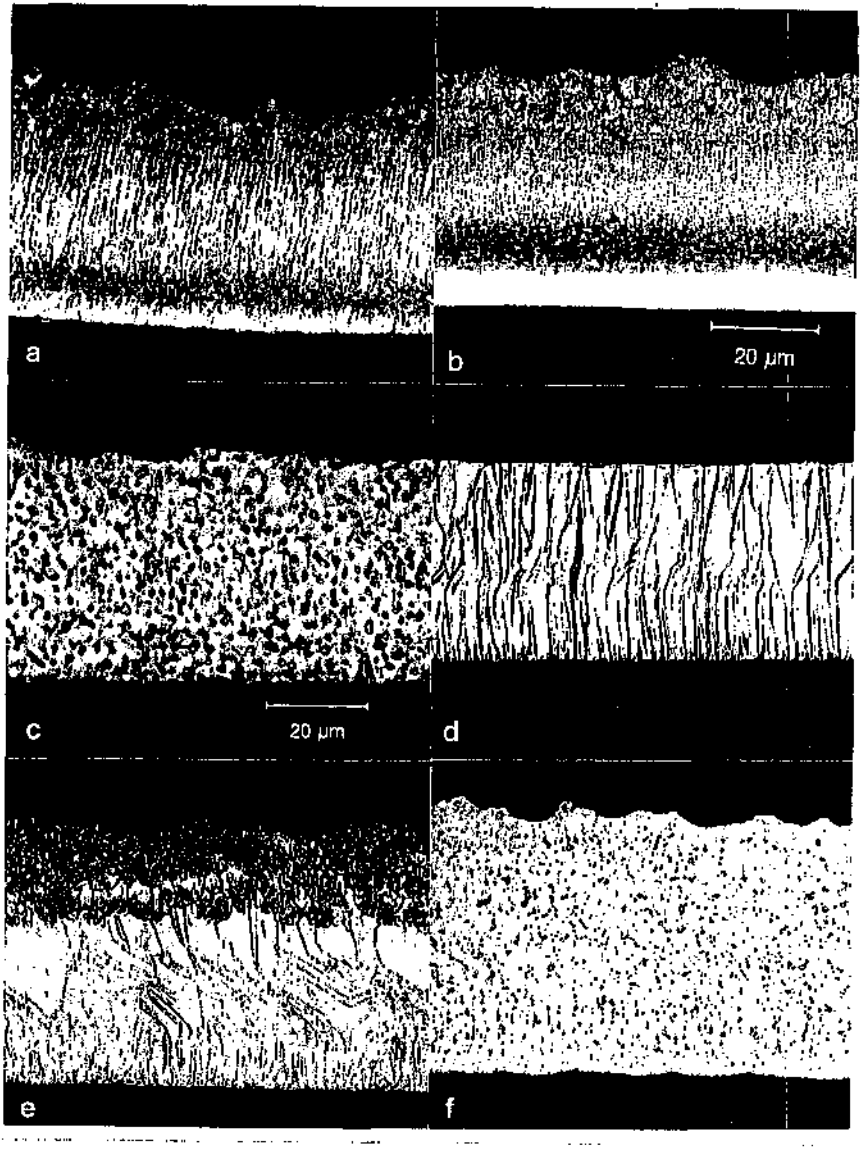

Figure IV.2 Transverse optical microstructure of copper-yttrium and copper-zirconium ribbons before and after heat treatment. (a) Cu-Y0.7 at% and (b) Cu-Y1.5 at% ribbons cast at 43 ms^{-1}, their microstructure consisted of three zones. Upon heat treatment (c) (800°C, 30 min) the microstructure coarsened rapidly to large grains of copper and copper-yttrium intermetallic. (d) As cast Cu-Zr0.33 at% and (e) Cu-Zr0.55 at% ribbons spun at 36 ms^{-1}. Copper-zirconium intermetallic particles could be seen after heat treatment of the Cu-Zr0.55 at% ribbon for 30 min at 800°C (f).

particles were clearly seen at the grain boundaries, but they did not coalesce at the same rate as for the yttrium-containing ribbons. Figure IV.2.f shows the optical microstructure of the Cu-Zr0.55 at% ribbon cast at 36 ms^{-1} heat treated at 800°C for 30 min. The grain size was not altered by heat treatment as the intermetallic particles were pinning the grain boundaries. After heat treatment, as in the copper-yttrium ribbons, no obvious distinction between the different portions of the ribbon could be seen. For all the chromium-containing ribbons heat treatment resulted in precipitation and the growth of chromium particles. They were found uniformly distributed within the grains and along the grain boundaries (figure IV.1.d). Similarly, as in the zirconium-containing ribbons, the grain size was unaltered by heat treatment due to the presence of particles at the grain boundary inhibiting grain growth.

4.1.2 Boron-containing alloys

Copper-chromium-boron, copper-cobalt-boron and copper-iron-boron alloys showed liquid phase immiscibilities during the attempt to cast the ingots. During fusion a liquid rich in boron floated in the melt. Near the bottom of the same ingot the volume fraction of second phase detected was noticeably less. This was because the solute rich phase flocculated near the top of the ingot during fusion. Since the melt spinning process requires a homogeneous liquid, these alloys were not melt spun.

Ingots of copper-zirconium-boron and copper-titanium-boron showed a uniform distribution of second phase particles before melt spinning. These alloys were melt spun. The as cast microstructures of the ribbons obtained are shown in figure IV.3. Columnar grains with coarse diboride particles either uniformly distributed (TiB_2 in figure IV.3.a) or floating on the top surface of the ribbon (ZrB_2 in figure IV.3.b) were observed. The size and distribution of these particles suggested that before casting, the boride phase was undissolved. At the moment of ejection, where the temperature was kept near 1500°C, (this value is approximate because the temperature was not monitored during the melt spinning process, *cf.* section 3.2, page 31) the melt consisted of a suspension of boride particles in liquid copper. Titanium and zirconium diboride particles proved therefore to be hardly soluble in copper near 1500°C. Furthermore, the analysis of the volume fraction of second phase particles present in the as cast state suggested that the extent of solid solution extension of the diborides in these ribbons was negligible. The limited volume fraction of useful dispersoid made these alloys uninteresting for further study.

Transverse optical microstructures of ribbons of copper-boron and copper-yttrium-boron before and after heat treatment are shown in figure IV.4. The as cast microstructures were sensitive to boron concentration, but were uninfluenced by the presence of yttrium as a ternary addition. For ribbons with

boron contents above 3 at%, a "structureless zone" (at this level of examination) could be seen on the wheel contact side in one quarter of the total ribbon thickness. The remaining thickness of the ribbon, for both the dilute and concentrated boron alloys, consisted of columnar grains, extending to the top of the dilute ribbons (figure IV.4.a) and close to the top of the concentrated ones (figure IV.4.b). For melt spun ribbons with high boron contents, the top region was characterized by an equiaxed microstructure. Because of its rather small and irregular nature, no particular study of its structure or stability was carried out.

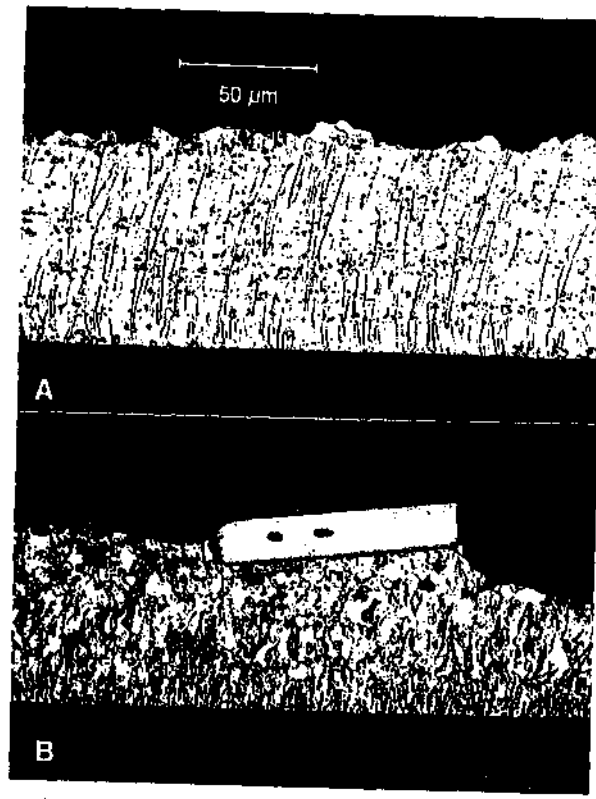

Figure IV.3 Optical microstructure of as cast copper-zirconium diboride (a) and titanium diboride (b) ribbons melt spun at 26 ms^{-1}. The melt ejection temperature was close to 1500°C, however, due to the insolubility of the diborides the volume fraction of soluble boride was limited, as can be seen by the coarse distribution of particles throughout the ribbon or on its surface.

Casting the binary Cu-B2.7 at% alloy at speeds ranging from 11 to 43 ms^{-1} showed a transition in the microstructure obtained. Optical examination of the as

cast state showed no second phase particles for ribbons cast at speeds above 20 ms^{-1}. The microstructure consisted of columnar grains approximately 1 μm in width extending throughout the ribbon thickness as in figure IV.4.a. Casting the same alloy at slower speeds resulted in a coarser structure with boron particles uniformly distributed within copper grains 3-5 μm in size (figure IV.4.c).

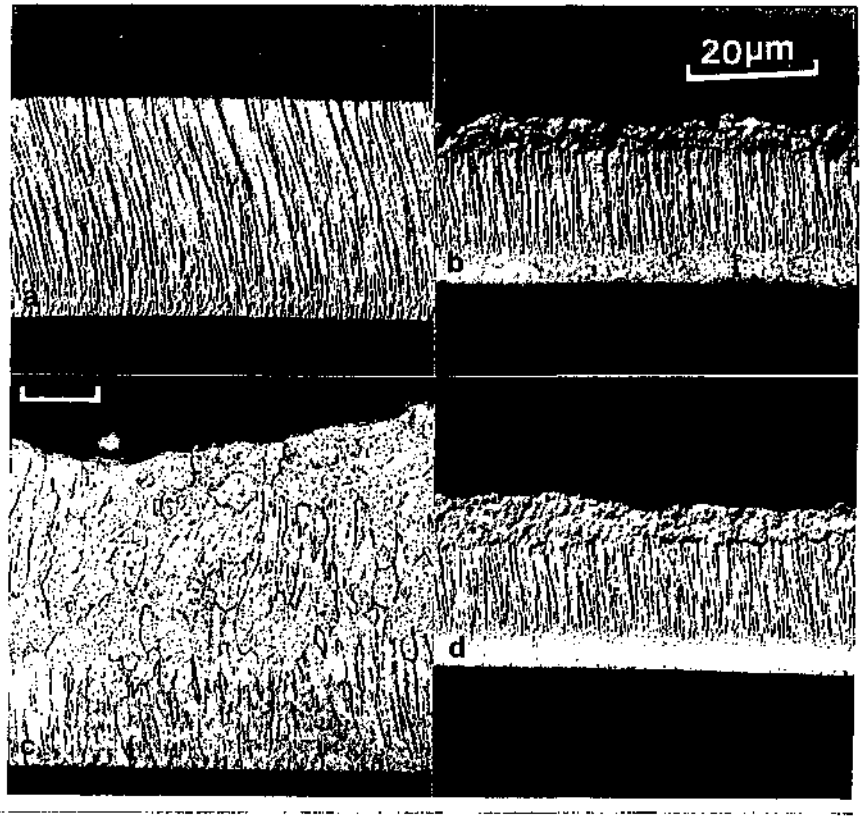

Figure IV.4 Optical micrographs of transverse sections in copper-boron and copper-yttrium-boron ribbons cast at different speeds or after heat treatment. (a) As cast Cu-B2.7 at%, 43 ms^{-1}, the microstructure consisted of columnar grains. (b) Structureless, columnar and equiaxed zones of as cast Cu-B7.3 at%, 43 ms^{-1} (c) Cu-B2.7 at%, 11 ms^{-1}, the as cast microstructure contained boron-rich particles. (d) As cast Cu-Y0.23 at% B5.66 at%, 36 ms^{-1}, similar zones are found as in (b). (Micron marker in (c) represents 20 μm, other micrographs have the same scale.)

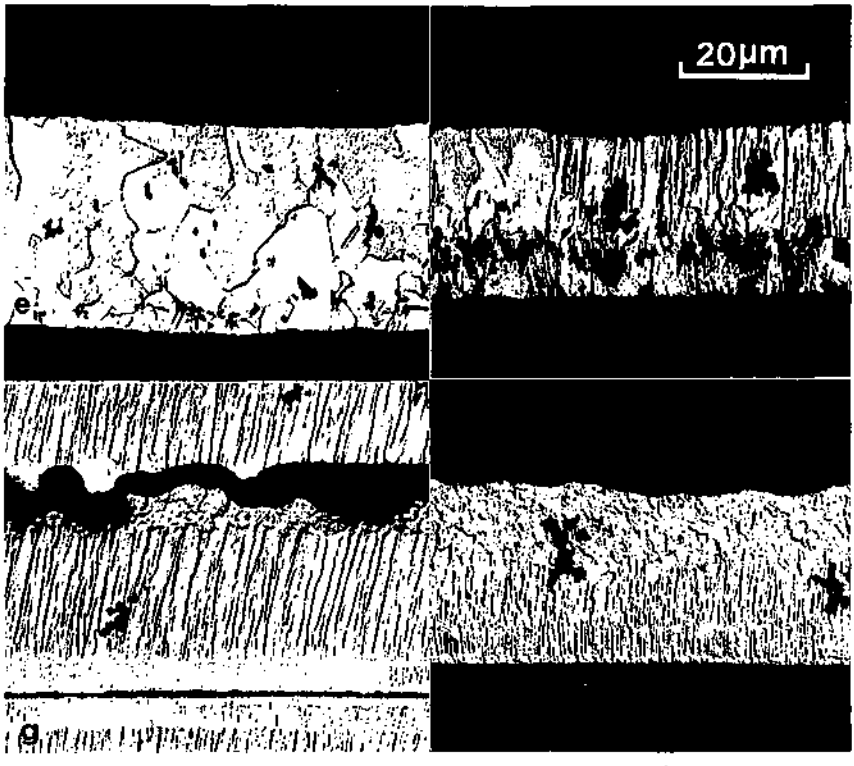

Figure IV.4 (Continued) After heat treatment (800°C, 30 min) Cu-B2.7 at% (e) and Cu-B7.3 at% (f) large boron crystals appeared preferentially near the wheel contact side. Grain growth was slower and the number density of the boron crystals less for the Cu-Y0.23 at% B5.66 at% ribbons, heat treatment: (g) 800°C, 30 min and (h) 24h.

After annealing for 30 min, ribbons containing boron spun at 43 and 36 ms^{-1} in the temperature range of 300-700°C exhibited no observable change in microstructure. At higher temperatures large boron crystals appeared (figure IV.4.e,f, g and h). Rapid growth of these particles followed. Their number was noted to be far greater in the binary alloys than the ternary yttrium-containing compositions for similar concentrations of boron. Yttrium addition appeared to decrease the number density of boron particles. In the case of copper-boron ribbons, the appearance of these crystals was followed by copper grain growth in the vicinity of the particle. Figure IV.5 shows a scanning electron micrograph (back scattered electron contrast) of a heat treated Cu-B2.7 at% ribbon. Copper grain

growth occurred in the regions surrounding the large boron particle, resulting from a depletion of grain boundary pinning particles. At a certain distance from the large particle no growth occurred and the grain size remained constant. No such localized copper grain growth was observed in the yttrium-containing alloys, possibly due to the existence of a second more stable grain boundary pinning phase (figure IV.4.g and h). For all the boron-rich ribbons, there is a clear tendency for crystal formation preferentially in the near wheel zone (figure IV.5.f). This is less evident in the ternary alloys because of the much smaller number density of crystals (figure IV.4.g).

In summary the rapid solidification of boron-rich ribbons was characterized by the total absence of microstructural change on annealing until a certain time-temperature treatment is attained. Thereafter microstructural breakdown of the rapidly solidified state occurred. This was demonstrated by the appearance and rapid growth of boron-rich crystals near the wheel side of the ribbon, resulting in general microstructural coarsening and leading to the breakdown of the rapidly solidified state. Both the time before the appearance of the first boron crystal as well as the rate at which the breakdown occurred were of interest, since these parameters determined the microstructural stability of the rapidly solidified state.

As described in section 3.7.1, page 36, the size of a boron crystal was determined from the diameter of the circle encompassing the particle. The size distribution, surface area fraction (equal to volume fraction) and planar number density of the boron particles were measured for each of the heat treated samples. Initially the volume fraction of particles increased eventually reaching the predicted values as determined by the composition (4$^{vol\%}$ and 1.5$^{vol\%}$ for the Cu-B7.3 $^{at\%}$ and Cu-B2.7 $^{at\%}$ ribbons, respectively). Upon further annealing, the size of the crystals increased by coarsening, the volume fraction remaining constant. The volume size distribution was obtained from the number of particles per unit area and the planar size distribution, using the Schwartz-Saltykov mathematical treatment [122]. Figure IV.6 shows both the planar and volume size distributions of boron particles obtained in the Cu-Y0.23 $^{at\%}$ B5.66 $^{at\%}$ ribbon. For the states shown, the volume fraction of crystalline boron was increasing. During this period the volume size distribution was narrow, and approached a monosized distribution. For small particle sizes, the volume number density was negligible, which suggested that the formation of these crystals was not a continuous process, as would be expected by classical nucleation, precipitation and growth. The density of particles remained invariant during this initial period where the volume fraction of boron particles increased, indicating that most of the boron particles appeared simultaneously and grew at the same rate. Therefore, if viewed in three dimensions and not as a metallographic section, all the particles would have approximately the same size during this transient period. For this reason the particle size recorded for each heat treated state was the maximum diameter of the encompassing circle found in each sample.

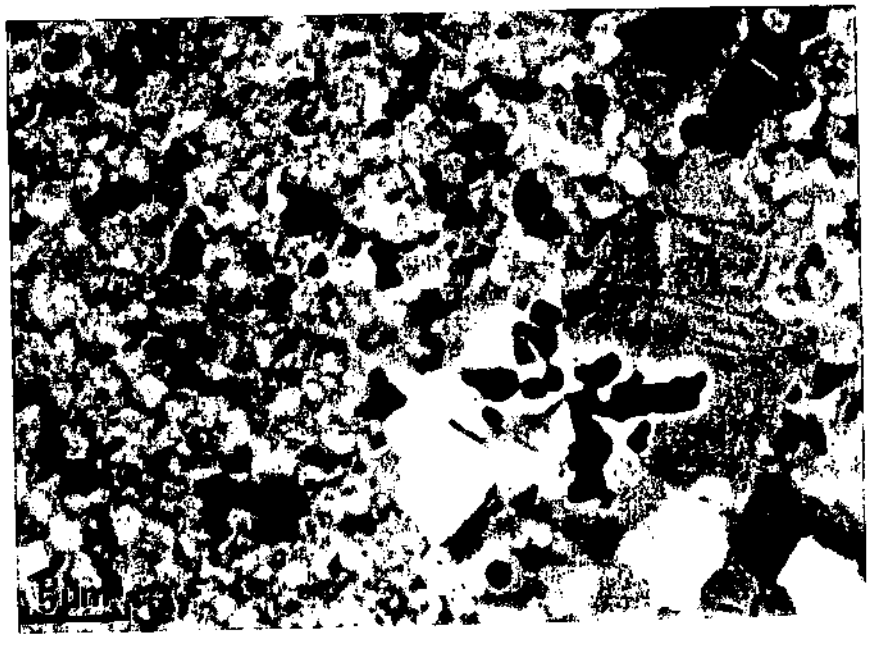

Figure IV.5 Scanning electron micrograph (back scattered electrons) of a Cu-B2.7 ^{at}% ribbon heat treated at 750°C for 30 min. Copper grain growth can be clearly seen around each boron crystal.

The influence of casting speed on the number of crystals forming upon heat treatment in the binary Cu-B 2.7^{at}% ribbons is shown in figure IV.7. The range of speeds used gave ribbons of thicknesses varying from 120 µm at 11 ms^{-1} to 30 µm at 43 ms^{-1}. For wheel speeds above 20 ms^{-1}, the ribbons exhibited, upon heat treatment, the microstructural instability described earlier. In view of the constant volume number density of boron particles during the period of transformation, only one heat treatment was needed to determine the number density of crystals at each casting speed. A heat treatment of 750°C for 22 min was chosen. The volume fraction of boron particles observed after this heat treatment was less than expected for 2.7 ^{at}% boron in all the ribbons, since the transformation was incomplete. At very low casting speeds (11 ms^{-1}) boron-rich particles could be seen in the as cast state and no microstructural instability was observed upon heat treatment. At faster quench rates, the number density of boron crystals increased with increasing casting speed. Since all the boron particles had the same growth rate, increasing the number of particles decreased the time for transformation. This, in consequence, decreased the thermal stability of the rapidly solidified state.

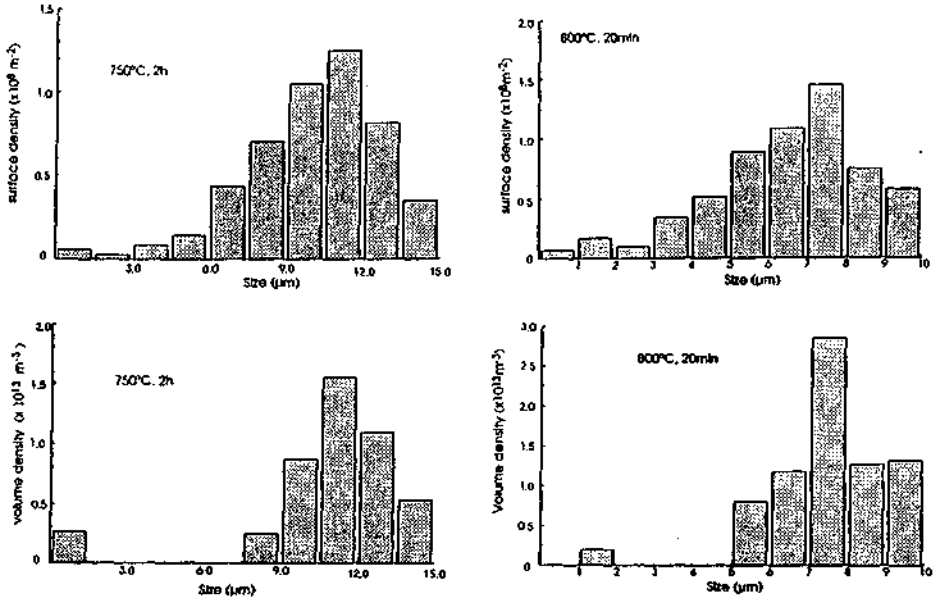

Figure.IV.6 Planar and volume distributions of boron particles in the Cu-Y0.23 at% B5.66 at% ribbon. The volume size distributions were obtained by the Schwariz-Saltykov method.

Due to the smaller number density of crystals which appear after aging in the Cu-Y0.23 at% B5.66 at% ribbon, the transformation occurred at a slower rate relative to the binary alloy (142 h and 30 min at 750°C for total transformation for the Cu-Y0.23 at% B5.66 at% and the Cu-B7.3 at% ribbons respectively). The growth of the large boron crystals is shown in figure IV.8 where the estimated time, ξ, necessary to transform all the boron of the alloy into large crystals is given. It is clear that this time interval is a measure of the thermal stability of the boron-containing alloys and is much shorter in the binary than in the ternary ribbon. For this reason the rate of growth of the crystalline boron phase during the period of increasing volume fraction was studied in the yttrium-containing alloy.

After total transformation, the coarsening of the boron crystals was also studied. This was carried out in the binary Cu-B7.3 at% ribbon spun at 43 ms^{-1} where the number of crystals was higher, permitting better quantification of the coarsening rate. Figure IV.8 shows the growth of these particles during both the transient period of variable increasing fraction and the coarsening stage where the

volume fraction of boron particles was constant. The passage from one stage to the next is indicated by ξ. The addition of yttrium decreased the number density of boron particles formed on heat treatment. The time of transformation was noticeably increased, improving the overall stability of the material.

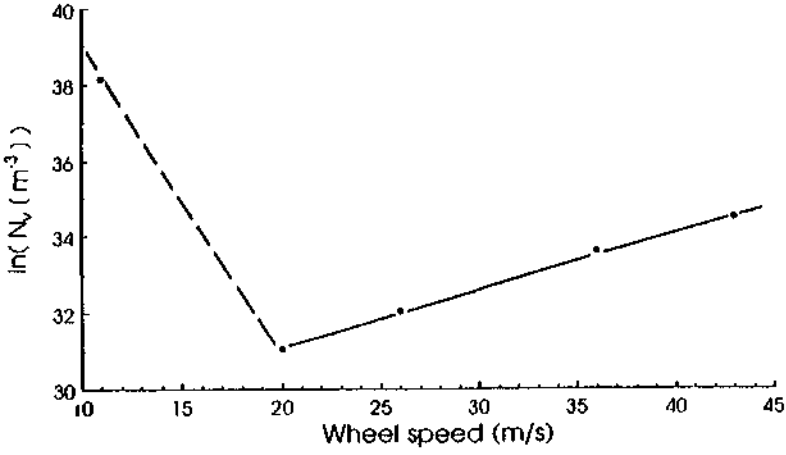

Figure IV.7 Variation of volume number density of boron crystals with casting speed in heat treated (750°C for 22min) Cu-B2.7 at%. The high number density at 11 ms^{-1} is due to preexisting boron particles in the ribbon.

Copper-nickel-boron ribbons were cast at 36 ms^{-1}. The optical microstructures of the as cast state consisted of columnar grains, one micron in width, extending from the wheel to the free surface, as shown in figure IV.9. Upon heat treatment, and depending on the composition, either a) a uniform distribution of fine boride particles was found (figure IV.9.b), (for alloys close to a nickel : boron ratio of 3:1) or, b) a bimodal distribution of particles consisting of fine boride particles similar to the latter, and coarse boron particles as observed in the binary copper-boron ribbons after heat treatment (for ribbons where the nickel to boron ratio was less than 3:1), were found (figure IV.9.c). The phases observed after heat treatment were in agreement with the ternary copper-nickel-boron isotherm established by Lugscheider [120] where boron and Ni_3B were found to be in equilibrium with copper in the copper corner of the ternary diagram.

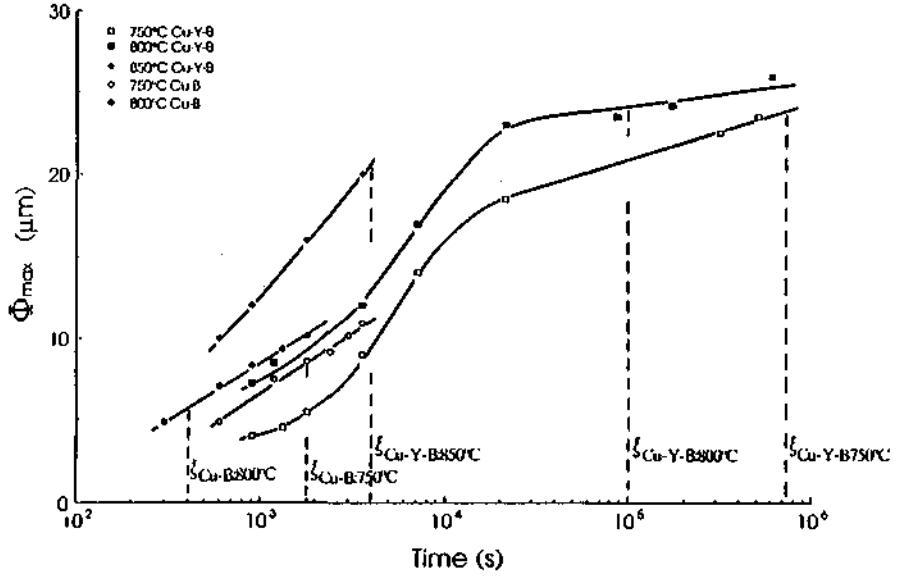

Figure IV.8 Variation of size, Φ_{max}, of the boron crystals as a function of time for different heat treatments in Cu-B7.3 at% and Cu Y0.23 at% B5.66 at% ribbons. ξ is the estimated time when the transformation of boron into large crystals is completed.

4.2 Mechanical properties

Melt spun ribbons produced as described in section 3.2, page 30, were generally of sufficient quality to enable tensile testing without preliminary preparation. After 30 min heat treatments in the range 400°C to 800°C, at 100°C intervals, the flow, maximum stress and elongation to failure were determined. The value of flow strength at 0.2% strain was reproducible with an error of approximately 2.5%. This reproducibility was associated with the good ductility and strong work hardening characteristics of the dilute copper alloys which restrict the influence of flaws in the ribbon geometry. However, the elongation to failure was less reproducible, since these values were sensitive to such microscopic defects. The following sections summarize the tensile and microhardness properties of the boron-free and containing ribbons.

4.2.1 Boron-free alloys

Figure IV.10 shows the evolution of the flow strength of binary copper-calcium, cerium and yttrium ribbons after 30 min anneals. The concentrated copper-cerium

and yttrium ribbons having approximately 10 vol% of second phase (deduced from chemical analysis and the molar volumes of the intermetallics) showed no ductility in the as cast state and after annealing up to 500°C. At higher temperatures, their ductility increased. The less concentrated copper-yttrium ribbon (approximately 5 vol% of second phase) was ductile in the as cast state and had a flow stress of 370 MPa. No age hardening within the time temperature range tested was observed for all the ribbons. The concentrated ribbons were characterized by a rapid drop in strength when compared to the dilute alloys.

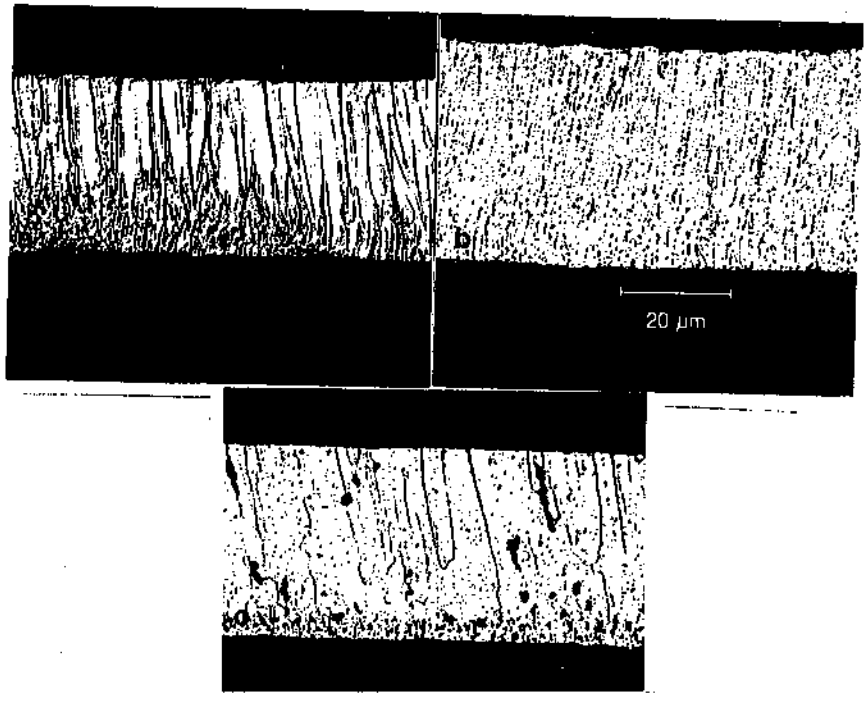

Figure IV.9 Optical microstructure of as cast and heat treated copper-nickel-boron ribbons. (a) As cast Cu-$(Ni_3B)_{0.6}$ consisting of columnar grains. After annealing at 800°C for 30 min, fine boride particles appeared (b). Cu-Ni1.01 at% B3.05 at% ribbon after annealing at the same temperature and time showed Ni_3B [120] and large boron particles (c).

The evolution of microhardness with temperature, for the wheel and the free surface of the Cu-Y0.7 at% alloy, melt spun at 43 ms^{-1}, is shown in figure IV.11. Slight age hardening after annealing at 300°C for 30 min is observed in the rapidly quenched wheel side. The free surface showed no age hardening and was generally softer. These measurements confirmed the optical microstructural observations where it was suggested that possible solid solution extension could be achieved near the wheel contact side. The top portion of the ribbon showed a clearly

segregated microstructure, which explains the lower microhardness measurements. Above 600°C the difference in hardness between the wheel and the free surfaces are lost. The hardness values decreased rapidly with heat treatment to levels approaching values characteristic of annealed pure copper. Due to the similarities in the evolution of strength and microstructure with temperature for the copper-calcium and cerium ribbons to the copper-yttrium ribbons, the latter was taken as representative of the other two.

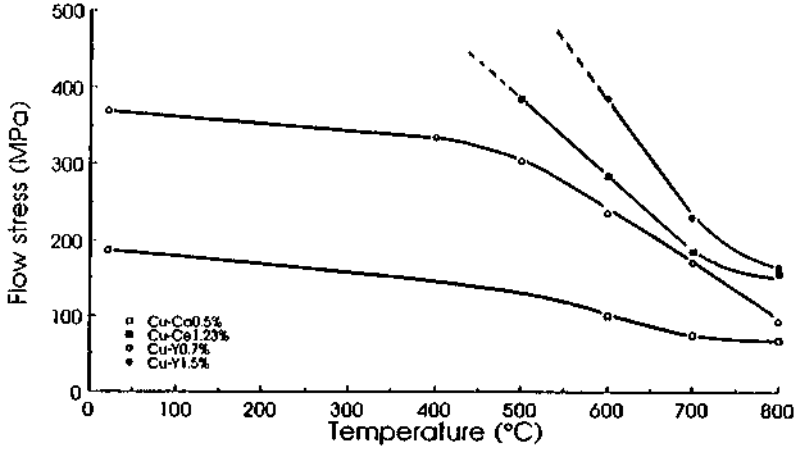

Figure IV.10 Flow stress of copper-calcium, cerium and yttrium ribbons spun at 43 ms^{-1} after annealing for 30 min. The concentrated ribbons were characterized by a rapid drop in strength.

Figure IV.12 shows the flow strength of copper-zirconium ribbons cast at 36 ms^{-1} after annealing for 30 min. It can be seen that for all the ribbons age hardening occurred near 400°C. The increase in as cast strength with concentration (215, 310 and 455 MPa for the 0.33 at%, 0.79 at% and 1.7 at% zirconium ribbons respectively) suggested that throughout the thickness of the ribbon, for a casting speed of 36 ms^{-1}, a limited solubility extension of zirconium was possible, the extra solute being present as second phase particles. The increase in strength as a result of precipitation (approximately 175 MPa) was similar for all the ribbons, suggesting that similar amounts of supersaturation were achieved. This finding confirmed the optical microstructural observations which suggested that the extent of solid solution extension of zirconium was limited to about 0.33at% by melt spinning.

The mechanical properties of the copper-chromium ribbons were characterized by strong age hardening. Peak ageing was obtained after annealing

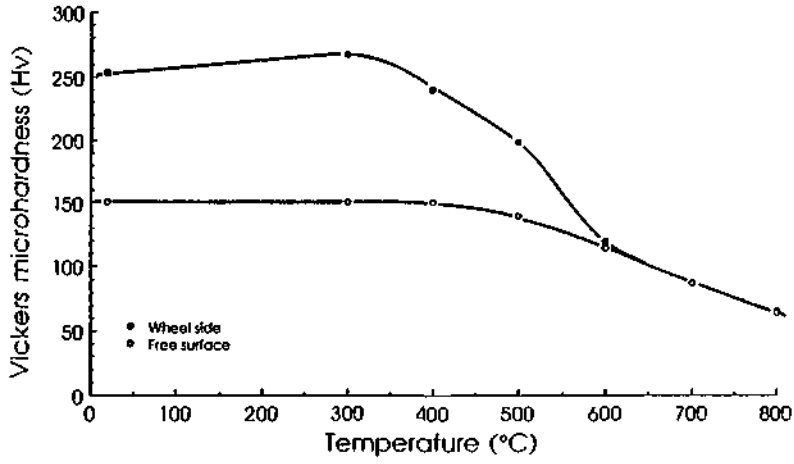

Figure IV.11 Microhardness (load 25 g)of the wheel and free surface after annealing for 30 min in Cu-Y0.7 at% spun at 43 ms^{-1}. The wheel contact side shows slight solid solution extension as reflected by the age hardening peak.

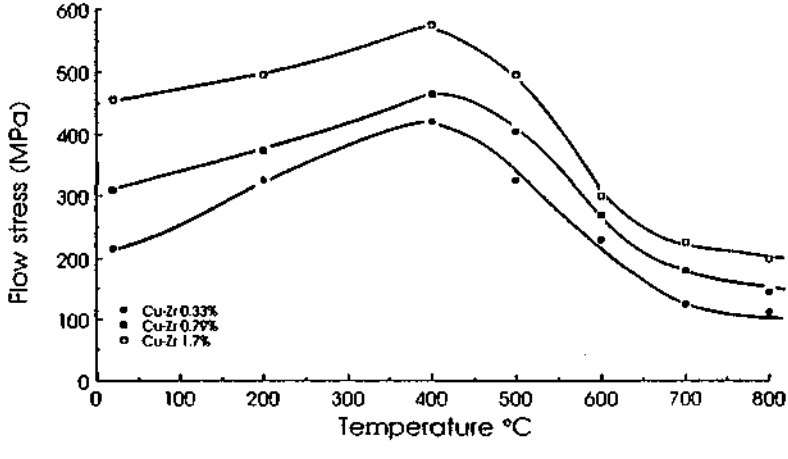

Figure IV.12 Flow strength of copper-zirconium ribbons after annealing for 30 min. The age hardening observed suggests some solid solution extension of zirconium.

at 500°C for 30 min. For the three ribbons the increase in strength observed with annealing temperature was accompanied by a decrease in ductility until the peak

aging temperature was reached. Further annealing resulted in a decrease in flow strength coupled with higher work hardening rates and ductilities. The binary alloys had as cast strengths of 190±5 MPa for the Cu-Cr1.85 at% and Cu-Cr2.54 at% ribbons. The cast strength of the Cu-Cr5.0 at% ribbon was higher, being 360 MPa. On aging to maximum strength, an increase of 305, 345 MPa and 325 MPa was obtained for the Cu-Cr1.85 at%, Cu-Cr2.54 at% and Cu Cr5 at% ribbons respectively. This strong age hardening suggests that a considerable amount of chromium was put into solution by rapid solidification. By heat treatment this excess solute precipitated as a fine dispersion causing the observed increase in strength. Figure IV.13 shows the variation of strength with temperature for the three binary ribbons tested. The gain in strength upon aging to peak strength is similar, suggesting that the extent of excess solute trapped for the three ribbons was comparable. The Cu-Cr1.85 at% and Cu-Cr2.54 at% probably had the chromium in solid solution, while the Cu-Cr5 at% ribbon had approximately 2.5 at% of chromium in solid solution, the rest present as second phase particles in the as cast state.

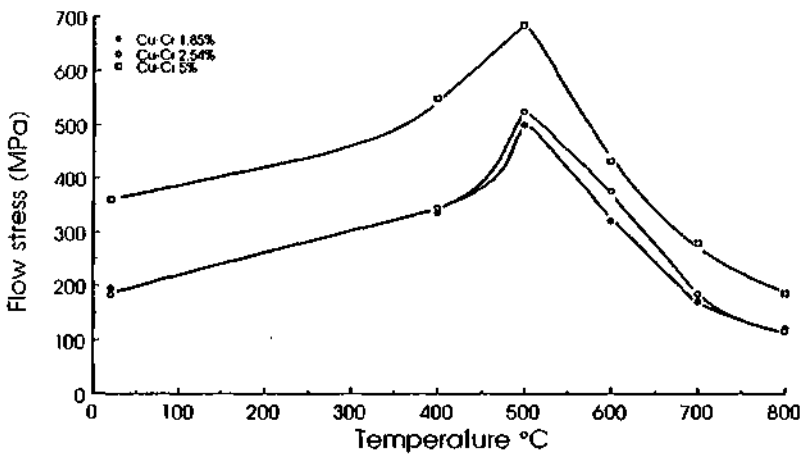

Figure IV.13 Variation of flow stress with annealing temperature (30 min) for the copper-chromium alloys.

Ternary copper-chromium-zirconium alloys were studied because of the possible solid solution extension for both the chromium and zirconium solutes. A large number of ternary compositions were melt spun at 26 ms^{-1} in order to optimize the mechanical properties with respect to chemical composition. The concentrations of alloying elements ranged from 2-3 at% chromium and

0.2-1.0 at% zirconium. Only alloys with concentrations of chromium less than 3 at% were studied, since earlier studies have shown that the maximum solid solubility extension of chromium was limited to this value by melt spinning.

Figure IV.14 shows the variation of flow strength for ternary copper-chromium-zirconium ribbons containing approximately 2.5 at% chromium as a function of zirconium content after 30 min anneals. The flow stress of the as cast material increased with zirconium content which suggested that not all the zirconium was put into solid solution, an increasing amount present in the matrix as second phase particles after rapid solidification. The effect of zirconium on the age hardening of the binary alloy is clearly seen by the substantial increase in strength obtained between the binary alloy and by an addition of approximately 0.3 at%. Further additions of zirconium showed no further improvement in properties. Similar behaviours were observed for other fixed levels of chromium.

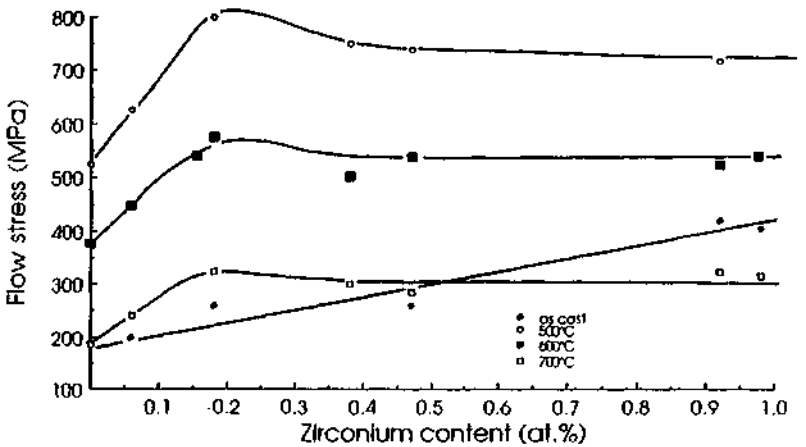

Figure IV.14 Variation of flow strengths as a function of zirconium content in ternary copper-chromium-zirconium ribbons melt spun at 26 ms^{-1}. The chromium content was fixed close to 2.5 at%. The addition of small quantities of zirconium (up to 0.3 at%) increased the strength of the alloy, additions above 0.3 at% did not contribute to further strengthening.

The evolution of strength with chromium content at fixed levels of zirconium was somewhat different (figure IV.15). For the different concentrations of chromium no noticeable increase in strength was observed in the as cast state, demonstrating that all the chromium was in solid solution. Upon annealing the strength of the ribbons increased with chromium content in a monotonic manner. These

observations showed that highest strengths were obtained by melt spinning for copper-chromium-zirconium compositions close to 0.3 at% zirconium and 2-3 at% chromium. The kinetics of the evolution of the microstructure of the Cu-Cr2.2 at% Zr0.2 at% ribbon was examined in further detail.

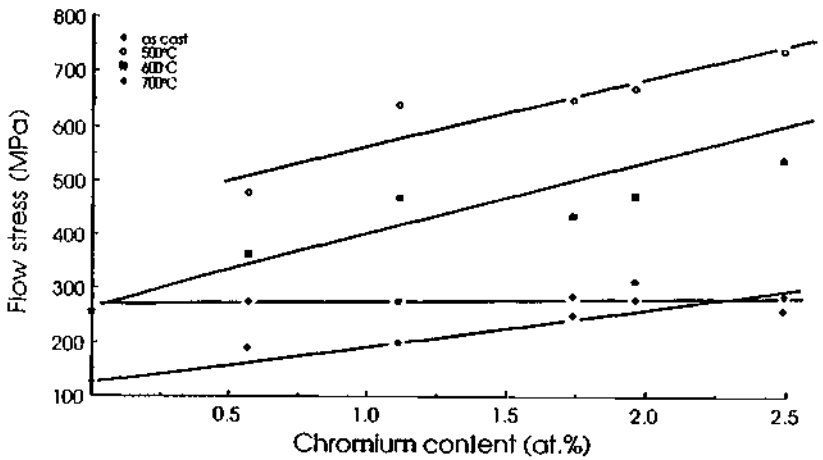

Figure IV.15 Variation of flow strength as a function of chromium content in ternary copper-chromium-zirconium ribbons melt spun at 26 ms^{-1}. The zirconium concentration was close to 0.5 at%. Chromium additions up to 3 at% increased the strength of the alloy.

Because of the interesting properties of rapidly solidified chromium based alloys, other ternary additions were made to alloys containing approximately 2 at% chromium. These additions were intended to modify either the precipitation or the coarsening mechanisms of the alloy as has been done in other precipitation or dispersion hardened systems [10-13, 121-124], with a view to understanding their effects on thermal stability or strength. Titanium, magnesium and silicon were added in concentrations not exceeding 0.3 at%. These elements were selected because of their differences in size and electronegativity with respect to copper. In order to determine how the extra solute intervened, and if a modification in behaviour with respect to the binary alloy was observed, the solute concentration was limited to 0.3 at%, less than the maximum solid solubility of the added element in copper. These elements are essentially insoluble in chromium. Silicon was considered a control element, for its difference in electronegativity and size with respect to copper were negligible. Magnesium, titanium and zirconium are all electropositive with respect to copper, magnesium and zirconium being more so

than titanium. Similarly, magnesium, titanium and zirconium have larger atomic radii than copper, and magnesium and zirconium are larger than titanium.

Table IV.1 shows compositions and volume fractions of chromium in the ribbons cast as well as the values of flow strength as a function of isochronal annealing temperatures. The alloys were intended to have approximately 2 vol% of chromium particles. The fluctuations observed are due to experimental variations during alloy preparation. In the as cast state the flow strength of all the ribbons was close to 200 MPa. On annealing, the strength increased to a maximum after heat treating at 500°C. Further annealing decreased the flow stress by over aging. The maximum effect of the solute additions to the binary alloy can be seen near the peak aged state. Compared to the binary alloy, zirconium and magnesium seemed to be effective alloying additions, while titanium proved detrimental to the resultant mechanical properties of the rapidly solidified material. Silicon additions did not seem to affect the mechanical properties of the ribbons.

Table IV.1 Flow strengths in MPa for the various ternary copper-chromium-metal ribbons after 30 min heat treatments.

Composition	f_v(%) of Cr part.	As cast	400°C	500°C	600°C	700°C	800°C
Cr1.85 at%	1.91	195	335	500	320	170	120
Cr2.19-Zr0.18 at%	2.22	230	460	700	500	305	185
Cr2.44-Mg0.19 at%	2.53	205	335	670	415	230	130
Cr2.37-Ti0.06 at%	2.46	205	320	515	445	205	135
Cr2.22-Ti0.11 at%	2.30	230	275	440	330	190	120
Cr2.41-Si0.23 at%	2.50	220	320	615	380	225	140

4.2.2 Boron-containing alloys

Figure IV.16 shows the evolution of microhardness with annealing temperature (30 min) for the wheel and free surfaces of the Cu-B2.7 at% and the Cu-B7.3 at% ribbons spun at 43 ms^{-1}. The existence of two different microstructures in the ribbons, as was observed optically, was confirmed by these microhardness measurements. It can be seen that the hardness of the wheel side is greater at all temperatures than the free surface hardness. Age hardening occurred after a heat treatment of 30 min at 300°C, which suggested that boron supersaturation was achieved particularly on the wheel contact side of the ribbon. Hardening was much more pronounced in the concentrated Cu-B7.3 at% ribbon. This difference in hardening observed between the concentrated and dilute alloys would suggest that the solid solubility of boron was extended to above 3 at%. After peak aging above 400°C the microhardness fell as the age hardening effect was lost. The hardness thereafter remained steady up to 700°C where a final drop occurred. This drop corresponded with the appearance of the large boron crystals which coarsened resulting in the breakdown of the rapidly solidified microstructure.

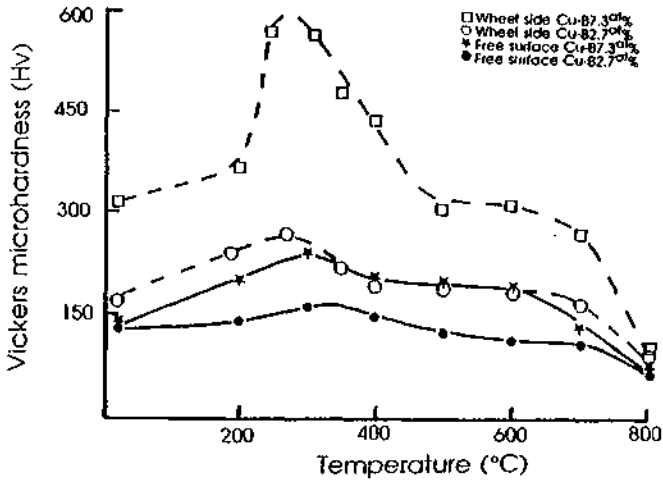

Figure IV.16 Variation of microhardness (load 15 g) with annealing temperature for the binary Cu-B2.7 at% and Cu-B7.3 at% ribbons spun at 43 ms^{-1}. The wheel side microhardness is substantially greater than the free surface.

The variation of peak hardness with casting speed is given in figure IV.17 for the Cu-B2.7 at% ribbon. As shown by the drop in peak hardness with decreasing wheel speeds the faster quench rates increased the concentration of boron put into solid solution. Both the number density of crystals (figure IV.7) as well as the extent of solubility extension increases with increasing wheel speed, suggesting that the number of boron crystals formed during the microstructural instability is directly related to the extent of solid solution extension in the wheel contact side of the ribbon.

The mechanical properties of the copper-boron and copper-yttrium-boron alloys spun at 36 ms^{-1} are compared in figure IV.18. Peak aging is less clearly visible by tensile testing as compared to local microhardness measurements. This was probably due to the narrow zone over which the solid solution extension occurred. In addition the tensile tested samples were annealed at higher temperatures where the samples were over aged. Ternary boron-rich ribbons retained their good mechanical properties up to high temperatures, while the strength of the binary ribbons fell significantly after anneals above 700°C.

Figure IV.19 shows the evolution of the flow strength of the Cu-Y0.18 at% B2.3 at% ribbon after annealing. In comparison with all the other ribbons of this study, the drop in strength with annealing time at 700 and 800°C is less. Anneals for several hours at 900°C are necessary to bring the initial strength

from approximately 500 MPa down to 200 MPa. As cast, the ribbon has a flow strength which is comparable to the concentrated copper-boron alloy. For this ribbon, as for other boron-rich ribbons, several hours at 600°C or minutes at 800°C, led to the appearance of crystalline boron particles. As a result of their rapid growth, a drop in strength was observed. However, further annealing was not followed by a continuous decrease in strength as in the case of the binary alloys. The retained strength was probably caused by yttrium-rich dispersions which coarsened slowly (this hypothesis is confirmed by microstructural observations presented later). In the as cast state the strength observed can therefore be attributed to a combination of the role of both the metastable boron and the yttrium-rich particles. After annealing, the drop in strength results from the transformation of the metastable boron to large particles which have little strengthening effect. However, because of the existence of a stable yttrium-rich dispersion, the strength of the ribbon decreased slowly thereafter. The as cast strengths are markedly influenced by the addition of small quantities of yttrium. For smaller concentrations of boron the mechanical properties of Cu-Y0.18 at% B2.3 at% are comparable to the concentrated Cu-87.34 at% ribbon. This was only valid for boron-rich compositions (figure IV.18). In contrast,

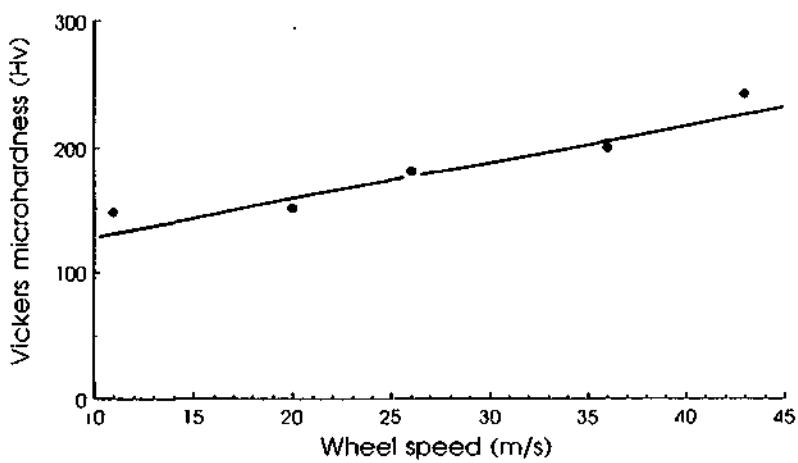

Figure IV.17 Wheel side microhardness (load 15 g) after peak aging of Cu-B2.7 at% ribbons as a function of casting speed. The hardness decreases with slower casting speeds, as the extent of solid solution extension of boron is decreased.

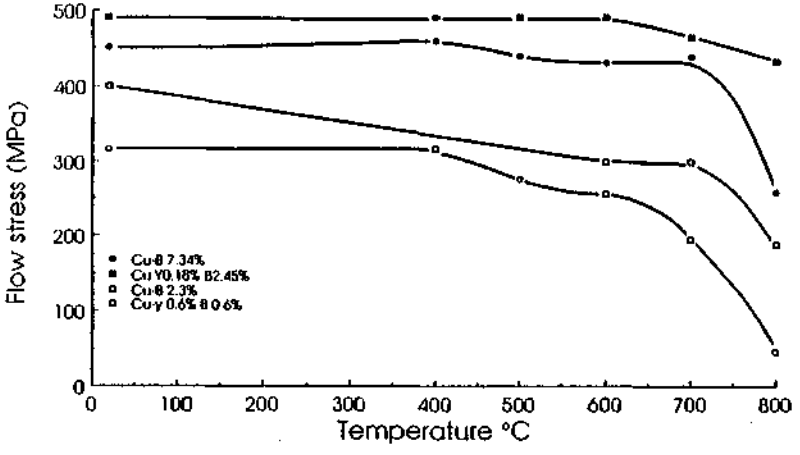

Figure IV.18 Flow strength of copper-boron and copper-yttrium-boron ribbons spun at 36 ms^{-1} as a function of annealing temperature (30 min).Cu-Y0.6 ^{at}% B 0.6^{at}% ribbons were only tested in the as cast state and at 600, 700 and 800°C.

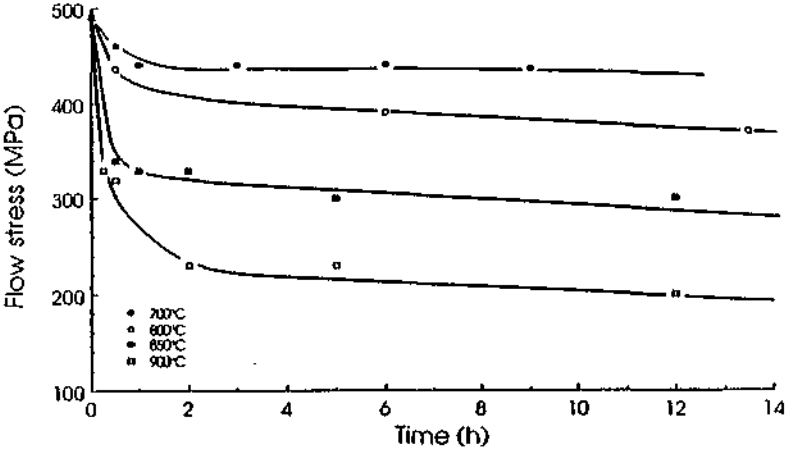

Figure IV.19 Flow strength of Cu-Y0.18 ^{at}% B2.3 ^{at}% ribbon after isothermal annealing. The stability of the rapidly solidified microstructure can clearly be seen.

for yttrium-rich alloys, where the ratio of yttrium to boron was approximately 1:1 a continuous decrease in strength with annealing temperature was observed (figure IV.18). When compared to the other ribbons, this ribbon behaves in a similar manner to the binary copper-yttrium ribbons where the strength monotonically decreased to similar values after heat treatment.

Figure IV.20 illustrates the mechanical behaviour of some of the copper-nickel-boron ternary ribbons after isochronal annealing. The as cast strength varies with the concentration of Ni_3B and is close to 850 MPa for a volume fraction of 13 vol% Ni_3B phase in the Cu-$(Ni_3B)_4$ alloy and drops down to 300 MPa for a volume fraction of 2 vol% Ni_3B phase in the Cu-$(Ni_3B)_{0.6}$ ribbon. No age hardening was observed for the concentrated alloys, however the small hardening peak observed for the Cu$(Ni_3B)_{0.6}$ ribbon after annealing at 500°C suggested slight solubility extension of nickel and boron. For the concentrated alloys the strength of the material began to drop after heat treatments above 400°C. The rate of decline in strength was greater in the concentrated ribbons.

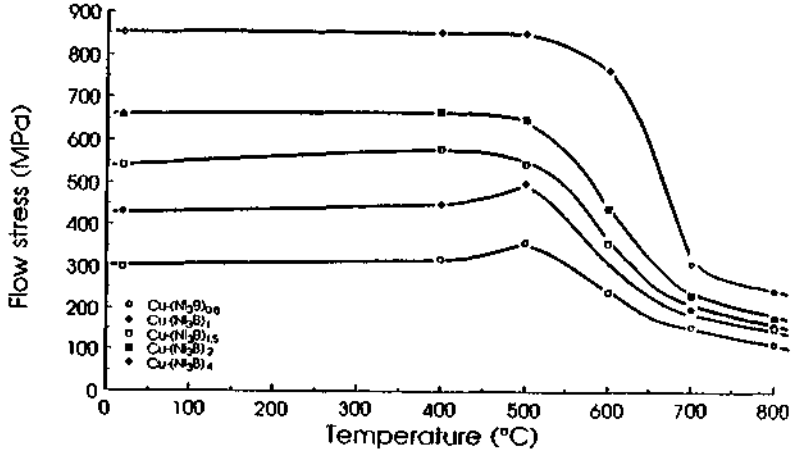

Figure IV.20 Evolution of flow stress of various Cu-Ni_3B ribbons after 30 min anneals. The least concentrated of the ribbons showed slight age hardening. All the alloys reached low values of strength after 700 to 800°C anneals.

4.3 TEM microstructural assessment

Transmission electron microscopy was widely used to characterize the initial rapidly solidified microstructure, dislocation density and nature of second phase particles present as well as the microstructural changes which occurred during annealing. Investigations were generally carried out by TEM at mid ribbon

thickness. For ribbons showing optically distinct wheel and free surface zones, the different portions of the ribbon were electrolytically thinned and the structural characteristics of each zone determined. The alloys chosen for examination were the copper-chromium, yttrium and zirconium and copper-chromium-metal, the copper-boron and copper-yttrium-boron compositions. The following sections summarize the results obtained by TEM observations of the boron-free and boron-containing ribbons.

4.3.1 Boron-free alloys.

TEM studies were carried out on Cu-Cr1.85 at% ribbons melt spun at different wheel speeds, Cu-Zr0.33 at% ribbon spun at 36 ms^{-1}, several ternary Cu-Cr2 at%-X0.3 at% alloys (where X=Zr, Ti, Mg, and Si) spun at 26 ms^{-1}, and finally on binary Cu-Y0.7 at% ribbon cast at 43 ms^{-1}.

Figure IV.21 shows the microstructure of as cast Cu-Cr1.85 at% rapidly solidified at different quench rates. Above wheel speeds of 16 ms^{-1} chromium solute is essentially in solid solution with a small volume fraction of chromium particles decorating the grain boundaries. For these different casting conditions, very small differences in grain size were observed the grain size being 1-2 μm. At quench rates lower than the casting speed of 16 ms^{-1}, chromium particles were present, either uniformly distributed throughout the interior of the grains with small particle-free zones at the grain boundaries (as in the ribbons spun at 8 ms^{-1}, figure IV.21.c) or arranged in a cellular manner (figure IV.21.d, for ribbons spun at the slower speed of 6 ms^{-1}). For the ribbon cast at 26 ms^{-1} no second phase particles were detected either within the grains or along the grain boundaries. A few randomly oriented dislocations were seen, with no tendency to form a cell structure. Using various diffraction vectors in order to avoid possible invisibilities of some dislocations, and estimating their total length in thick areas of the foil the dislocation density in the as cast state was estimated as $5x10^{13}$ m^{-2}. Detailed analysis of the kinetics of particle coarsening was carried out on this ribbon by prolonged isothermal heat treatment and quantification of chromium particle size. During coarsening of the chromium particles in the Cu-Cr1.85 at% ribbon spin at 26 ms^{-1}, particle free zones were found on either side of grain boundaries. These zones were found to increase in size, as the annealing time increased (figure IV.21.e and f).

Figure IV.22 shows the TEM observations of the microstructures in as cast Cu-Zr0.33 at% alloy melt spun at 36 ms^{-1}, and the change after heat treatment. Near the wheel side of the ribbon (figure IV.22.a) no second phase particles were present, showing that a supersaturation of 0.33 at% zirconium was achieved in this rapidly quenched region of the ribbon. The average grain size was approximately 0.5 μm. In the middle and top portion of the ribbon, the grain size was

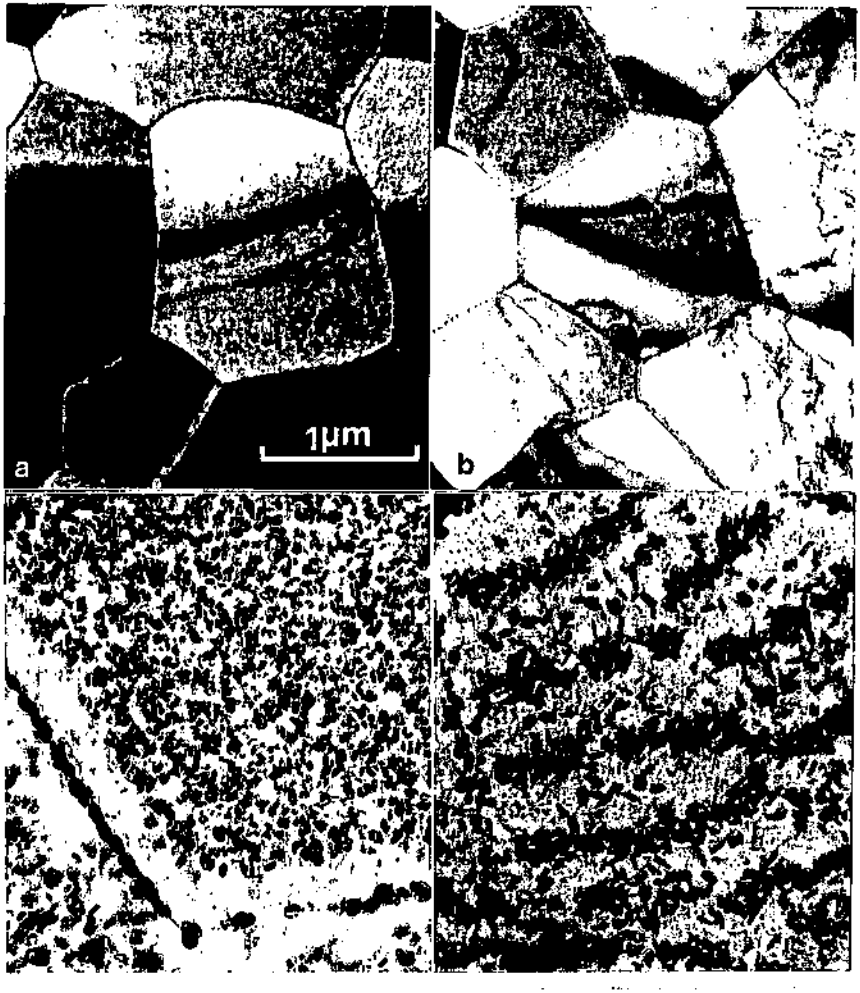

Figure IV.21 As cast microstructure of the middle of Cu-Cr1.85 ^{at}% ribbons cast at different wheel speeds. For wheel speeds of 16 ms^{-1} (a) and 26 ms^{-1} (b) the excess chromium solute is in solid solution. At wheel speeds of 8 ms^{-1} (c) and 6 ms^{-1} (d) chromium-rich particles are found.

noticeably larger. The grains contained zirconium-rich particles 40 nm in size arranged in a cellular manner (figure IV.22.b). The grain boundaries were also found to be decorated with similar particles. Precipitation and growth of the zirconium particles in the wheel side occurred upon heat treatment and after 30 min at 500°C, the particles 8 nm in size, were oriented along specific crystallographic

directions, as can be seen in figure IV.22.c. In the middle of the ribbon, the zirconium-rich particles also grew with heat treatment. Figure IV.22.d shows the typical lenticular shape the particles adopted. After 30 min at 600°C the zirconium-rich particles found in the grains increased to a diameter of 70 nm. The grain boundary particles were also found to coarsen.

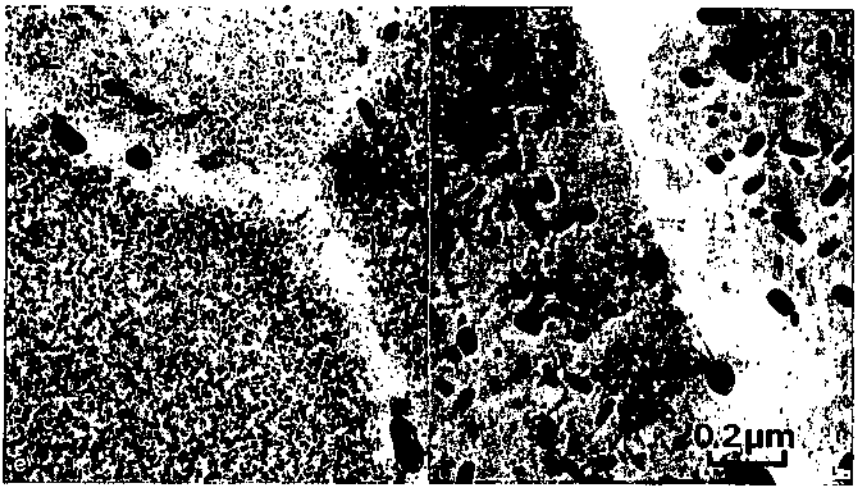

Figure IV.21 (Continued) (e) and (f) particle free zones present after annealing were found to grow with time (26 ms^{-1}, 600°C, 1h (e) and 3 days (f)).

Optically, no microstructural differences could be observed between the various ternary copper-chromium-metal ribbons. TEM observations of the as cast structures of the middle portion of these ribbons showed marked differences for some of the additions, mainly titanium and zirconium. The magnesium and silicon-containing ternary alloys were similar to the binary copper-chromium alloy and all the solutes were in solid solution for these cases, as would be expected since magnesium and silicon were in amounts inferior to their equilibrium solid solubilities in copper. Figure IV.23 shows the as cast microstructure of the silicon, titanium, and though the concentration of titanium was far less than its equilibrium solid solubility (approximately 1 ^{at}% at 500°C [21]) the titanium-containing ribbon had a fine distribution of titanium-rich particles, uniformly distributed within the grain interiors. Figures IV.23.b and c show bright and dark field TEM micrographs of the as cast microstructure of the titanium-containing alloy. The dark field image was taken using one of the titanium-rich particle diffracted beams. These fine particles,

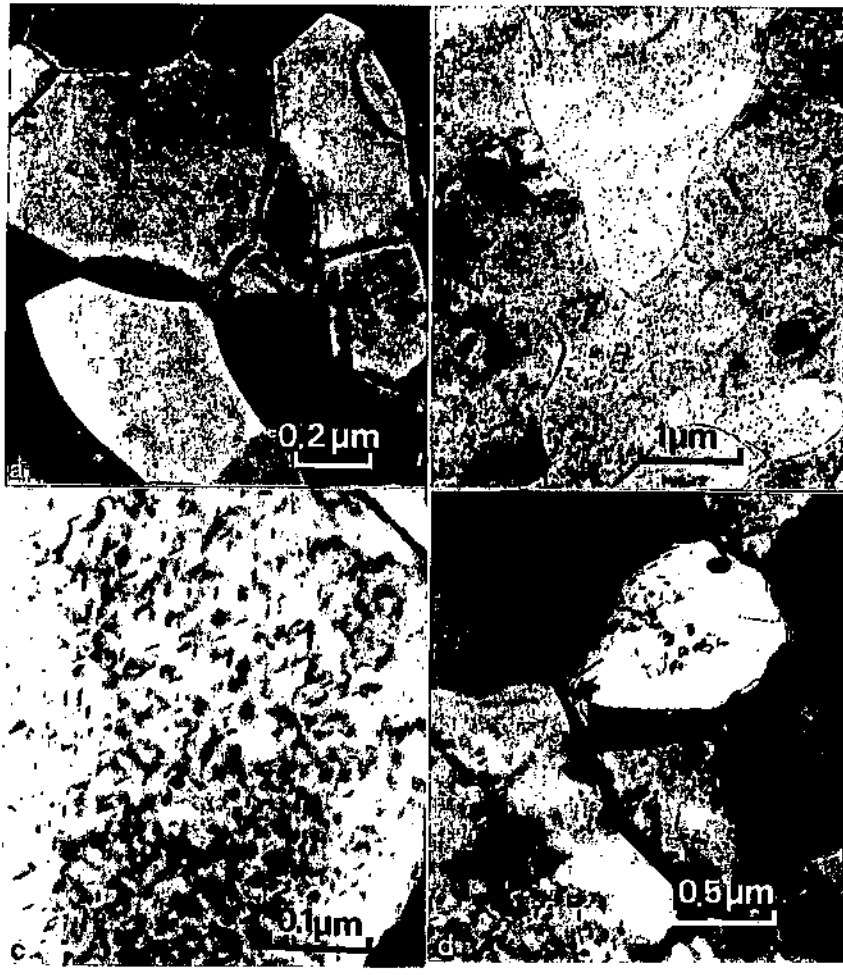

Figure IV.22 As cast and heat treated microstructure of the wheel and middle portions of Cu-Zr0.33 at% ribbon. The wheel side (a) was particle-free, while the middle portion (b) contained copper-zirconium intermetallic particles arranged in a cellular manner. After heat treatment (c, wheel side 30 min 500°C, d, middle 30 min 600°C) precipitation and/or growth of the zirconium-rich particles occurred.

5-10 nm in size, were extracted and their structure analyzed by electron diffraction. Their structure was identified as that of distorted tetragonal TiO_2.

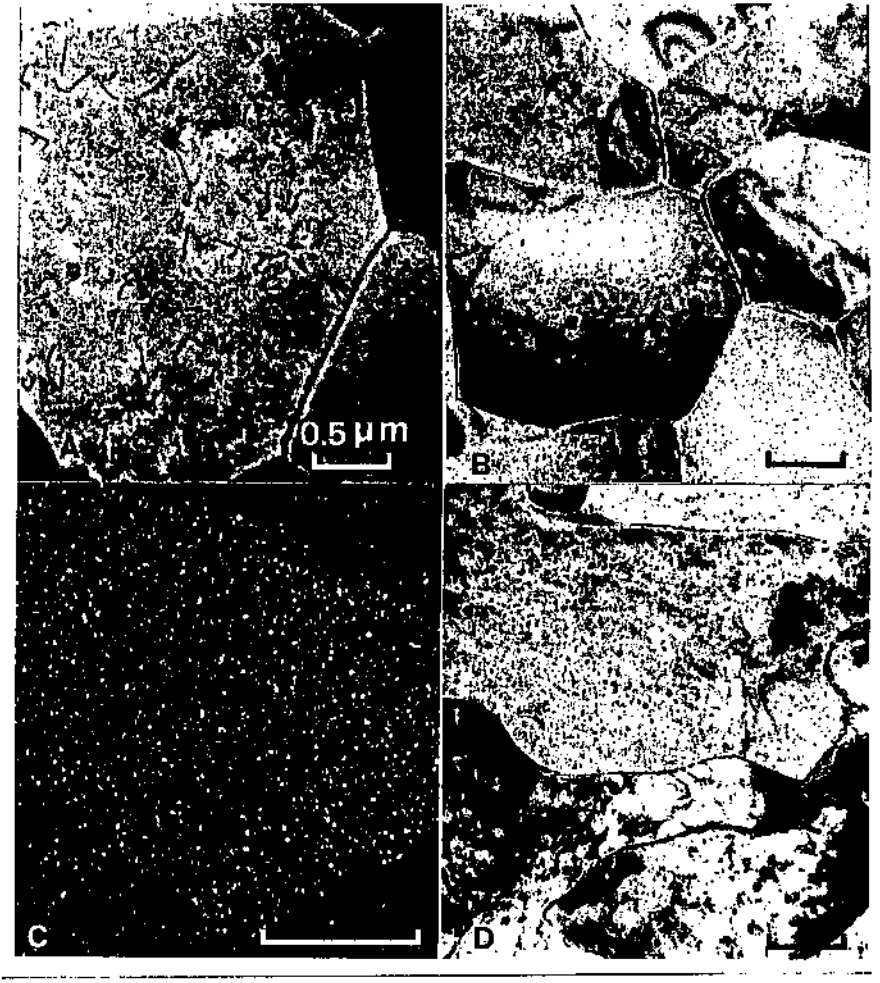

Figure IV.23 As cast microstructure of the middle portion of silicon (a), titanium (b and c) and zirconium (d) containing copper-chromium ribbons cast at 26 ms^{-1}. The titanium-containing ribbon had TiO_2 particles uniformly distributed within the matrix. Figure (c) is a centered dark field image using one of the particle reflections.

The distortion of the tetragonal crystal structure might have been caused by either copper or chromium substitution in the TiO_2 crystal. The analysis of the diffraction patterns is given in paragraph 4.3.3.1.

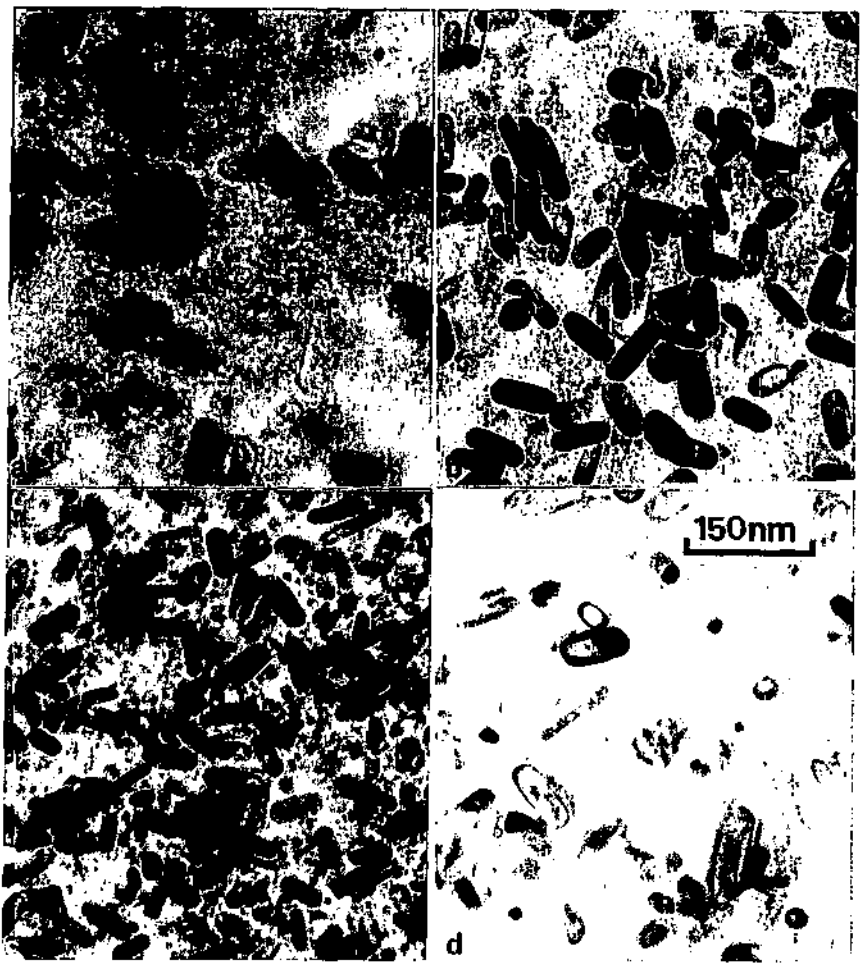

Figure IV.24 Microstructural changes of Cu-Cr1.85 at% ribbon spun at 8 ms^{-1} annealed at 500°C. The as cast ribbon (a) contained chromium-rich particles uniformly distributed within the grains, leaving small particle-free zones around the grain boundaries. After a heat treatment of 30 min a uniform precipitation of chromium particles was observed (b). Both particle distributions coarsened with further heat treatment (c-24h) and eventually the small particles disappeared after 96 h (d).

Upon annealing, precipitation of the excess chromium solute occurred in all the chromium-containing ribbons. For the alloys spun at speeds less than 16 ms^{-1}, where an initial distribution of chromium particles was present, a

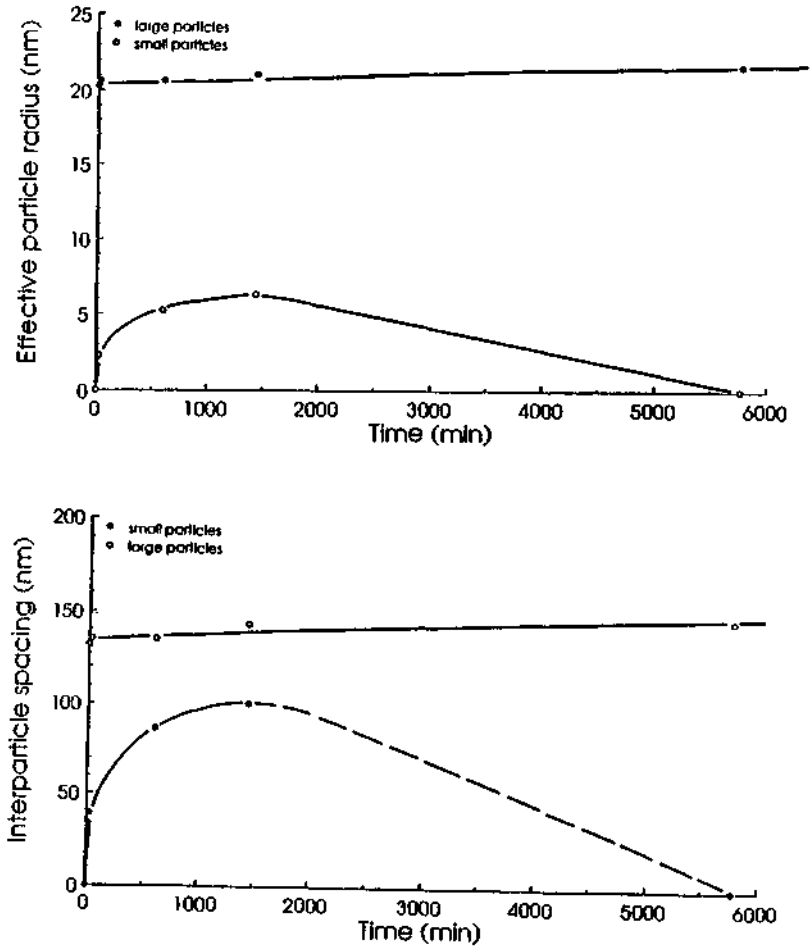

Figure IV.25 Evolution at 500°C of the effective radius of coarsening and volume interparticle spacing of both the small and large chromium particles in the Cu-Cr1.85 at% ribbon spun at 8 ms^{-1}.

bimodal distribution of particles resulted. Figure IV.24 shows the evolution of the microstructure upon isothermal annealing at 500°C of the alloy spun at 8 ms^{-1}. A fine and uniform distribution of particles initially precipitated from the chromium in solid solution. On further annealing coarsening of the microstructure caused a rise in the size and spacing of both the fine precipitated, and coarse previously existing particles. Because of their size, the coarsening of the large chromium particles was minimal at 500°C as shown by the virtually flat evolution

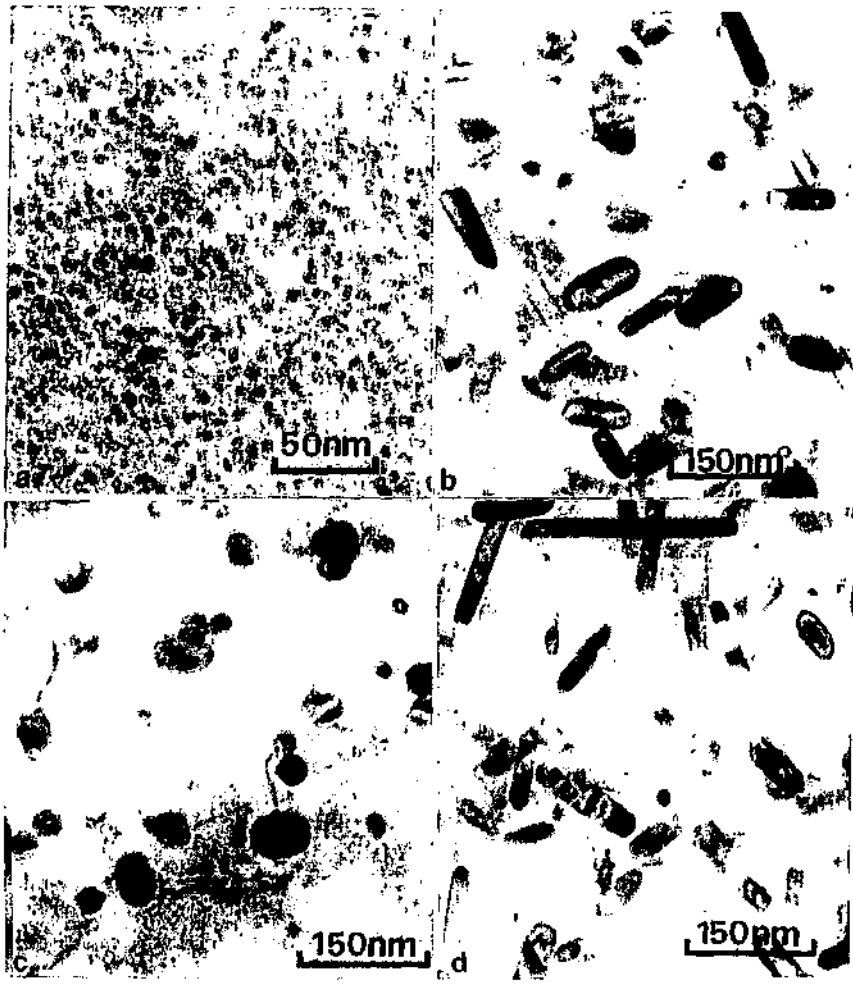

Figure IV.26 Microstructure of annealed copper-chromium and copper-chromium-metal ribbons showing different chromium morphologies. All chromium-containing ribbons after peak aging (500°C, 30 min) (a) had small and near spherical particles. After 48 h at 600°C the chromium particles in the binary Cu Cr 1.85^{at}% ribbon (b) adopted their cigar shaped morphology. The zirconium (c) and titanium (d) additions had strong effects on the projected aspect ratio of the particles, heat treatments were the same as (b).

(figure IV.25). For a fixed volume fraction, the distance over which each particle may influence its neighbour would be related to its size and its nearest neighbour distance *cf.* section 5.3.2, p. 138. As the spacing of the small particles increased as

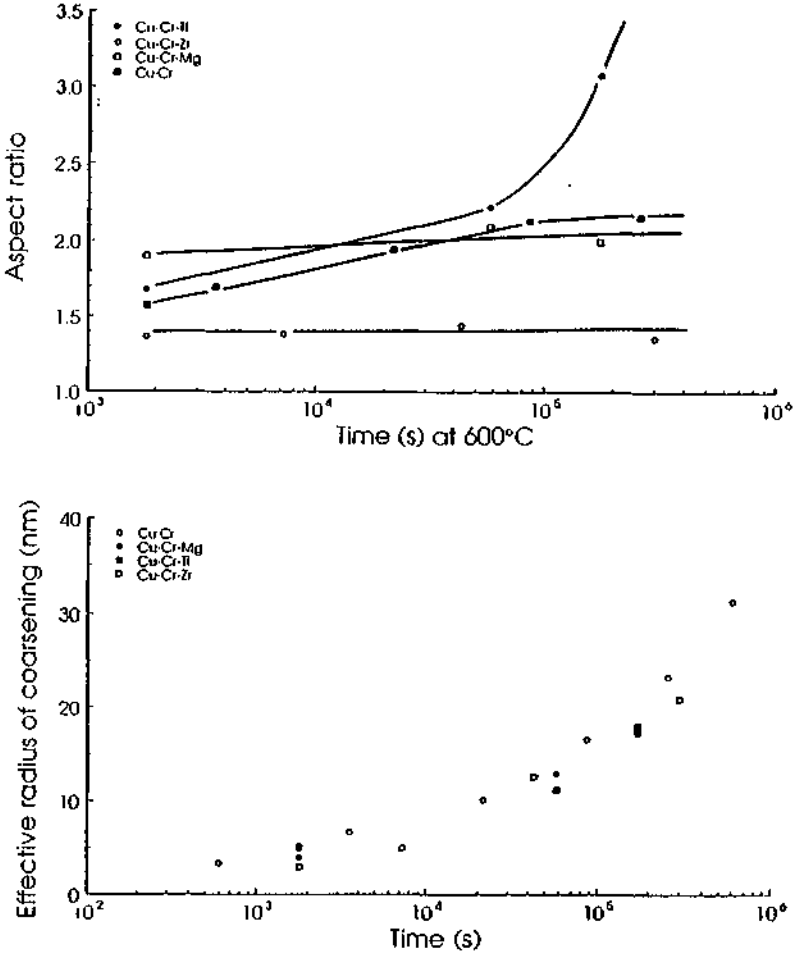

Figure IV.27 Evolution of size and projected aspect ratio of chromium particles with heat treatment. The effect of titanium and zirconium on the aspect ratio can clearly be seen in (a). The increase in the effective radius of coarsening, r_{eff}, at 600°C for the chromium particles was found to be similar for the titanium, magnesium and zirconium-containing ribbons (b).

a result of coarsening, the coarsening process changes from being controlled by the competition between the small, to a competition between the small and the large particles. This change occurs when the sphere of influence of the small particles overlaps with that of the larger particles. As a result the small particles disappear.

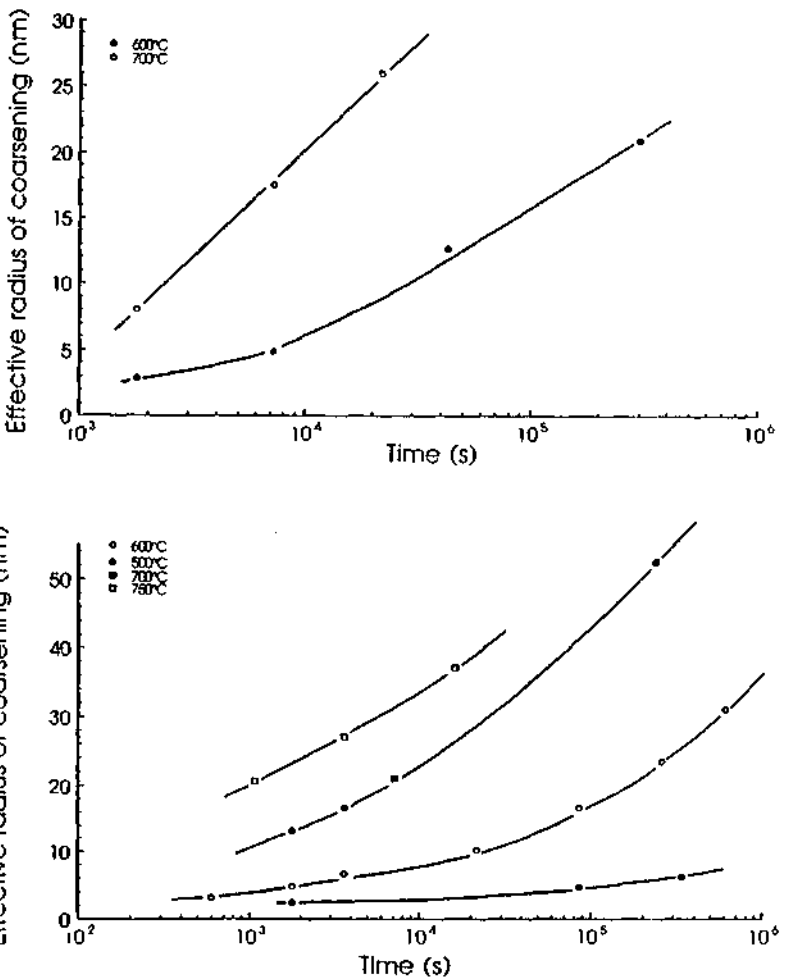

Figure IV.27 (Continued) Coarsening of the chromium particles at different temperatures is illustrated in figure (c) and (d) for the Cu-Cr2.22 at% Zr0.18 at% and the Cu-Cr1.85 at% ribbons respectively, spun at 26 ms^{-1}.

The evolution of size and volume interparticle spacing of small and the large chromium particles in the bimodal distribution is shown in figure IV.25. The spacing was directly calculated from TEM micrographs by counting the number of particles in a given volume, after estimating the foil thickness.

Annealing the binary alloys spun at speeds above 16 ms^{-1} where the chromium solute was in solid solution resulted in copious precipitation. No marked difference in the size or the distribution of particles was observed at the end of precipitation (determined by peak aging: 30 min at 500°C). This suggested that the rate of precipitation for the different binary ribbons spun at 43, 36, 26 and 16 ms^{-1} was more or less identical. The quench rate had therefore little effect on the rate of precipitation of the excess chromium in solid solution. When heat treated to peak strength all the alloys examined had similar near-spherical precipitate morphologies as illustrated in figure IV.26.a for the binary alloy spun at 26 ms^{-1}. Further annealing caused gradual coarsening of the microstructure, the chromium particles adopted their typical cigar shaped morphology, previously observed by several authors [125, 126]. Figure IV.26.b,c and d show the precipitate size and morphology after a heat treatment of 48 h at 600°C. The cigar shaped morphology of the chromium particles is clearly seen for the binary alloy as well as the zirconium and titanium-containing ribbons. Similar morphologies to those of the binary alloy were observed in magnesium and silicon-containing ribbons. However, noticeable differences in projected aspect ratio of the chromium particles were noted between the zirconium (figure IV.26.c) and the titanium-containing (figure IV.26.d) ribbons. Zirconium addition tended to decrease the projected aspect ratio of the chromium particles bringing it close to unity, while titanium addition enhanced the longitudinal growth of these particles increasing the average projected aspect ratio to above 3 after prolonged heat treatment. Magnesium and silicon additions did not appreciably influence the shape. Their influence on the evolution of the projected aspect ratio on annealing at 600°C was similar to that of the binary ribbon. Figure IV.27 summarizes the size and projected aspect ratio of the chromium particles in the various ribbons after heat treatment. The zirconium-rich phase found in the as cast zirconium-containing ribbons was found to coarsen; a large percentage of these particles was then found at the grain boundaries. Figures IV.27.b,c and d show the variation of the effective radius of coarsening, r_{eff}, of the chromium particles with time at different temperatures, and with different alloying additions. Ribbons with additions of zirconium, titanium or magnesium have similar growth behaviour at 600°C as shown in figure IV.27.b. Figure IV.27.c shows the growth of the chromium particles in the temary copper-chromium-zirconium ribbon at 600 and 700°C. The coarsening of the chromium particles in the Cu Cr1.85 at% ribbon spun at 26 ms^{-1} at 500, 600, 700 and 750°C is illustrated in figure IV.27.d. As can be seen by comparing figures IV.27.c and d, the growth rate of the chromium particles was unaffected by the presence of a second solute.

Figure IV.28 TEM microstructure of copper 0.7 at% yttrium ribbons melt spun at 43 ms^{-1}. As cast state (a), and after annealing for 1 h at 700°C (b).

The microstructures of the as cast and heat treated Cu-Y0.7 at% ribbons spun at 43 ms^{-1} are shown in figure IV.28. The middle, columnar portion of the as cast ribbon consisted of grains 0.5 µm in size. Nearly spherical yttrium-rich particles, approximately 23 nm in size, were found uniformly distributed within the grains and along the grain boundaries. The dislocation density in the as cast state was estimated as $8x10^{14}$ m^{-2}. In comparison with the binary copper-chromium alloy spun at 26 ms^{-1} this density was higher. The presence of particles pinning dislocations in the yttrium-containing ribbon as well as the faster casting speed could explain the difference observed. In the case of the binary chromium ribbon, no particles were present to pin the dislocations formed due to thermal stresses during solidification as well as those formed during the impact of the ribbon with the chamber wall during melt spinning, giving the possibility of the dislocations to annihilate. The lack of supplementary precipitation in the copper-yttrium ribbon during annealing confirmed that no significant solution extension occurred; this is consistent with the absence of age hardening as seen by microhardness and tensile testing, suggesting that the solubility of the yttrium was not extended above its maximum equilibrium value of less than 0.04 at% [23]. With heat treatment the microstructure coarsened. The grain boundary particles present in the as cast material quickly coalesced. The rapid coarsening of these particles liberated the copper grains from their pinning obstacles, resulting in rapid grain growth. After 1h at 700°C the grain size increased to 1.5 µm. No yttrium-rich particles were found

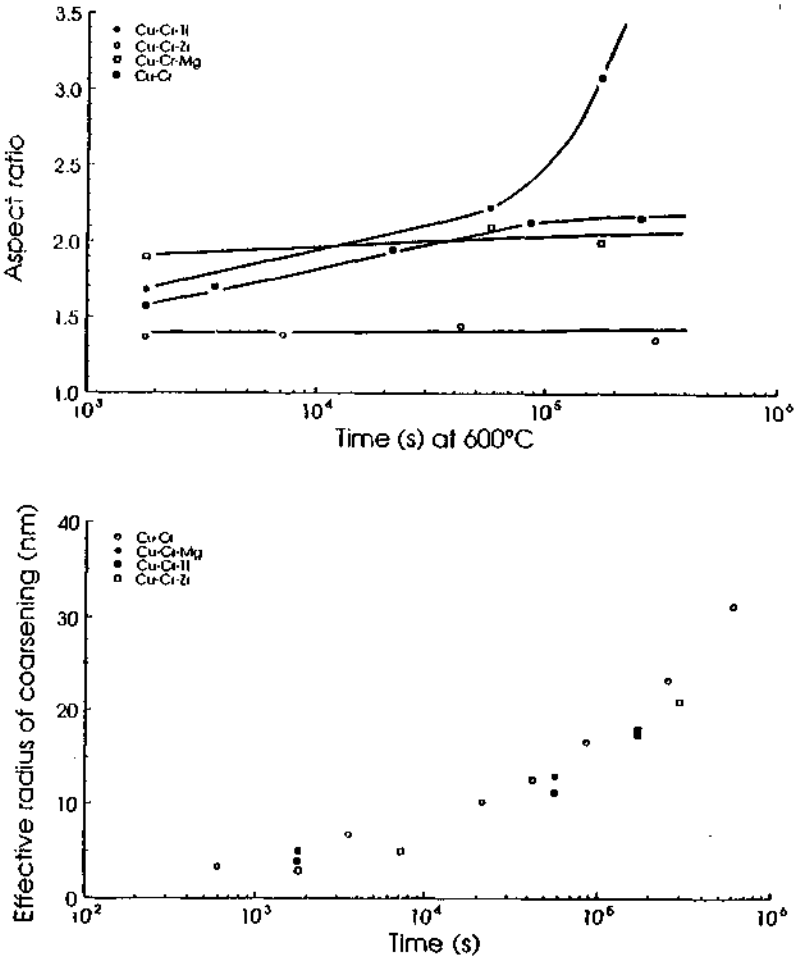

Figure IV.27 Evolution of size and projected aspect ratio of chromium particles with heat treatment. The effect of titanium and zirconium on the aspect ratio can clearly be seen in (a). The increase in the effective radius of coarsening, r_{eff}, at 600°C for the chromium particles was found to be similar for the titanium, magnesium and zirconium-containing ribbons (b).

a result of coarsening, the coarsening process changes from being controlled by the competition between the small, to a competition between the small and the large particles. This change occurs when the sphere of influence of the small particles overlaps with that of the larger particles. As a result the small particles disappear.

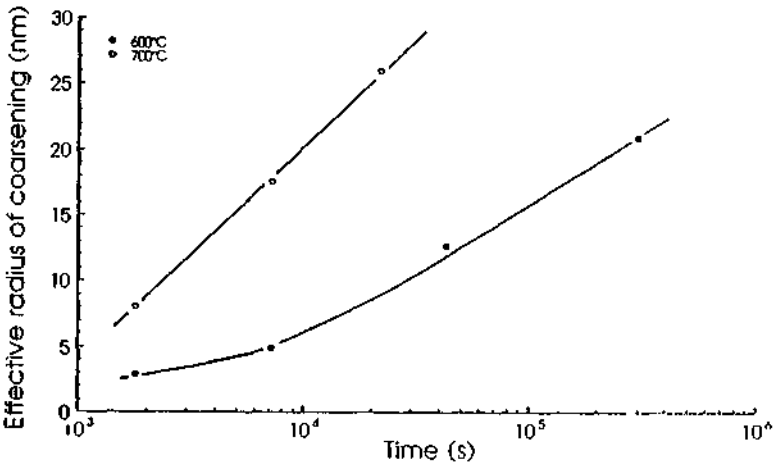

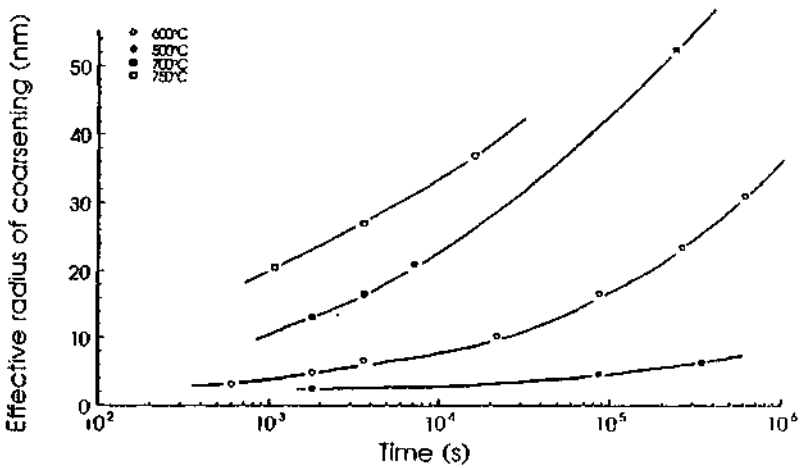

Figure IV.27 (Continued) Coarsening of the chromium particles at different temperatures is illustrated in figure (c) and (d) for the Cu-Cr2.22 at% Zr0.18 at% and the Cu-Cr1.85 at% ribbons respectively, spun at 26 ms^{-1}.

The evolution of size and volume interparticle spacing of small and the large chromium particles in the bimodal distribution is shown in figure IV.25. The spacing was directly calculated from TEM micrographs by counting the number of particles in a given volume, after estimating the foil thickness.

Annealing the binary alloys spun at speeds above 16 ms^{-1} where the chromium solute was in solid solution resulted in copious precipitation. No marked difference in the size or the distribution of particles was observed at the end of precipitation (determined by peak aging: 30 min at 500°C). This suggested that the rate of precipitation for the different binary ribbons spun at 43, 36, 26 and 16 ms^{-1} was more or less identical. The quench rate had therefore little effect on the rate of precipitation of the excess chromium in solid solution. When heat treated to peak strength all the alloys examined had similar near-spherical precipitate morphologies as illustrated in figure IV.26.a for the binary alloy spun at 26 ms^{-1}. Further annealing caused gradual coarsening of the microstructure, the chromium particles adopted their typical cigar shaped morphology, previously observed by several authors [125, 126]. Figure IV.26.b,c and d show the precipitate size and morphology after a heat treatment of 48 h at 600°C. The cigar shaped morphology of the chromium particles is clearly seen for the binary alloy as well as the zirconium and titanium-containing ribbons. Similar morphologies to those of the binary alloy were observed in magnesium and silicon-containing ribbons. However, noticeable differences in projected aspect ratio of the chromium particles were noted between the zirconium (figure IV.26.c) and the titanium-containing (figure IV.26.d) ribbons. Zirconium addition tended to decrease the projected aspect ratio of the chromium particles bringing it close to unity, while titanium addition enhanced the longitudinal growth of these particles increasing the average projected aspect ratio to above 3 after prolonged heat treatment. Magnesium and silicon additions did not appreciably influence the shape. Their influence on the evolution of the projected aspect ratio on annealing at 600°C was similar to that of the binary ribbon. Figure IV.27 summarizes the size and projected aspect ratio of the chromium particles in the various ribbons after heat treatment. The zirconium-rich phase found in the as cast zirconium-containing ribbons was found to coarsen; a large percentage of these particles was then found at the grain boundaries. Figures IV.27.b,c and d show the variation of the effective radius of coarsening, r_{eff}, of the chromium particles with time at different temperatures, and with different alloying additions. Ribbons with additions of zirconium, titanium or magnesium have similar growth behaviour at 600°C as shown in figure IV.27.b. Figure IV.27.c shows the growth of the chromium particles in the ternary copper-chromium-zirconium ribbon at 600 and 700°C. The coarsening of the chromium particles in the Cu Cr1.85 at% ribbon spun at 26 ms^{-1} at 500, 600, 700 and 750°C is illustrated in figure IV.27.d. As can be seen by comparing figures IV.27.c and d, the growth rate of the chromium particles was unaffected by the presence of a second solute.

Figure IV.28 TEM microstructure of copper 0.7 at% yttrium ribbons melt spun at 43 ms^{-1}. As cast state (a), and after annealing for 1 h at 700°C (b).

The microstructures of the as cast and heat treated Cu-Y0.7 at% ribbons spun at 43 ms^{-1} are shown in figure IV.28. The middle, columnar portion of the as cast ribbon consisted of grains 0.5 μm in size. Nearly spherical yttrium-rich particles, approximately 23 nm in size, were found uniformly distributed within the grains and along the grain boundaries. The dislocation density in the as cast state was estimated as $8x10^{14}$ m^{-2}. In comparison with the binary copper-chromium alloy spun at 26 ms^{-1} this density was higher. The presence of particles pinning dislocations in the yttrium-containing ribbon as well as the faster casting speed could explain the difference observed. In the case of the binary chromium ribbon, no particles were present to pin the dislocations formed due to thermal stresses during solidification as well as those formed during the impact of the ribbon with the chamber wall during melt spinning, giving the possibility of the dislocations to annihilate. The lack of supplementary precipitation in the copper-yttrium ribbon during annealing confirmed that no significant solution extension occurred; this is consistent with the absence of age hardening as seen by microhardness and tensile testing, suggesting that the solubility of the yttrium was not extended above its maximum equilibrium value of less than 0.04 at% [23]. With heat treatment the microstructure coarsened. The grain boundary particles present in the as cast material quickly coalesced. The rapid coarsening of these particles liberated the copper grains from their pinning obstacles, resulting in rapid grain growth. After 1h at 700°C the grain size increased to 1.5 μm. No yttrium-rich particles were found

along the grain boundaries, only large copper-yttrium intermetallic grains formed resulting in a duplex microstructure. These grains could be seen as etched out portions in the thin foil since, as described in paragraph 3.6.1, electrolytic thinning conditions that could simultaneously electropolish the copper matrix as well as the yttrium-rich phase were not found. Smaller yttrium-rich particles were found in the middle of the copper grains. These particles coarsened at a rate similar to that observed for the chromium particles in the binary and ternary chromium-containing ribbons. Figure IV.29 illustrates their growth at different temperatures.

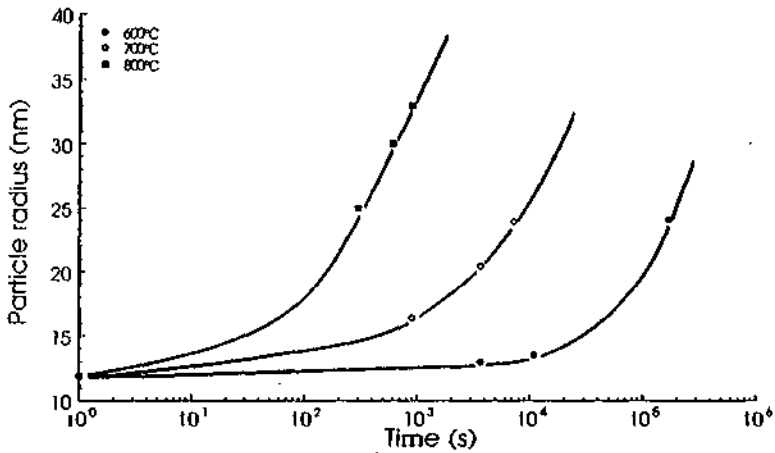

Figure IV.29 Evolution of the size of yttrium-rich particles at different temperatures.

4.3.2 Boron-containing alloys.

The TEM microstructures of the centre of the copper-boron and copper-yttrium-boron ribbons before and after heat treatment are shown in figure IV.30. The as cast structure consisted of grains 1 µm in size for the Cu-B2.7 at% alloy and 0.4 µm for the concentrated Cu-B7.3 at% ribbon. Boron-rich particles, 25 nm in size, decorated the grain and solidification cell boundaries. The cell size was 0.3 and 0.2 µm for the two alloys respectively. There was no evidence of boron precipitation within the cell interiors, neither in the as cast state, nor after annealing. It can therefore be considered that the solubility of boron throughout the ribbon thickness (with the exception of a narrow wheel contact zone) was hardly extended above its equilibrium value (figure IV.30.a).

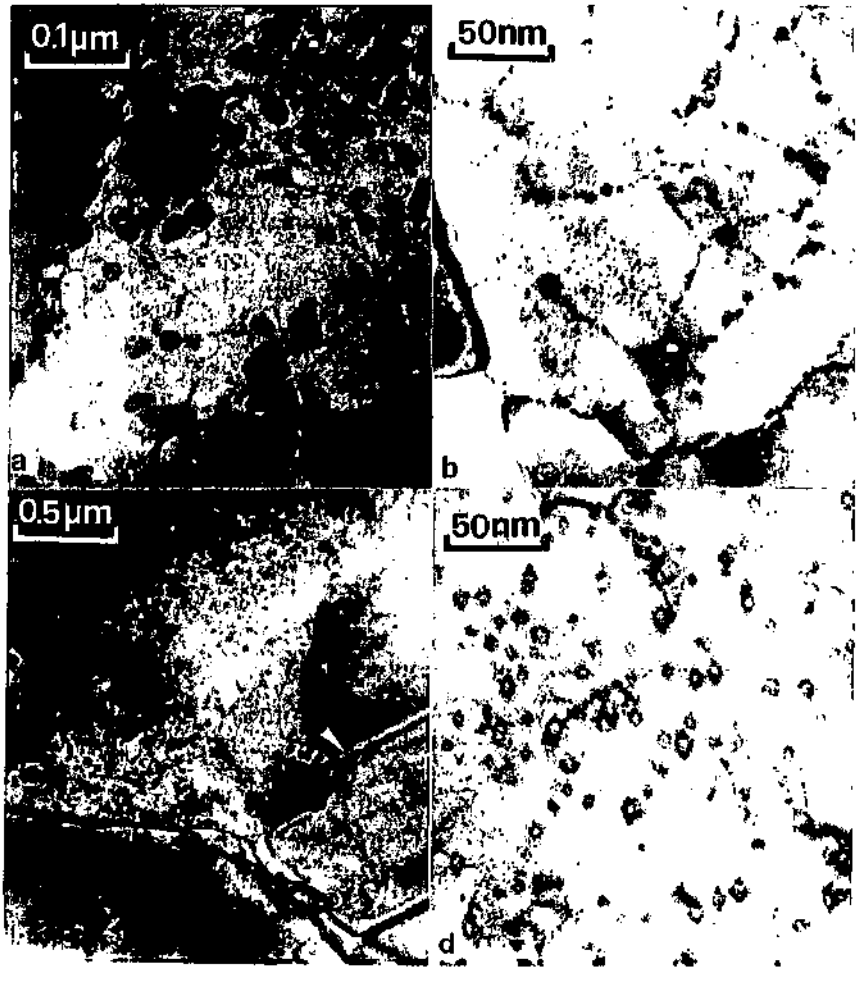

Figure IV.30 TEM micrographs of the centre of the as cast and heat treated binary and ternary ribbons. (a) As cast Cu-B7.3 at% ribbon showing amorphous boron-rich particles in a solidification cell structure. (b) As cast Cu-Y0.18 at% B2.3 at% ribbon, the structure consisted of amorphous boron and yttrium-rich particles. Heat treated for 30 min at 800°C (c) the binary alloy consisted of large crystalline boron grains (arrow) surrounded by boron-free copper grains. After 168 h at 850°C (d) the YB_6 particles in the ternary alloy coarsened slowly.

During tilt experiments on the small boron particles decorating the solidification cell walls, the particles never changed contrast as expected for a noncrystalline phase. Microdiffraction analyses on these small particles (figure IV.31) confirmed

the amorphous nature of these particles; the amorphous rings are weak due to the small scattering factor of boron.

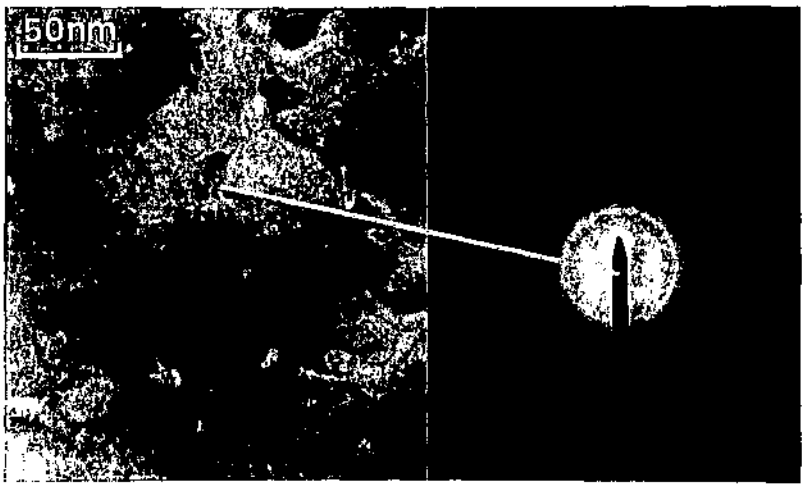

Figure IV.31 As cast Cu-B7.3 at% ribbon. Microdiffraction on the small amorphous boron particles. Electron beam diameter is 30 nm.

Thin foils of the wheel contact area of the binary ribbons showed different microstructures. Figure IV.32 shows the as cast microstructure of the wheel side of both the Cu-B2.7 at% and Cu-B7.3 at% ribbons spun at 43 ms^{-1}. The less concentrated alloy consisted of grains 0.5 µm in size with no boron segregation or large particles, only a uniform fine coherent precipitation, suggesting that the solubility of boron had been extended to about alloy composition. The wheel contact side of the concentrated Cu B7.3 at% ribbon ("structureless" when observed optically) consisted of microcrystals 50 nm in size with some amorphous boron particles at triple points. The extent of solid solution extension within this region was difficult to estimate.

TEM observations of the middle of the boron-rich ribbons showed no measurable change in microstructure on annealing to time temperature treatments equivalent to 700°C for 30 min. This invariance of microstructure confirmed the mechanical testing and optical observations described earlier, where similarly no change occurred. Further annealing at higher temperatures or for longer times provoked the onset of the microstructural instability described earlier. Large boron crystals surrounded by copper grains depleted of their small amorphous boron-rich particles were observed. The dissolution of the amorphous phase at the expense of the crystalline phase removed the pinning obstacles to grain boundary motion, which resulted in copper grain growth in the neighbourhood of the crystalline boron

phase (figure IV.5). At a sufficient distance from the boron crystal, the amorphous particles were still found and no growth was observed. The crystalline nature of the large boron phase was confirmed by tilt experiments where diffraction analysis allowed identification of the crystal structure as ß-rhombohedral boron. Details of the analysis are given in paragraph 4.3.3.2.

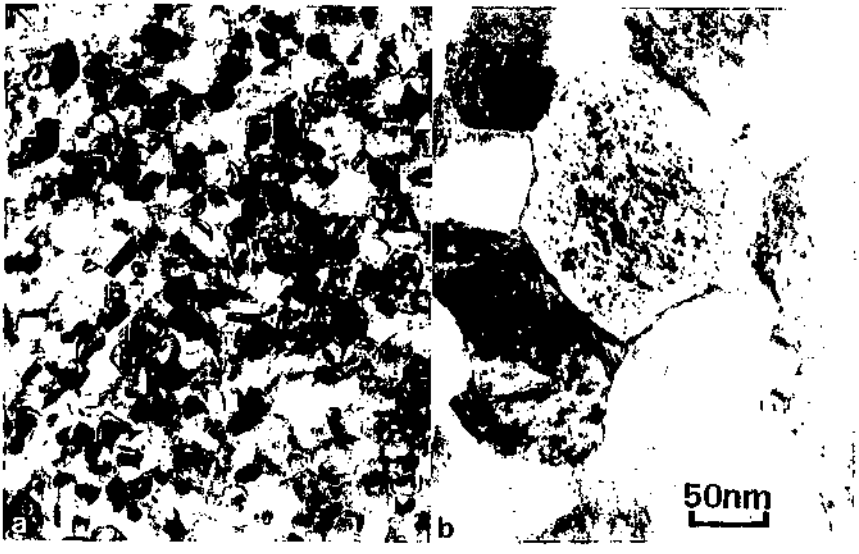

Figure IV.32 TEM micrographs of the wheel contact area of both the Cu B7.3 at% (a) and Cu-B2.7 at% (b) ribbons melt spun at 42 ms^{-1}.

Analysis of the transformation of amorphous to crystalline boron was carried out on two alloys, initially qualitatively on the Cu-82.7 at% and Cu-B7.3 at% ribbons spun at 42 ms^{-1} and subsequently quantitatively on the Cu-Y0.23 at% B5.66 at% ribbon spun at 36 ms^{-1}. As shown in table IV.2 and described in section 4.1.2, page 48, the number density of crystalline particles in the Cu-Y0.23 at% B5.66 at% ribbon was far less than in the binary ribbons. As a result, the time required to reach total transformation of the amorphous particles was longer (figure IV.8). For experimental convenience, the quantification of the transformation of the amorphous to crystalline boron was carried out on the ternary yttrium-containing, boron-rich ribbon. Table IV.2 shows the evolution in size of both the amorphous and crystalline particles in the binary and ternary ribbons. Before the onset of the microstructural instability (*i.e.* the appearance of the first boron crystals) it is clearly shown that for the binary alloys the amorphous particles do not coarsen in any appreciable manner. Because of their invariance in size, as observed in the binary alloy, the average size of the amorphous particles were not measured in the ternary ribbon during this transient period. Growth of the crystalline boron particles near the

wheel contact side decreased slowly the volume fraction of amorphous particles as boron was transferred from one phase to the other. As the volume fraction of crystalline boron increased, the average size of the amorphous particles can be seen to decrease. This is explained by the decreasing proportion of amorphous particles, which are uninfluenced by the presence of the crystalline phase as the size of the latter increases with time, and an increasing proportion of the measured population of particles being particles that are dissolving.

Table IV.2 Number and size of amorphous and crystalline boron particles showing the influence of annealing treatments

		amorphous			crystalline		
Alloy	State	volume fraction f_v(%)	Part. size (nm)	Part. density (x10^{21}) (m^{-3})	volume fraction f_v(%)	Part. size (µm)	Part. density (x10^{12}) (m^{-3})
Cu-B7.3at%	as cast	3.6	26±4	3.9	0	0	0
	600°C 3h	2.6	22±5	3.9	0	0	0
	6h	3.6	26±4	4.0	0	0	0
	23h	1.2	18±4	4.4	1	6.5	280
	60h	0.7	16±4	3.0	2	9.0	260
	700°C 5min	2.9	24±5	4.1	0	0	0
	10min	3.1	26±4	3.8	0	0	0
	15min	2.3	21±5	4.5	0	0	0
	20min	2.1	24±4	3.5	0	0	0
	40min	2.0	22±4	3.4	1	3.6	900
Cu-B2.7at%	As cast	1.4	26±4	1.5	0	0	0
	600°C 6h	1.2	26±4	1.3	0	0	0
Cu-Y0.23at% B5.66at%	750°C 30min				0.16	7.6	46
	6h				0.97	20.1	34
	87h				2.4	31.9	33
	800°C 20min				0.25	10.5	56
	1h				1.02	16.8	59
	24h				2.6	21.7	56

Yttrium-containing copper-boron ribbons showed a solidification cell structure finer (60-80 nm) than the binary ribbons, with a grain size of approximately 1 µm for the Cu-Y0.18 at% B2.3 at% ribbon (figure IV.30.c) and of 0.5 µm for the Cu-Y0.23 at% B5.66 at% ribbon. Boron and yttrium-rich particles 15 nm in size were found decorating the solidification cell walls and grain boundaries. The boron-rich particles within the boundaries were identified as the amorphous phase as found in the binary ribbons. Within the cells, fine precipitation of a yttrium-rich

phase in the as cast state of either copper-yttrium intermetallic or a yttrium boride phase was also found. The crystallographic analysis of these particles was difficult because of their small size (2 nm). Based on the distribution and size, precipitation of these yttrium-rich particles was believed to have taken place after solidification, during the secondary cooling of the ribbon.

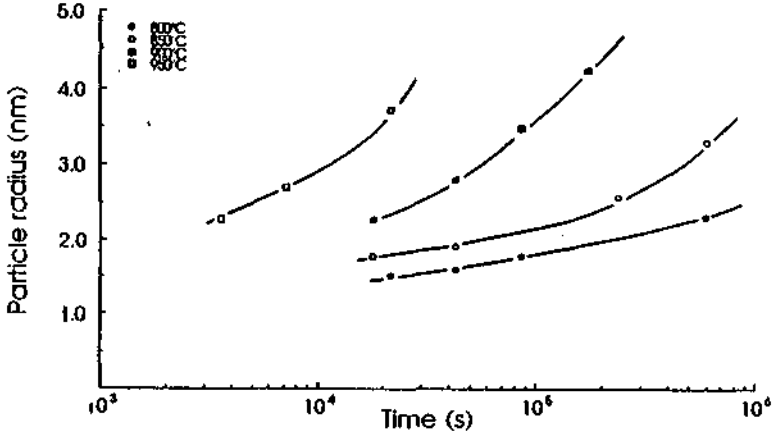

Figure IV.33 Coarsening of YB_6 particles in Cu Y0.18 at% B2.3 at% spun at 26 ms^{-1}.

After heat treatment the microstructure of the copper-yttrium-boron ribbons coarsened slowly. The yttrium-rich particles present after annealing were crystallographically analyzed as cubic YB_6; the analysis of this phase is given in paragraph 4.3.3.3. Only crystalline YB_6 and ß-rhombohedral boron particles were identified in annealed samples. Accounting for the total boron content distributed between the boride particles and the free boron, volume fraction measurements of each phase taking a molar volume of boron as 4.6×10^{-6} m^3mol^{-1} and YB_6 as 4.14×10^{-5} m^3mol^{-1} [127], the stoichiometry of the boride as YB_6 was confirmed. The precise nature of the yttrium intracellular precipitation present before annealing remains uncertain and may have been YB_6 or a copper-yttrium intermetallic. No amorphous boron particles were observed after prolonged heat treatment suggesting that the amorphous particles were perhaps resorbed by crystalline boron, as in the case of the binary alloys. Alternatively, they were possibly consumed by the formation of supplementary YB_6 particles after reaction with the initially precipitated yttrium-rich phase, if these precipitated particles were copper-yttrium intermetallics.

Contrary to the binary alloys no grain growth occurred during annealing in the areas depleted of amorphous boron, due to stable YB_6 particles which pinned the grain boundaries. After the initial transformations (amorphous to crystalline boron and transformation of the precipitated yttrium-rich phase to YB_6), a stable volume fraction of YB_6 particles, approximately 1 ^{vol}% and 1.5^{vol}% for the Cu Y0.18 ^{at}% B2.3 ^{at}% and the Cu-Y0.23 ^{at}% B5.66 ^{at}% ribbons was measured. Coarsening of crystalline boron particles in the ternary ribbons followed the same rate as in the binary. Figure IV.33 illustrates the evolution of the average size of YB_6 particles after different isothermal anneals. The coarsening rate of the YB_6 particles was extremely slow.

4.3.3 Electron diffraction analysis

4.3.3.1 Titanium dioxide

No stable ternary Cu-Cr-Ti compound has been reported and therefore only binary chromium-titanium or copper-titanium compounds were considered as possible phases. Due to possible oxygen contamination, stable oxides of titanium or chromium may form. However, since no chromium oxide was detected in the binary copper-chromium ribbons, it is improbable that this oxide should form in this ternary alloy.

Copper-rich titanium intermetallic phases likely to form are either Cu_4Ti or Cu_3Ti. Three polymorphs of Cr_2Ti have also been identified. These phases are the only intermetallics known to exist in the binary chromium-titanium or copper-titanium systems [21]. If oxygen contamination was considered, the stable oxide possible in the ternary copper-chromium-titanium system would be TiO_2. Several polymorphs of TiO_2 have been reported, the two stable structures being tetragonal rutile (high temperature) and anatase (low temperature) [128]. All other oxides of titanium either decompose at elevated temperature or have an energy of formation inferior to TiO_2 and are therefore less probable to form.

Figure IV.34 shows the selected area diffraction patterns obtained from small titanium-rich particles extracted onto a replica from the as cast Cu-Cr2.22 ^{at}%Ti0.11 ^{at}% ribbon. The angles between the different zone axes obtained experimentally are shown. Due to the symmetry of the diffraction patterns, triclinic, monoclinic, hexagonal and rhombohedral structures can be directly eliminated. The 4-fold symmetry of zone (1) as well as the angular relationship between the different axes would suggest a near cubic structure. Tetragonal or orthorhombic structures, with their lattice parameters similar in size could also be possible. If the diffraction pattern (1) is indexed as [001] zone axis, zone (5) can be indexed as [011], with the (200) or the (100), depending on the indexing of zone (1), reflection missing. The cubic space group proposed is $I\bar{4}3d$. or the primitive $P2_13$, both incompatible with all possible phases.

Crystal structures based on a tetragonal or orthorhombic Bravais lattice, where the lattice parameters are near cubic can be considered instead. By rapid solidification one can envisage the substitution of atoms within the tetragonal structure causing a distortion such that the lattice parameters become similar. A space group that would be compatible with the observed diffraction patterns, as well as the extinctions observed, is the $P4_2/mnm$. TiO_2 (rutile) has this symmetry. Computer simulated diffraction patterns of the TiO_2 structure have shown a close resemblance between the simulated and the experimentally obtained patterns.

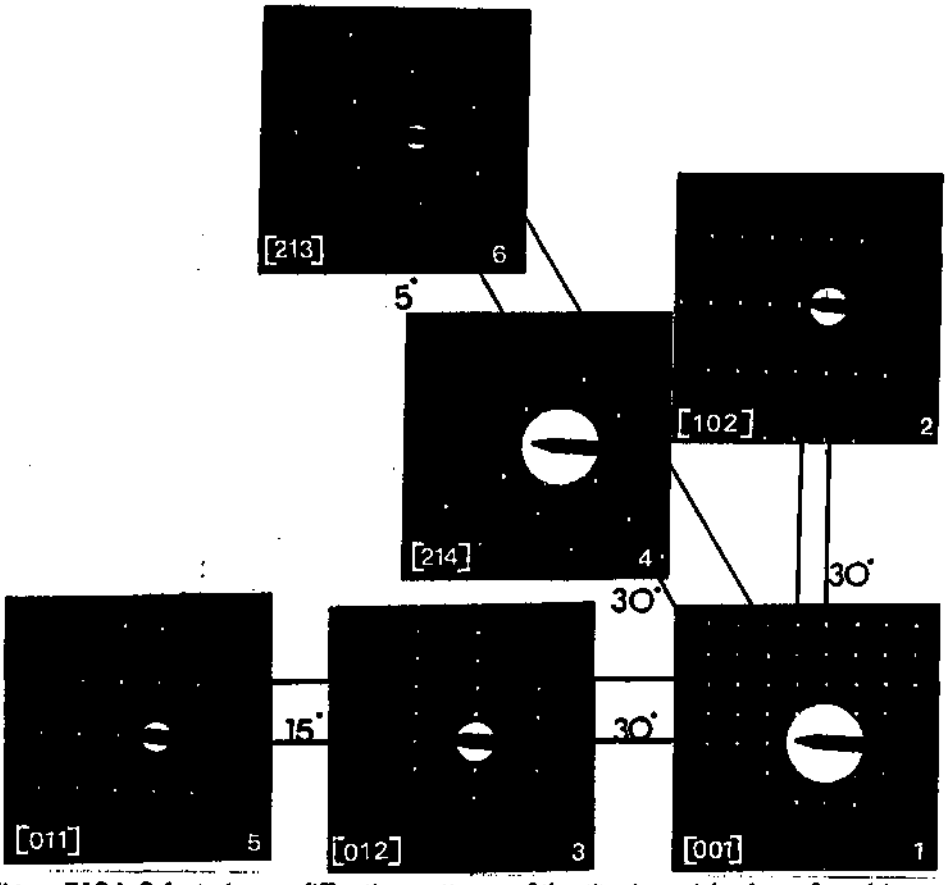

Figure IV.34 Selected area diffraction patterns of the titanium-rich phase found in an as cast Cu-Cr2.22 at%Ti0.11 at% ribbon (camera length: 770mm, 120kV).

If a slight variation in the lattice parameter of copper occurs, due to solid solution extension, the interplanar spacings of the two structures would be alike, for example $(111)_{Cu} \approx (211)_{TiO_2}$ and $(200)_{Cu} \approx (220)_{TiO_2}$. It is concluded that the

titanium-rich phase observed in the as cast Cu-Cr2.22 at%Ti0.11 at% ribbon was a distorted tetragonal titanium oxide. Distortion could be the result of substitution of copper or chromium in the structure.

4.3.3.2 Crystalline ß-rhombohedral boron

Figure IV.35 shows the selected area diffraction patterns as well as the tilt angles between the different zone axes obtained from one crystal. Eight different polymorphs of boron are known to exist [128]: three tetragonal, two rhombohedral, one orthorhombic, one hexagonal and one cubic. Two copper borides have also been identified [129-131]. Since their structure is identical to the ß-rhombohedral phase, they were considered as rhombohedral boron phases with some copper in solid solution as described by Higashi *et al.* [132] Comparison of the experimental diffraction patterns with the computer generated ones narrowed the choice of possible structures down to two phases: the tetragonal and ß-rhombohedral phases having $P4_1$ and, $R\bar{3}m$ space groups. Comparing the tilt angles between the zone axes of the two structures with the values obtained experimentally was a confirmation that the structure of the boron crystal was ß-rhombohedral boron.

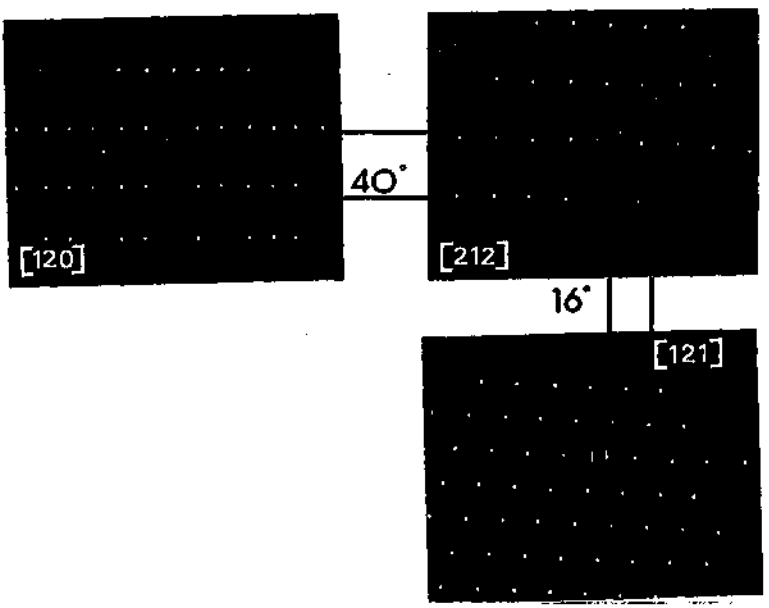

Figure IV.35 Selected area figures of diffraction of the crystalline boron phase obtained after annealing the rapidly solidified copper-boron ribbons (camera length: 1450mm, 100kV).

4.3.3.3 Yttrium hexaboride.

Figure IV.36 shows the different axes obtained as well as the angles between them. The symmetry observed and angles of 45 and 55° between zone (1) and zones (2) and (3) respectively suggest a cubic structure. Structures based on known copper-yttrium and yttrium-boron phases were tested for compatibility with the observed diffraction patterns. Cu_7Y, Cu_6Y and Cu_5Y [133-135]. have hexagonal structures and hence were not further considered. Due to the relatively high affinity of both boron and yttrium to oxygen, possible contamination of the alloy by oxygen and thereby forming an oxide was envisaged. It is quite unprobable that the oxide of boron, B_2O_3, would form since the oxide was not detected in binary copper-boron ribbons. The oxide of yttrium, Y_2O_3 having a cubic structure was however considered. Because of the very large difference in lattice parameter between the Y_2O_3 phase and the measured lattice parameters from the diffraction patterns, this oxide was eliminated.

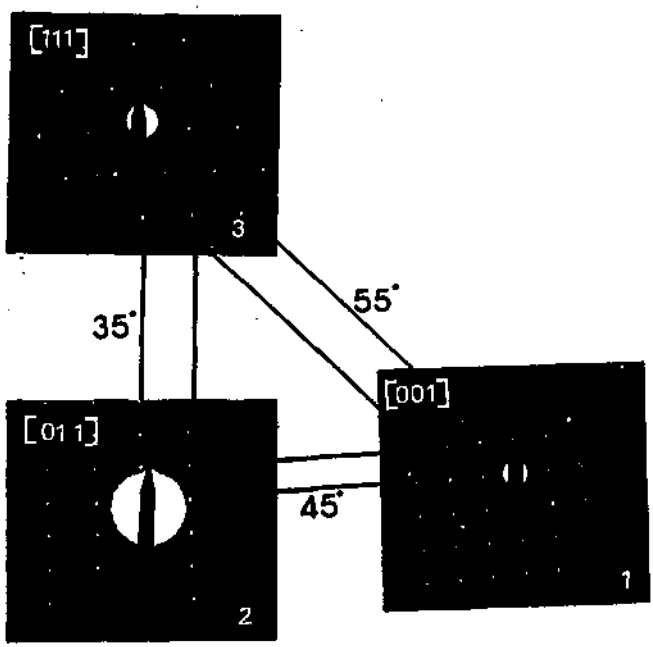

Figure IV.36 Selected area diffraction patterns obtained from the yttrium-rich phase after annealing (950°C, 6h) the rapidly solidified copper-yttrium-boron ribbon (camera length: 770mm, 120kV).

Taking the the crystal structure as cubic, the three zone axes could be directly indexed as: (1) [001], (2) $[0\bar{1}1]$ and (3) [111] with a lattice parameter of 0.405±0.05 nm. This corresponds within experimental error to the cubic hexaboride of yttrium.

CHAPTER 5

Discussion and Interpretation of Results

5 Discussion and interpretation of results

The previous chapter presented the thermal stability and mechanical property results of rapidly solidified copper alloys. The examination of these alloys and clarification of the mechanisms which determine thermal stability and strength were the main objectives of this study. Alloys were selected for study where minimal effects of solute additions on conductivity were expected. It was necessary to obtain a sufficient volume fraction of finely dispersed second phase particles, precipitated or preexisting, for efficient dispersion strengthening.

Anticipating an eventual industrial interest in hot consolidation of rapidly solidified material, the evolution of the microstructure with temperature was of particular concern. Two microstructural systems were studied: precipitation-strengthened and microsegregated, dispersoid-hardened alloys. In the former, alloying elements were selected for solid solution extension by rapid solidification. Care is needed on heating the rapidly solidified material, since the advantages of rapid solidification could be lost during high temperature treatments. It was observed that the maximum strength of precipitation-strengthened alloys was far higher than that of microsegregated dispersion-hardened alloys. However, the thermal stability of the microsegregated dispersoid-strengthened materials was in some cases greater, e.g. boron-rich copper-yttrium-boron ribbons. Such stability was of great interest since eventual consolidation would be easier. The nature of the strengthening phase, the casting conditions and the chemical composition were all of prime importance in controlling the stability and strength of the rapidly solidified materials.

The following sections discuss and interpret these results. The rapidly solidified microstructures obtained after melt spinning will be interpreted followed by an evaluation of the criteria of solubility extension. The effect of heat treatment on the mechanical properties as well as the reasons for the various microstructural changes and the observed thermal stabilities will be discussed in detail.

5.1 Interpretation of as cast microstructures and solute distribution

Based on conductivity, solubility and diffusivity criteria (independently from the rapidly solidified microstructure obtained) it was suggested in section 2.2 that solutes such as calcium, cerium, chromium, niobium, yttrium and zirconium would be interesting alloying additions to explore with respect to precipitation hardening. Ternary copper-metal-boron systems were also envisaged as microsegregated dispersion hardened alloys.

The dispersion of second phase particles may be the result of precipitation from a supersaturated solid matrix or microsegregation during the rapid solidification of the alloy. If sufficient supersaturation is obtained by rapid solidification, particles resulting from precipitation are more finely and more

uniformly distributed than the particles obtained from microsegregation. Solubility extension by means of rapid solidification was therefore preferred.

Section 5.1.1 deals with the mechanisms leading to the as cast microstructures obtained after melt spinning. In section 5.1.2 the solute distribution in these microstructures will be related to models to predict extension of solubility. The thermodynamic limitations of dispersoid formation of microsegregated dispersoid-hardened materials will be presented in section 5.1.3.

5.1.1 Interpretation of the microstructure of as cast ribbons

The microstructures observed at different points through the thickness of the ribbon are the result of competitive growth, the mode of solidification and of thermal and momentum transfer conditions established during melt spinning [109, 136, 137]. Changes in solidification rate are indicative of growth at different undercoolings which result in microstructure variations. These variations are provoked by recalescence which may not be totally suppressed during the melt spinning process.

Solidification initially took place by heterogeneous nucleation of the heavily undercooled melt on the wheel surface of the ribbon [138]. Depending on the wheel speed or undercooling, planar front growth, or cellular solidification of columnar grains followed. The transition from the fine equiaxed grains of the chill zone to columnar growth, if the solidification mode is unaltered, is the result of competitive crystal growth. Crystals with unfavorable growth orientation are overtaken by rapidly growing columnar grains having more favorable growth orientation. In this study this was confirmed by TEM observations. All the grains observed in thin foils taken from the centre of the ribbon thickness had their <100> directions parallel to the foil normal.

The inclination of the columnar grains observed in some ribbons can be explained by the dominance of either momentum [139] or thermal [140-142]] transfer mechanisms during ribbon formation. If momentum transfer conditions prevail, ribbon thickness is determined by the drag of the melt puddle provoked by the rotating wheel. Solidification is independent of ribbon thickness and occurs further downstream from the melt puddle. If ribbon formation is heat transfer controlled, solidification occurs within the melt puddle and the ribbon thickness is the result of growth of the solid within the puddle. In this case the inclination of the columnar grains back towards the melt puddle is due to the inclination of the crystal/melt interface during solidification. This in turn depends on the wheel surface velocity, u, and growth velocity, V, as shown in figure V.1 by Blank *et al.* [23]. Inclination of the grains towards the melt pool was observed in ribbons with small solidification intervals such as the copper-chromium alloys (figure IV.1). Under these conditions heat transfer dominates ribbon formation. If the alloy melt has a large solidification interval, viscosity gradients within the puddle are less steep and

solidification occurs to a greater extent outside the melt puddle, momentum transfer conditions dominate ribbon formation. In the latter case a slower solidification results allowing the melt to be dragged (*i.e.* longer contact length). The resultant columnar grain morphology is more or less vertical as in the concentrated copper-boron, the copper-calcium, -cerium, -yttrium, and -zirconium ribbons (figures IV.2 and 4)

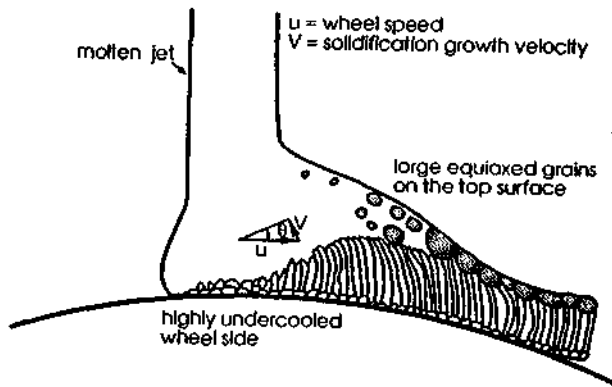

Figure V.1 Schematic diagram of the crystallization process during melt spinning according to Blank *et al.* [23]

At low wheel speeds or undercoolings, solidification occurred by cellular columnar growth for all alloys with small solidification intervals, as for the copper-chromium ribbons spun at 6 and 8 ms^{-1}, figures IV.1 and IV.20. In cases where the solidification interval was large, equiaxed grains were found almost throughout the ribbon thickness as exemplified by the transverse microstructure of the copper-boron ribbon spun at 11 ms^{-1}. These tendencies are shown schematically in figure V.2. The figures represent tendencies in ribbon microstructural changes with increasing alloy content and increasing wheel speed or ease of solubility extension. Shaded areas represent parts where segregation was observed. At high solidification rates, characteristic of large undercoolings, solid solution columnar grains were observed for alloys with small solidification intervals as for copper-chromium ribbons spun at above 16 ms^{-1}, figure IV.1. In cases where the solidification interval was large, solubility extension was limited to the wheel contact side of the ribbon. Above this zone, cellular columnar growth took place (figure V.2.c) as in dilute Cu-B ribbons (figure IV.4). For ribbons with moderately large solidification intervals the columnar grains extended to the top surface of the ribbon as for the dilute copper-boron or copper-yttrium-boron alloys spun at 43 ms^{-1}, figure IV.4. For very large solidification intervals like the

concentrated copper-boron, copper-calcium, -yttrium and -zirconium ribbons, a top equiaxed dendritic zone was observed, figure V.2.e and f, as in figure IV.2.

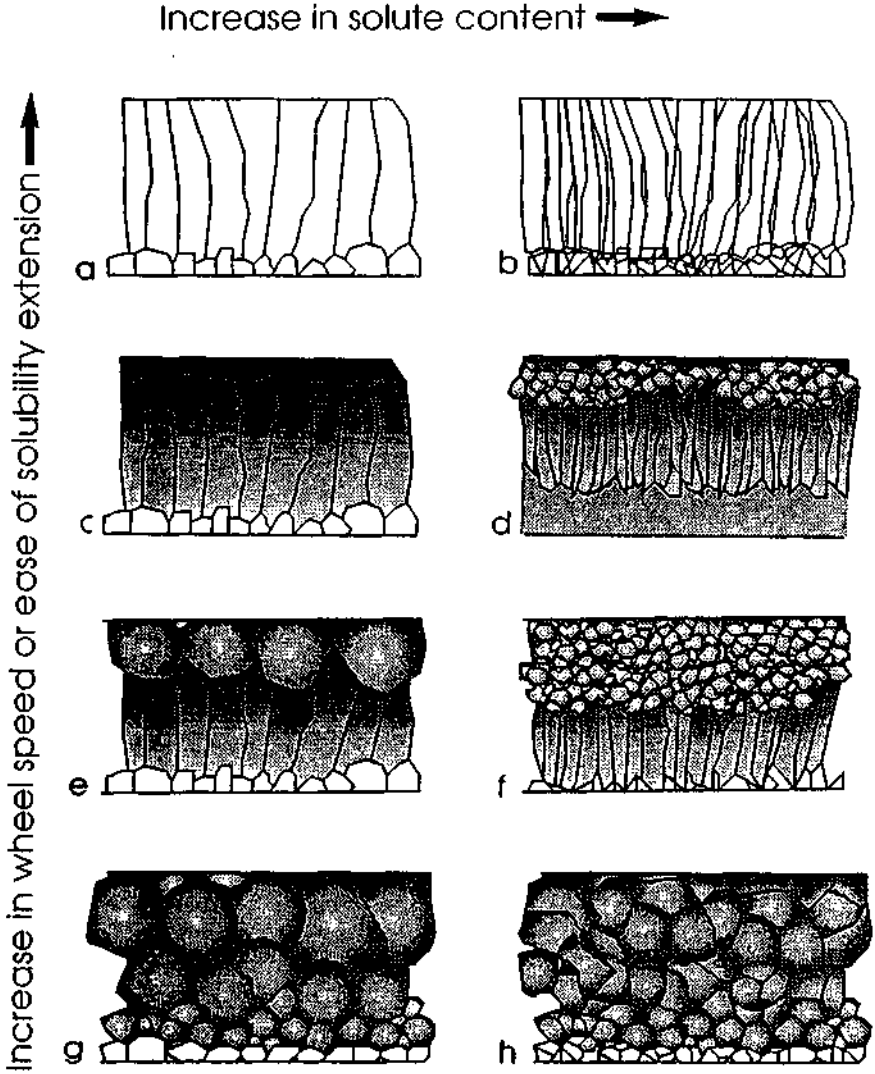

Figure V.2 Schematic diagrams of the evolution of the as cast ribbon microstructures. Horizontally the figures represent microstructures with increasing solute content and; vertically downwards, microstructures resulting from increasing wheel speed or from decreasing solidification interval. The shaded areas represent segregation.

The chromium-containing alloys were characterized by small solidification intervals. Their ribbon grain structures, figure IV.1, were similar to figures V.2.a, b and c, and depended on chromium concentration and casting speed. Thermal transfer conditions dominated ribbon formation and columnar grain growth was sufficiently rapid to avoid the nucleation and growth of equiaxed grains in the melt above the moving solid liquid interface.

Because of the larger solidification intervals of the copper-calcium, -cerium, -yttrium and -zirconium ribbons, ribbon formation was momentum and not heat transfer controlled. This resulted in growth of straight cellular columnar grains and in crystallization of the liquid above the solid originating from the wheel surface producing segregated equiaxed grains on the ribbon top surfaces, figure IV.2, with microstructures similar to figures V.2.c, d e and f. Increasing the solute content decreased the size of the wheel contact zone where solute trapping occurred. This is explained by the increase of undercooling necessary for partitionless solidification with solute content (*c.f.* section 5.1.2.2 and 5.1.2.3). This also refined the cellular columnar zone and increased the size and refined the structure of the dendritic equiaxed top zone as in the copper-yttrium ribbons (figure IV.2).

The evolution of grain structure in boron containing ribbons, figure IV.4, was similar to that in figures V.2.c and d. At high wheel speeds and low boron concentrations the ribbons consisted of a narrow equiaxed grain structure where solubility extensions occurred at the wheel side. Columnar cellular growth throughout the rest of the ribbon thickness exhibited no detectable solubility extension. At high wheel speeds and solute concentrations, a large zone of equiaxed crystals 50 nm in size followed by a cellular columnar and a small top layer of equiaxed dendritic grains was observed (figure V.2.d and IV.4.b). In these ribbons the wheel contact zone was relatively thick with respect to the grain size. A large portion of the melt was therefore sufficiently undercooled permitting copious nucleation, resulting in a fine grain size. With large undercooling and the fact that these grains are not limited to the wheel surface (encouraging heterogeneous nucleation) homogeneous nucleation of these grains could be possible. Boron is known to decrease crystal growth rates in copper alloys as described by Willnecker *et al.* [143]. The combination of slow growth and high nucleation rates resulted in the fine wheel side structure obtained. Transition to columnar cellular growth in the middle of the ribbon occurred during recalescence where, as in other ribbons, grains having favorable <100> orientations predominated. (Competitive growth results in a transition from equiaxed to columnar, while recalesence and competitive growth resulted in the modification of the grain morphology and solidification mode.) The slow growth of the columnar grains in the presence of boron enabled the nucleation and growth of equiaxed grains on the top surface of the ribbon. This explains the third narrow top surface structure observed in the Cu-B7.3 at% ribbon (figure IV.4.b). It could also be seen that the size of each zone

was dependant on the wheel speed. At low casting speeds the top surface structure dominated, while at high velocities, the bottom wheel side structure prevailed. This is clearly understood from the relative undercooling obtained in each section of each ribbon. At low undercoolings (low wheel speeds) nucleation on the top surface, either caused by impurities or small crystal clusters dominates (broken off from the growing solid due to convection in the melt puddle) since growth is independent from the heat transfer through the ribbon thickness. While at high undercoolings, columnar growth reaches the top surface before nucleation occurs in the liquid above the moving columnar grain interface.

5.1.2 Solute distribution and solubility extension in precipitation hardening alloys

Solubility extension is dependent on the competitive nature of phase selection during rapid solidification. It is necessary to suppress nucleation and growth of the equilibrium intermediate phases in favour of the formation of a metastable solid solution. The prediction of such metastable crystalline solid solutions depends on alloy chemistry, the thermodynamics of solid solution formation and the kinetics during rapid solidification. The following account deals with these three aspects for the solutes used in this study.

5.1.2.1 Alloy chemistry

The use of Darken-Gurry plots, based on electronegativity and atomic size differences, in predicting the extent of solid solubility have demonstrated some accuracy for many systems [144]. More recently, plots based on ΔH_S, the heat of solution, calculated from the semiempirical Miedema theory for the enthalpy of solution of disordered alloys, and, r_W, the atomic Wigner-Seitz radius, have been more predictable for solid solubilities [145-147]. Figure V.3 shows such a plot for copper as a solute according to Alonso *et al.* [148]. The ΔH_S values in this plot are calculated for equiatomic solid solutions of solute and copper. The dashed contour plotted by the authors separates the insoluble elements (maximum solid solubility less than 1 ^{at}%) from the soluble. It is important to note that these predictions are not infallible, many exceptions exist, as antimony, iron, iridium, silver and tin which should be within the boundary. However, these representations may be used for the prediction of some trends in alloy chemistry.

The dashed contour is shifted towards negative values of ΔH_S. The solubility region is bounded vertically by the size mismatch which contributes to the heat of solution with a repulsive (positive in value) term and corresponds to the size rule proposed by Hume-Rothery [144]. The shift in equilibrium solubility boundary towards negative ΔH_S values may be explained by the favorable situation in having a negative ΔH_S which gives a larger negative free energy change of the solid solution. If ΔH_S is positive, the free energy change in the formation of a solid

solution becomes less negative. Depending on the magnitude of a positive ΔH_s the result can be positive free energies of solution which lead to insolubility of the solute. The contour is, however, bounded to the left because very large negative heats of solution, suggesting intermetallic and not solid solution formation.

Based on this and previous studies an extra contour, larger in size, was drawn on the original figure of Alonso *et al.* [148]. It connects elements that have shown metastable solid solution extensions up to 3 at% by melt spinning, notably chromium, cobalt, iron, magnesium tin and titanium. Bearing in mind the predictibility of this theory, within this second contour, other elements such as boron, cadmium, niobium and vanadium are found which would suggest that these solutes might demonstrate solubility extensions by rapid solidification.

Calcium, cerium and yttrium are situated far away from the solubility boundary. The combination of their large negative heats of solution, suggesting that the intermetallic phase was hard to suppress, and their large size difference made solubility extension by rapid solidification difficult. The predicted solubility extension could only be small as was confirmed experimentally. The present experimental observations showed that ribbons spun at the fastest casting speed had only slight extension in solubility within the narrow zone at the wheel contact side where the undercooling was greatest. The rest of the ribbon contained second phase particles, which confirmed the above predictions that solutes with large differences in chemical nature are unsuitable for solubility extension by rapid solidification.

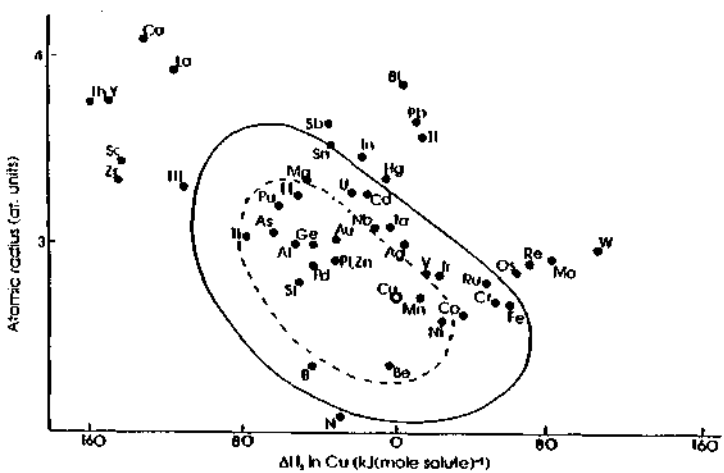

Figure V.3 Wigner-Seitz radius of the solute against the heat of solution calculated using the Miedema semiempirical relation calculated by Alonso et al. [148]. The broken curve encloses the soluble elements (maximum equilibrium solubility in excess of 1 at%) in copper. The solid curve encloses some of the elements where possible solubility extensions above 3 at% may be observed by rapid solidification.

5.1.2.2 Thermodynamic conditions for partitionless solidification

Figure V.4 shows equilibrium phase diagrams of the copper-chromium and copper-yttrium systems [6, 21]. The T_o line is drawn, based on equation 2 of section 2.2.3.1, page 18. For the copper-chromium system up to the eutectic composition the undercoolings necessary to attain the T_o line are small. This would suggest that it is easy to extend solubility by rapid solidification such that the kinetic partition coefficient tends towards unity. An undercooling of 2.5 K is necessary for the eutectic composition, at 1.56 at% chromium. However, for hypereutectic mixtures, due to a very steep liquidus after the eutectic composition, the undercooling increases rapidly. Extrapolation of the above data to a concentration of 5 at% chromium shows that the undercooling necessary is above 200 K. Such undercooling is difficult to realize throughout the whole of the ribbon thickness under standard melt spinning conditions, but may be obtained near the wheel contact side of the ribbon (*cf.* section 5.1.1, page 93). These observations explain why a limit of approximately 2.5 at% chromium supersaturation was observed by melt spinning chromium-containing alloys.

For the copper-yttrium system, figure V.4.b shows that the T_o line drops rapidly as the concentration of the alloy increases. For the copper-calcium, -cerium, and -zirconium systems, similarly plunging T_o lines are found. The undercooling necessary for partitionless solidification increases very rapidly with composition. This is in agreement with the present experimental observations where slight solubility extensions were attained only in the heavily undercooled wheel contact zone of the ribbons.

5.1.2.3 Kinetics of solidification

In section 2.2.3.3 it was shown that the value of $C_o^{crit.}$ can be used to assess the ease of solubility extension by rapid solidification. Table V.1 shows the estimated $C_o^{crit.}$ for different binary copper alloys where Γ, the Gibbs-Thomson coefficient, was taken as 1.5×10^{-7} Km for pure copper [149]. The interatomic jump distance, a_o, was taken as 0.5×10^{-9} m. An iterative calculation of V_a in order to determine $C_o^{crit.}$ with the kinetic term of $k_v(V)$ was not carried out. $C_o^{crit.}$ was calculated with a constant equilibrium partition coefficient.

In table V.1 it is suggested that chromium and niobium are more easily into solution by rapid solidification than the other solutes. In the present study the ease of chromium solubility extension was confirmed experimentally. It is to be noted that no copper-niobium alloy was rapidly solidified in this study because of the difficulty in producing non-contaminated ingots (section 4.1.1, page 41).

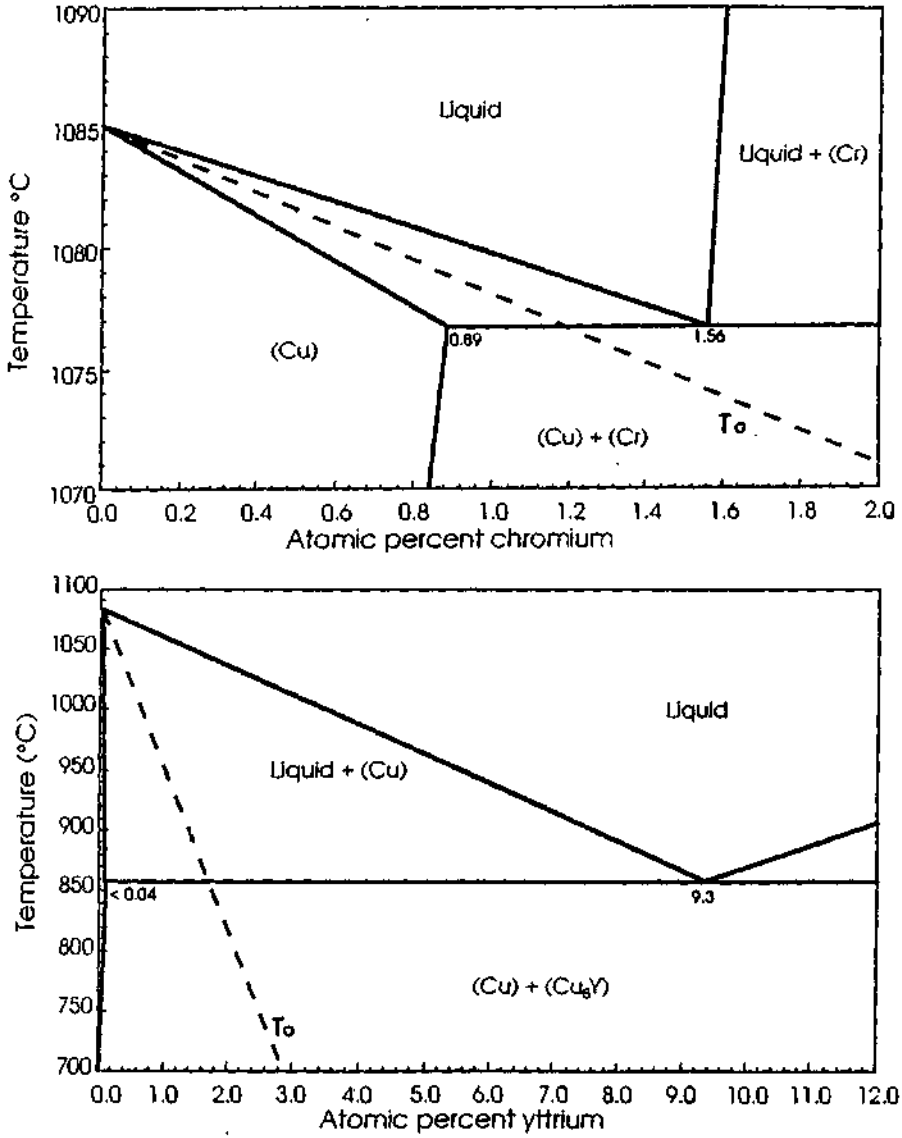

Figure V.4 Phase diagrams of copper-chromium (a) and copper-yttrium (b), with the calculated T_o line based on equation 10 in section 2.2.3.3, page 18.

Table V.1 Equilibrium partition coefficient, liquidus slope and $C_o^{crit.}$ of various solutes in copper.

Element	Equi. part. coef., k [-]	liquidus slope, m [K/at%]	$C_o^{crit.}$ [at%]
Boron	0.12	-5.3	0.93
Calcium	(0.0)¶	-16.6	(0.0)
Cerium	0.01	-23.2	0.002
Chromium	0.57	-5.3	42.7
Hafnium	0.003	-22.5	1.2×10^{-4}
Niobium	0.5	-20	7.5
Yttrium	0.004	-22.0	2.2×10^{-4}
Zirconium	0.02	-20	.006

For the copper-chromium alloy, the $C_o^{crit.}$ calculated was 42.7 at%, suggesting that the observed solid solution extension for all the copper-chromium alloys cast at fast melt spinning rates occurred by growth at absolute stability. However, the solubility extension of chromium was limited to 2-3 at%, total solubility extension was not observed for hypereutectic ribbons containing 5 at% chromium. Two reasons can explain this situation: (a) the $C_o^{crit.}$ calculation considers only copper as primary phase, and; (b) the very steep rise in the liquidus after the eutectic point calls for very large undercoolings to suppress the formation of primary chromium. This results in the formation of primary chromium particles during melt spinning [17].

Since $C_o^{crit.}$ determines the concentration above which solubility extension occurs by solute trapping it would be interesting to estimate the average interface velocity during the melt spinning process and compare it with the value of V_t. With the assumption that the final ribbon thickness is determined by the growth of the solid as long as the solidifying ribbon is in contact with the wheel (ribbon formation is primarily heat transfer controlled), the average interface velocity during melt spinning can be estimated. If a contact length of 5 mm* is taken, a wheel speed of 43 ms^{-1} and a ribbon thickness of 30 µm, the average interface velocity is estimated to be 0.3 ms^{-1}. As was shown by Liebermann *et al.* [142], the interface velocity varies considerably between the wheel contact portion and the free surface of the ribbon. This suggests that the value of 0.3 ms^{-1} is an underestimate at the wheel side, and an over estimate at the free surface of the ribbon. This was also confirmed in this study by the variation in the solidification structures observed. For example in the copper-yttrium and dilute copper-boron ribbons solute trapping

¶Values in curved brackets represent no detectable solubility in the solid state.

*This length was estimated from video films of the melt spinning process.

occurred near the wheel side and cellular columnar growth was found in the middle portion of the ribbon, evidencing different solidification rates.

If solute diffusivity in the liquid at the melting point is taken as $5x10^{-9}$ m^2s^{-1} [149] and a_o is approximated as 0.5 nm, the value of V_t is calculated as 10 ms^{-1}. Since for ribbons cast in this study, the average interface velocity was estimated as 0.3 ms^{-1} this would suggest that for some systems, the local interface velocity might have reached the value of V_t in the highly undercooled wheel contact zone of the ribbons. Solubility extension by partitionless solidification with an interface velocity close to V_t might have therefore occurred in calcium, cerium, yttrium and zirconium-containing alloys where the solute concentration was higher than $C_o^{crit.}$. Through the rest of the ribbon, the undercoolings were insufficient to attain V_t, leading to the absence of any detectable solubility extension in the middle or top portions of the ribbons.

If a cellular arrangement of the particles is observed, it is understandable that this arrangement is the result of cellular or dendritic growth during solidification. However, if the particles are arranged in a non-cellular manner, for the alloys studied, this may be the result of: a) primary solidification from the melt due to a hypereutectic composition of the alloy as in the Cu-Cr5 at% ribbons, or; b) in hypoeutectic compositions where there are two possibilities; first, as a result of precipitation of the second phase during secondary cooling of the ribbon and second, as a result of microsegregation where the cellular spacing is sufficiently small to allow for a quasi-uniform distribution of particles.

In certain microstructures, for example, the hypoeutectic copper-yttrium ribbons, it is interesting to study the reasons why in the as cast state the microstructure consisted of a uniform distribution of particles (figure IV.28). Table V.1 suggested that rapid solidification would result in segregation of yttrium because of its low $C_o^{crit.}$ which would result in cellular or dendritic growth. However, the second phase particle distribution in the cast ribbon was uniform and not in a distinct cellular arrangement. To determine whether this distribution was the result of precipitation or microsegregation, the maximum possible particle size resulting from precipitation during secondary cooling can be estimated by calculating the diffusion distance of the solute during cooling. A similar calculation as that carried out by Ellis and Michal for copper-chromium-niobium ribbons [42] showed that the maximum diffusion distance for yttrium atoms during secondary cooling was 29 nm. This corresponded to a maximum precipitated intermetallic particle size of 5.5 nm. Since the actual intermetallic particle radius in the as cast ribbon was 23 nm, this analysis suggests that the particles present are not the result of precipitation during secondary cooling but of fine segregation during solidification which confirms the discussions of the previous sections.

The $C_o^{crit.}$ for boron was calculated as 0.93 at% suggesting that up to this concentration solid solution extension can be obtained by growth at absolute

stability. As mentioned earlier growth at absolute stability would occur at higher concentrations since the $C_o^{crit.}$ calculated using equilibrium parameters is an under estimate of the effective $C_o^{crit.}$ if the kinetic parameters were to be used. Above this limiting concentration, partitionless growth occurs. In this study boron solubility extension was observed for the Cu-B2.7 at% ribbon spun at 43 ms^{-1} in the wheel contact side of the ribbon. Because the value of $C_o^{crit.}$ was not precisely known, it was difficult to determine whether the solubility extension observed was due to growth at absolute stability or by partitionless solidification. In the middle and top portion of the ribbon, cellular growth without any noticeable solubility extension occurred due to slower interface velocity. However, the high cooling rate resulted in the formation of an amorphous phase from the boron-rich intercellular liquid, avoiding nucleation and growth of the equilibrium crystalline phase.

5.1.3 Thermodynamics of dispersoid formation in microsegregated dispersion hardening alloys

Section 5.1.2 discussed solute trapping leading to supersaturation to obtain precipitation hardened materials. In some cases supersaturation was not obtained but resulted in microsegregation of solute forming cellularly distributed particles in the solid. These particles were consequently larger than what would have been obtained by precipitation and did not have the required strength after annealing as shown in figures IV.10 and IV.12. Thermodynamically more stable particles are therefore of greater interest. However, the development of finely distributed stable particles by rapid solidification poses a thermodynamic incompatibility. In the context of this study, thermally stable dispersions are necessarily insoluble in the solid state. The formation of an adequate volume fraction of dispersion requires that the dispersion be sufficiently soluble in the liquid. The combination of these two requirements is hard to satisfy.

As observed in Cu-ZrB_2 and Cu-TiB_2 ribbons, the solubility of these borides in liquid copper was negligible. After solidification, a very small volume fraction of fine dispersion was found. The majority of the boride particles present were large inclusions in suspension in liquid copper before casting. Two examples are cited to demonstrate the formation of dispersoid; YB_6 where approximately 2 vol% of dispersoid was obtained after rapid solidification, and ZrB_2 where the volume fraction of finely distributed dispersoid in the solid was negligible.

In presence of boron, the heats of solution of both zirconium and yttrium in liquid copper must neither be too positive nor too negative. Large negative heats of solution (with respect to the heat of formation of the boride) would lead to the formation of an intermetallic with copper. This condition is unlikely since the copper intermetallics encountered in this study are less stable than their metal borides. Positive heats of solution can result in liquid immiscibilities. In the present work this situation was encountered with the copper-chromium-boron, copper-cobalt-boron

and copper-iron-boron systems. An explanation of this behaviour can be given based on the work of Verhoeven and Gibson [150], who observed that in presence of an impurity (oxygen in their case) the eutectic reaction in the copper-niobium system was modified to a monotectic. The flat liquidus, characteristic of the copper-niobium system, is also found in the copper-chromium, copper-cobalt and copper-iron phase diagrams and a monotectic reaction has also been reported by Siedschlang for the copper-chromium system [151]. It may be assumed that in the presence of boron the free energies of the liquids are modified resulting in large positive deviations from ideality, transforming the flat liquidus into an immiscibility gap.

In order to produce a homogeneous liquid, the value of ΔH_{net}, the enthalpy change on forming the boride from elements in solution should be studied. The dissolution reaction of the boride can be written as:

$$M_\alpha B_\beta \rightarrow \alpha\underline{M} + \beta\underline{B} \qquad -\Delta H_{net} \quad (1)$$

where a and b are stoichiometric parameters, $\underline{B}$ and $\underline{M}$ respectively represent boron and the metal in solution in liquid copper and ΔH_{net} the enthalpy change of the reaction. The value of ΔH_{net} cannot be determined directly, but can be obtained knowing the enthalpy of formation, ΔH_f, of the boride from its elements:

$$\alpha M + \beta B \rightarrow M_\alpha B_\beta \qquad \Delta H_f \quad (2)$$

and the partial heats of solution in the liquid $\Delta\bar{H}_s$, of the elements in copper:

$$B \rightarrow \underline{B} \qquad \Delta\bar{H}_s^B \quad (3)$$

and

$$M \rightarrow \underline{M} \qquad \Delta\bar{H}_s^M \quad (4)$$

from equations 2, 3 and 4, ΔH_{net} of reaction 1 is calculated:

$$\Delta H_{net} = \Delta H_f - \alpha\Delta\bar{H}_s^M - \beta\Delta\bar{H}_s^B \quad (5)$$

A large negative ΔH_{net} would result in a heterogeneous liquid with boride particles in suspension as in the case of ZrB_2. Small negative values of ΔH_{net} are therefore favoured, otherwise the temperatures necessary to dissolve a reasonable volume fraction of boride would become impracticably high. In order to satisfy the condition of a small negative ΔH_{net} in the liquid, both $\alpha\Delta\bar{H}_s^M$ and $\beta\Delta\bar{H}_s^B$ should be large and negative. However, in the solid a large negative ΔH_{net} is required to produce dispersions resistant to coarsening. The dilemma arises from the fact that

in the solid state, $\Delta\bar{H}_s^M$ and $\Delta\bar{H}_s^B$ have to be positive, or at least less negative to satisfy the demand of solid insolubility.

Sato and Kleppa determined the partial heat of solution of boron in liquid copper to be 7.13 kJmol^{-1} for dilute copper mixtures [152]. Due to the lack of thermodynamic data as well as the uncertain liquidus lines in the copper-yttrium and copper-zirconium phase diagrams the enthalpies of mixing of both yttrium and zirconium in copper could not be obtained. As a first approximation, it can be assumed that $\Delta\bar{H}_s^M$ for both yttrium and zirconium are equal due to the similarity of the phase relationships. The heats of formation of ZrB_2 and YB_6 are respectively -310 kJmol^{-1} [75] and -100 kJmol^{-1} [127]. Substituting the appropriate values into equation 5, it can be seen that the ΔH_{net} for ZrB_2 is approximately three times larger than that of YB_6. This high negative value of ΔH_{net} for ZrB_2 explains the experimental difficulty in dissolving a sufficient volume fraction of the compound in liquid copper at 1500°C. This analysis shows that the ideal dispersion in copper should have a small negative enthalpy of formation per atom, ΔH_f^{atom}, as for YB_6, of approximately -100/7 kJmol^{-1} ≈ 14 kJmol^{-1}. As demonstrated by the present experiments, small negative ΔH_{net} values obtained from large negative ΔH_f, $\Delta\bar{H}_s^M$ and $\Delta\bar{H}_s^B$ were difficult to satisfy in practice. This restricted the choice of the dispersoid to those with a small negative ΔH_f^{atom}.

5.1.4 Summary

These analyses have shown that the grain structure of rapidly solidified ribbons was dependent on wheel speed and the solidification interval of the alloy. Depending on the growth kinetics, one, two or three distinct zones could be distinguished within the ribbon. The kinetics of solidification were of particular importance in predicting and explaining the resultant rapidly solidified microstructure in terms of the interface velocity. Furthermore, thermodynamic characteristics of the solute were relevant in predicting solid solubility extension of different solutes by rapid solidification.

It was also shown that because the restrictions imposed by conductivity and strength the number of binary systems were limited when a large volume fraction of fine precipitation of second phase particles is to be obtained from supersaturation. The alloys which proved to be promising were based on the copper-chromium, and to a lesser extent, the copper-zirconium systems.

Sections 5.1.2 and 5.1.3 showed that there are limitations in choosing a solute that would provide a large volume fraction of second phase particles with elevated thermal stability, for both precipitation and microsegregation dispersoid-hardened materials. For both types of materials it was shown that a compromise on thermal stability was necessary: a) for precipitation hardened alloys, when a large volume fraction of particles is needed, techniques such as melt spinning and powder atomization do not provide sufficiently high solidification rates for the metastable

solubility extension of elements such as cerium, yttrium and zirconium which would be interesting from a thermal stability view point, and; b) for microsegregated dispersoid-hardened alloys, the choice of a stable dispersoid was limited by liquid equilibrium thermodynamics which determine the volume fraction of dispersoid distributed finely in the rapidly solidified material.

In those cases where the dispersed phase was not obtained by precipitation from a supersaturated solid, thermally stable microsegregated dispersed particles resulting from solidification were of interest. It is necessary that the thermal stability of microsegregated microstructures be better than that of alloy systems having solubility extension by rapid solidification. If the structure initially contains dispersed particles, those particles must have lower coarsening rates than particles which arise from precipitation. The latter particles will first precipitate finely from the supersaturated matrix and then coarsen before reaching the size of the dispersed particles present in the microsegregated ribbon.

5.2 Mechanical properties

5.2.1 Microhardness measurements

Hardness measurements carried out on either side of copper-boron and copper-yttrium ribbons showed distinct differences. For these materials there was no evidence of supersaturation on the free surface of the ribbons as confirmed by the absence of age hardening, figures IV.11 and IV.16. In contrast, the wheel side of the ribbons showed signs of solute supersaturation. Based on the relative degrees of age hardening observed for the copper-boron ribbons wheel sides of the two alloys, and assuming that all the 2.7^{at}% boron of the dilute alloy was retained in solution (figure IV.32), it can be concluded that some 5-7^{at}% boron was retained in solution, at the wheel side, for the concentrated alloy. As for the wheel side of the Cu-Y0.7^{at}% ribbon, the age hardening observed suggests some solubility extension of yttrium.

5.2.2 Tensile tests

The evolution of strength of binary chromium-containing ribbons depended on casting speed. At high casting speeds, after heat treatment a large volume fraction of uniformly distributed particles was obtained by precipitation and growth of chromium. The mechanical properties may in this case be simply explained in terms of particle and grain size strengthening. However, at low casting speeds, the strengths measured were the result of a more complex microstructure having a bimodal distribution of particles. The structure either consisted of a uniform distribution of two distinct particle sizes (ribbons spun at 8 ms^{-1}, figure IV.24), or of large particles arranged in a cellular manner and fine particles, arising from precipitation, uniformly distributed within the microstructure (ribbons spun at

6 ms^{-1}, figure IV.21.d). It is only by examination of the microstructure of the melt spun ribbons in the as cast state and after annealing that the parameters needed to explain the observed flow strengths can be determined.

It was shown in several occasions [19, 41, 47, 48] that the flow strength of mechanically alloyed or rapidly solidified and aged, dispersion hardened, copper alloys can be explained by equation 10 in section 2.3, page 22. It is necessary, however, to confirm that the particles present in the matrix at peak and overaged states are not cut by dislocations. Figure V.5 shows dislocation/particle interactions in a heat treated copper-chromium ribbon deformed 2% in tension. The weak beam image shows how the dislocations are anchored by the particle. For smaller particle sizes similar interactions were observed. In the chromium-containing alloys the cigar shape of the bcc chromium-rich particles would suggest a certain coherency with the fcc copper matrix. Weatherly *et al.* [153] showed that the orientation relationship between the copper matrix and the chromium needles was of the Kurdjumov-Sachs type, with $<651>_{Cu}$ growth axes on {111} planes preferred. Even though a certain coherency of the particles is observed, the Orowan model can be applied since no particle shearing was observed.

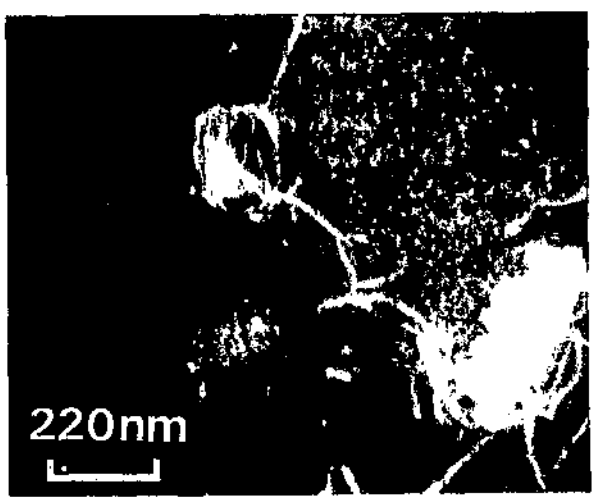

Figure V.5 Weak beam micrograph of dislocation/particle interaction in Cu-Cr1.85 at% ribbon cast at 26 ms^{-1}, heat treated 30 min at 700°C and deformed 2%.

For a volume fraction of 2vol%, the planar centre to centre interparticle spacing can be considered sufficiently large with respect to the obstacle size that λ_p-ϕ can be replaced by λ in equation 10, section 2.3, page 22. Combining equation 11

(section 3.7.2.2, page38) with equation 10 (section 2.3, page 22) the following equation is obtained, thus:

$$\Delta\sigma \approx \frac{6}{\lambda_p} ln\left(\frac{\phi}{2b}\right) = 6\sqrt{\frac{f_v \phi}{\overline{V}}} ln\left(\frac{\phi}{2b}\right) \quad (6)$$

where $\Delta\sigma$ is the strength contribution due to Orowan looping.

Figure V.6 shows a plot of experimental flow strengths obtained on overaged ribbons plotted according to equation 6. The straight line relationship is closely followed giving a slope of 5.7 Nm^{-1}, close to the expected value of 6 Nm^{-1} for the Cu-Cr1.85 at%, Cu-Cr2.12 at% Zr0.18 at% and Cu-Cr2.44 at% Mg0.19 at%. The intercept of 53 MPa indicates the average value of the matrix strength for all of these ribbons having a grain size of 1-5 µm which suggests that the contribution of this fine grain size to hardening is far less than that of finely dispersed particles.

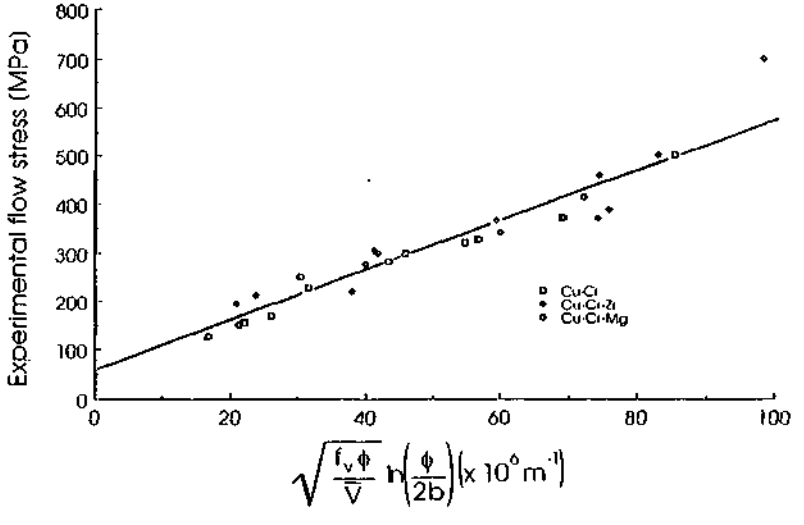

Figure V.6 Plot of the experimental flow stresses as a function of $\sqrt{\frac{f_v \phi}{\overline{V}}} \ln\left(\frac{\phi}{2b}\right)$ for the different alloys after various anneals.

5.2.2.1 Analysis of alloying additions to the copper-chromium alloys

Success in predicting the strength of these materials by Orowan strengthening mechanisms permit a better classification of the efficiency of the different alloying

additions made to the binary alloy. Based on equation 6, dividing the flow strength of the ribbons by the square root of the volume fraction of chromium present and normalizing to a volume fraction of 2 vol%, a direct comparison of the effect of various alloying additions can be made. Figure V.7 shows the variation of this normalized flow strength as a function of the different isochronal anneals. It is important to note that these comparisons can only be made for the peak and over aged materials where the Orowan mechanism controls strengthening, since during the early stages of precipitation (below 500°C) other strengthening mechanisms may operate.

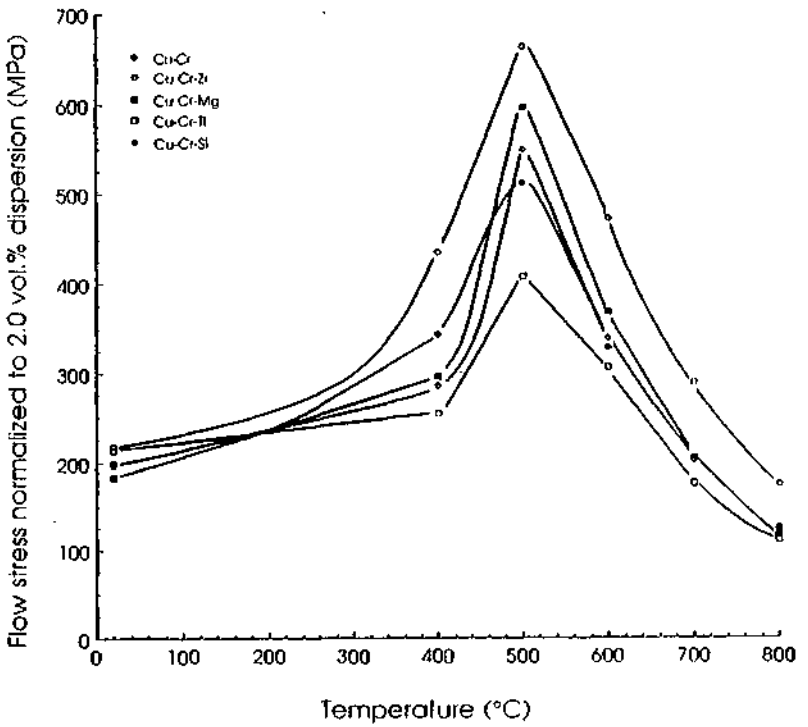

Figure V.7 Plot of flow stress at room temperature against isochronal annealing temperature. All the flow stresses are normalized to 2 vol% of chromium dispersion.

Figure V.7 shows the strengthening achieved after annealing samples for 30 minutes at each temperature. As such the peak strength at 500°C for each material corresponds to the situation where fine precipitation and sufficient particle coarsening has occurred such that an optimal particle size and spacing is obtained (particles sufficiently large to act as strong obstacles to dislocations and a very fine particle distribution). In view of the close similarity of coarsening kinetics within the

alloys examined and the similarity in temperature dependence of coarsening rate (as was illustrated in figure IV.27) it is unlikely that the relative positions of the curves in figure V.7 will be modified in any major manner by the choice of a shorter or longer ageing period. A longer ageing period would displace the peak in strength to a lower temperature since a longer time allows for optimal particle size to be achieved by slower coarsening at a lower temperature.

It is clear from figure V.7 that the different additions have their most pronounced effect in the peak aged condition - the strength of the alloy reflecting the fineness of the chromium dispersion. Compared with the binary alloy, zirconium proves to be the most effective of all the alloying additions. Not only does it substantially increase maximum strength, but it also helps retain relatively high flow stresses after further annealing. It should be noted that the volume fraction of zirconium rich particles present in the as cast state (figure IV.23) was not taken into account in this normalization. If these particles were to be considered, the Cu-Cr-Zr curve would be shifted down, but would still remain above the Cu-Cr-Mg line. Coarsening at 600°C was similar to that of chromium particles in other alloys (figure IV.27). The magnesium containing ribbons show a similar behaviour. Magnesium, present in solid solution at less than 0.2 at.%, cannot participate in strengthening by any supplementary precipitation. The superior strengths observed at 500 and 600°C were therefore due to finer chromium precipitation. The effects of silicon addition are small and are only felt at maximum strength where the flow stress is increased by about 20 MPa relative to the binary alloy. Titanium on the other hand had a deleterious effect on mechanical properties. As the concentration of titanium increased, the strength of the alloy fell to levels below that of the binary alloy (table IV.1).

The coarsening kinetics for chromium particles in the binary as well as the ternary magnesium, titanium and zirconium containing alloys were the same at 600°C (figure IV.27). On the basis of coarsening alone it is therefore impossible to explain the large differences in mechanical properties discussed above for the different alloys. Titanium and zirconium containing ribbons, for example, had virtually the same particle coarsening rates, but differed in strength by more than 300 MPa after peak aging. Coarsening kinetics will be analyzed in detail later in this chapter both on the binary and the ternary zirconium-containing ribbons. However, the result of this analysis is important to be stated. Virtually identical values of the activation energy for bulk diffusion of chromium in the binary and the ternary zirconium-containing alloys were obtained. This leads to the conclusion that the presence of zirconium atoms does not modify in any appreciable manner the mechanism of chromium atom transport within the copper matrix and, therefore, is not the reason for the variations of strength observed.

One reason for the different strengths is seen by examining the effect of ternary additions on projected aspect ratio. Ternary alloy additions affected the aspect ratio

of the chromium particles, zirconium kept it close to unity, while after a sufficient time/temperature treatment, titanium increased this value to above 3 (figure IV.27). The reason for this difference in morphology between the zirconium and titanium containing alloys is not fully understood. It is nevertheless clear that for substantially over aged states, the zirconium containing alloy has preferable mechanical properties when compared with the titanium containing ribbon. Particle thickening being the same for all the alloys (figure IV.27), titanium additions induced fast longitudinal growth, resulting in a rapid increase of the average volume of the chromium particles. The average interplanar particle spacing was therefore increased and the strengthening contribution of these particles with respect to the zirconium containing alloy decreased.

A second reason for the different strengths of the different alloys may also arise from the different fineness of the initial precipitation before coarsening occurs. Detailed analysis by Tang *et. al.* [10] on precipitation in copper-chromium-zirconium and copper-chromium-magnesium alloys showed that precipitation followed a two stage process. By electron diffraction, they showed that a complex intermetallic phase having a Fm3m symmetry (Heusler phase) initially formed with a composition $CrCu_2(Mg,Zr)$. On further annealing, this metastable phase decomposed to bcc chromium and Cu_4Zr particles for the zirconium containing alloy and bcc chromium and magnesium in solid solution for the magnesium containing alloy. They also claimed that the presence of impurities in the simple copper-chromium alloy may favorize this initial metastable precipitation. These observations can be used to explain the differences in mechanical properties at peak strength for the zirconium and magnesium containing ribbons (before the chromium particles take up significant cigar-shaped morphologies). The homogeneous metastable precipitation of the Heusler phase in the zirconium and magnesium-containing alloys, heavily supersaturated after rapid solidification, results in a finer particle size distribution, compared to the binary alloy where this initial phase does not form. The complex intermetallic precipitated as a very fine distribution which thereafter decomposed as described above. This resulted in a particle size distribution which was finer in the zirconium and magnesium modified alloys compared to the binary alloy which followed the normal precipitation sequence [153]. The effect was less marked for the silicon modified ribbons. Silicon being markedly different in size and electronegativity from zirconium and magnesium and quite similar to copper, can be considered less efficient in inducing this metastable precipitation. The existence of TiO_2 particles in the as cast state for the titanium containing alloy leads to an opposite effect to that of zirconium and magnesium. Heterogeneous nucleation of bcc chromium on these oxide particles results in a coarser particle size distribution of chromium. As the titanium concentration in the ribbon increases, the percentage of oxide in the ribbon also increases leading to greater losses of mechanical strength (table IV.1).

5.2.3 Summary

Analysis of the mechanical properties showed that the strength of cast ribbons depended on: a) the as cast microstructure (solute either segregated and/or in solid solution), b) the kinetics of change in microstructure during annealing (precipitation from supersaturation, phase transformation from metastable to stable, grain and/or particle coarsening), c) alloy composition (modification of strength or kinetics of microstructural change by small additions of an extra solute) and; d) the relative amount of each of the strengthening mechanisms that contribute to strengthening (bimodal distribution of particles, shearable and/or non-shearable precipitates, solidification cell and grain size).

The largest contribution to strengthening brought about by rapid solidification was due to dispersion refinement, resulting from either supersaturation and precipitation or particles produced after solute segregation. With respect to the fine particle dispersion, grain refinement was not believed to contribute significantly to strengthening.

Where a homogeneous distribution of particles was found, strength could be explained by the Orowan mechanism as expected for particles which are not cut by dislocations. Ternary additions to the binary chromium-containing ribbons modified considerably the mechanical behaviour of the alloy by influencing the precipitation and the morphology of the particles. Mechanical properties of copper-chromium alloys were enhanced by careful choice of alloying elements which modify the precipitation sequence resulting in a finer distribution of particles and/or precipitate morphology, decreasing the effective interparticle spacing. Zirconium proved to be the most effective of the alloying additions increasing the maximum strength of the copper-chromium ribbons, as well as retaining most effectively this strength after annealing at higher temperatures. The optimum zirconium concentration was found to be near 0.3 at% as was shown in figure IV.14. Addition of magnesium, like zirconium, increased the peak strength of the alloy by modifying precipitation, but its effects were lost during high temperature anneals.Titanium additions reduced the age hardenability of the ribbons to levels below the binary copper chromium alloy. The existence of oxide particles in the as cast ribbon provoked heterogeneous nucleation of bcc chromium. Homogeneous precipitation was thereby limited resulting in a coarser particle size distribution consequently reducing the strength of the material.

Microsegregation resulted in larger particles as compared to particles obtained from precipitation. As a result, for the same volume fraction of dispersion, precipitation hardened ribbons had considerably higher strengths (450 MPa for 1.91 vol% of chromium at peak strength) than microsegregated ribbons (450 MPa for 3.6 vol% of amorphous boron distributed in a cellular manner). In order to reach

similar strengths in microsegregated as in precipitation hardened ribbons, the volume fraction of dispersion had to be increased.

5.3 Thermal stability of the rapidly solidified microstructures

A knowledge of the mode and the kinetics of the transformation of metastable phases and microstructural coarsening is important for controlling alloy behaviour during fabrication, for example, during consolidation, working and heat treatment, and subsequently during service. The previous sections showed that the type of solute, the nature and distribution of the dispersion hardening phase influence the thermal stability of the alloy and in consequence affect its mechanical behaviour. It is therefore necessary to understand the mechanisms which control the thermal stability of the rapidly solidified material. This would allow the prediction of the behaviour of alloys with similar characteristics as well as the design of alloys with unique microstructures having improved thermal properties.

As shown in section 5.1 the solute choice as well as the processing parameters determine the rapidly solidified microstructure. The resultant melt spun ribbon was shown to have: a grain size determined by the solute content, undercooling and grain nucleation rate and; a particle size distribution depending on the solidification rate. These ribbons also contained other defects such as quenched-in vacancies and dislocations resulting from the rapid quench and deformation of the ribbon during processing. These defects, as well as other microstructural characteristics, will affect the thermal stability of the rapidly solidified material.

The grain size of the as cast microstructure influences the evolution of the microstructure during heat treatment. As the grain size decreases the volume fraction of grain boundary increases. These short circuit diffusion paths will promote particle coarsening. They also act as sinks for solute, draining the solute within the grains towards rapidly coarsening particles situated within the grain boundaries. This effect can clearly be seen in figure IV.21 where particle free zones on either side of the grain boundary can be distinguished in annealed copper-chromium ribbons. The influence of grain boundaries on microstructural evolution will be discussed in section 5.3.2.

Solubility extension was possible for some of the systems studied in this work. During subsequent heat treatment precipitation of the excess solute and coarsening occurred. For alloys where the as cast state contained preexisting particles, the distribution of particles after annealing is influenced by their presence. This can be clearly seen in figure V.8 of a copper-Ni_3B ribbon heat treated for 30 min at 600°C. Competitive growth between the small and large particles results in the drainage of solute from the small to the large particles resulting in particle free zones. Competitive growth between particles in a bimodal distribution was also seen in the Cu-Cr1.85 at% ribbon cast at 8 ms^{-1}, figure IV.25. The effects of particle distribution on the microstructural evolution will be discussed in section 5.3.1.

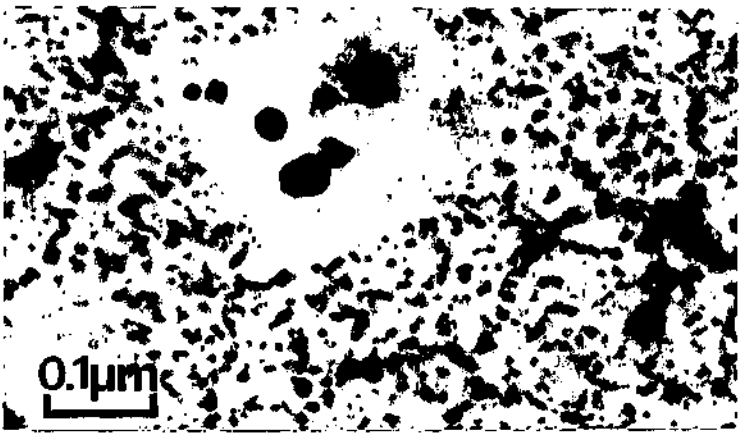

Figure V.8 Particle free zones surrounding large particles in a Cu-Ni 3at% B 1at% ribbon heat treated 30 min at 600°C.

5.3.1 Particle growth

The coarsening rate of second phase particles will depend on the interfacial energy of the dispersion as well as the solubility and diffusivity of the rate controlling element. Growth of the dispersed phase during heat treatment has been generally found to follow classical theories of bulk diffusion controlled particle coarsening [82, 83]. However in some cases, if no microstructural assessment is carried out (particle size is determined by indirect methods such as conductivity or scattering experiments), there might be some doubt with respect to the precise coarsening model to be used. In every analysis, the relative importance of the different transport paths should be evaluated for correct interpretation of results.

5.3.1.1 Establishment of the rate controlling transport mechanism during coarsening

The driving force for particle coarsening is the reduction of the total interfacial energy in a system. There is a tendency for smaller particles to dissolve and larger ones to grow by transfer of solute through the solvent. Section 2.4 reviewed the different size-time relations that have been established. Experimental data on coarsening is usually in the form of size-time-temperature plots. Analysis of such data may sometime lead to erroneous conclusions if the wrong transport mechanism is chosen, even through a good fit of the experimental points is observed with a r^n *vs.* t plot. Plotting the experimental data in log-log form may also be of little use, since this often results in a slope with an exponent n intermediate between two transport mechanisms. Such ambiguities arise because of experimental scatter, or of uncertainties in the solubility of the rate controlling element, whether in be in the bulk, in the dislocation pipe, or within the grain

boundary. The aim of the following development is to establish, based on microstructural observations such as dislocation density, particle and grain size, the rate determining transport mechanism and apply the analysis to the systems where coarsening was studied.

Section 2.4 showed that the solubility X_r, of a particle of radius r can be approximated by:

$$X_r = X_\infty \left(1 + \frac{2\gamma\upsilon}{kTr}\right) \qquad (7)$$

where υ is the atomic volume and k the Boltzmannl constant. If n is the number of solute atoms in a particle, the growth of a spherical particle can be written:

$$4\pi r^2 \frac{dr}{dt} = \upsilon \frac{dn}{dt} \qquad (8)$$

applying Ficks' first law:

$$\frac{dn}{dt} = - \frac{F(r)D}{\upsilon} \frac{dX}{d\xi} \qquad (9)$$

where ξ is the distance from the particle D the diffusivity and F(r) is the effective transport diffusion area [84]. As mentioned in section 2.4, the difficulty arises when calculating the concentration gradient $dX/d\xi$ for a distribution of particles. If the simplifications made in section 2.4.1 are accepted, equation 20, page 25, in the same section can be used, for a single spherical particle the concentration gradient can be approximated by:

$$\left[\frac{dX}{d\xi}\right]_{\xi = r} = \frac{X_\infty - X_r}{r} \qquad (10)$$

which leads, based on equations 7 to 10, to:

$$r^2 \frac{dr}{dt} = \frac{\gamma X_\infty \upsilon}{4\pi kT} \frac{DF(r)}{r^2} \qquad (11)$$

This equation can also be written:

$$r^2 \frac{dr}{dt} = \frac{\gamma X_\infty V_m}{4\pi RT} \frac{DF(r)}{r^2} \qquad (12)$$

where V_m is the molar volume of the particle.

In order to determine F(r) one must consider the diffusion area where solute predominantly arrives. Figure V.9 illustrates schematically the different modes of solute transport towards a particle. For bulk transport the diffusion area is the surface of the particle and $F(r)=4\pi r^2$, for grain boundary diffusion the area is restricted to $F(r)=2\pi r\delta$ where δ is the grain boundary thickness, while for pipe diffusion F(r)=Nq where N is the average number of dislocations arriving to a particle and q the cross sectional area of the dislocation pipe. Introducing the above values of F(r) and integrating equation 12 the established power laws of $r^n \propto t$ are found. The development carried out here for particle coarsening has not taken into account the conditions of continuity and conservation. LSW [82, 83] carried out this analysis and showed that a steady state distribution of particles is asymptotically reached. Equation 12 can be written, taking into account this analysis, as:

$$r^2\frac{dr}{dt} = \alpha'(f_v)\frac{\gamma X_\infty V_m}{4\pi RT}\frac{DF(r)}{r^2} \qquad (13)$$

where $\alpha'(f_v)$ is a numerical constant which is dependant on the volume fraction of dispersion and is equal to 27/8 for the LSW zero volume fraction approximation.

It can be seen that the magnitude of the product of F(r) and its appropriate diffusivity term will determine the dominating coarsening mode. In order to test this analysis the coarsening of chromium particles in binary chromium-containing ribbons cast at 26 ms^{-1} is studied below.

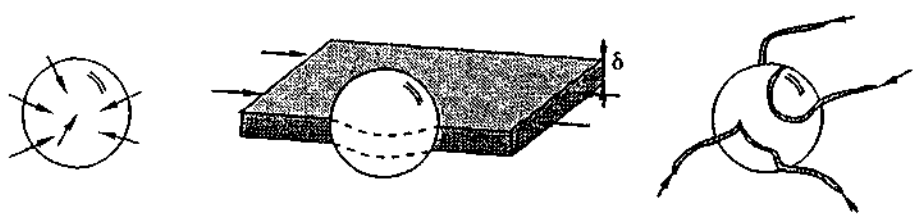

Bulk diffusion controlled
$F(r) = 4\pi r^2$

Grain boundary diffusion controlled
$F(r) = 2\pi r\delta$

Pipe diffusion controlled
$F(r) = Nq$

Figure V.9 Schematic representation of the different modes of solute transport.

5.3.1.2 Analysis of particle coarsening in solid solution chromium-containing ribbons

The diffusivity of chromium in dilute copper-chromium alloys was measured by Barreau *et al.* [154] and Saxena [155]. The two authors found that diffusivity followed the classical Arrhenius relationship with, respectively, a pre-exponential term D_o of 1.02×10^{-4} m^2s^{-1} and 1.6×10^{-4} m^2s^{-1} and an activation energy Q_{bulk} of 224 $kJmol^{-1}$ and 255 $kJmol^{-1}$. For the following calculations the bulk diffusivity of chromium in copper is approximated by:

$$D^{Cr}_{bulk} = 1.3 \times 10^{-4} \exp\left(\frac{240\ kJmol^{-1}}{RT}\right) [m^2s^{-1}] \qquad (14)$$

It is necessary to estimate the grain boundary and pipe diffusivities of chromium in order to determine the product F(r)D for the two other modes of transport. Gjostein [156] showed that the activation energy for pipe diffusion is approximately 3/4 that of bulk diffusion, while that of grain boundary diffusion can be approximated to half the activation energy of bulk diffusion. The frequency factors for each transport mode were found to be approximately equal. Figure V.10 shows the theoretical behaviour of F(r)D as a function of particle radius r, at 450°C and 700°C. For this representation an average of 4 dislocations per particle (N=4) was assumed, a dislocation pipe area of b^2, where b is the Burgers vector and the grain boundary thickness was taken to be 1 nm.

It can clearly be seen in figure V.10 that within the temperatures of interest the F(r)D term for grain boundary transport dominates the other two modes of transport. Particles situated on grain boundaries can therefore be considered to be uninfluenced by the other modes of transport, their coarsening being solely controlled by the arrival of solute via the grain boundaries. The discussion arises for particles within the matrix where a certain dislocation density can be distinguished. Under the assumptions made, at low and elevated temperatures, dislocation pipe diffusion would be the principle mode of transport for small particle sizes. For large particle sizes, bulk diffusion dominates.

In the as cast state the dislocation density was estimated as 6×10^{13} m^{-2}. Upon heat treatment precipitation of the excess solute, preferentially onto dislocations, will pin the existing dislocations and stabilize the initial density until the volume interparticle distance increases sufficiently by coarsening that dislocations are freed and annihilated. Figure V.11 shows the dislocation arrangement after 4.5 h at 750°C, the interparticle spacing is still not sufficient to decrease significantly the dislocation density estimated here at 4×10^{13} m^{-2}.

It is clear that the number of dislocations per particle will depend on the initial dislocation density,ρ, and the volume interparticle spacing, λ_v. The value of N can be obtained by considering the relation:

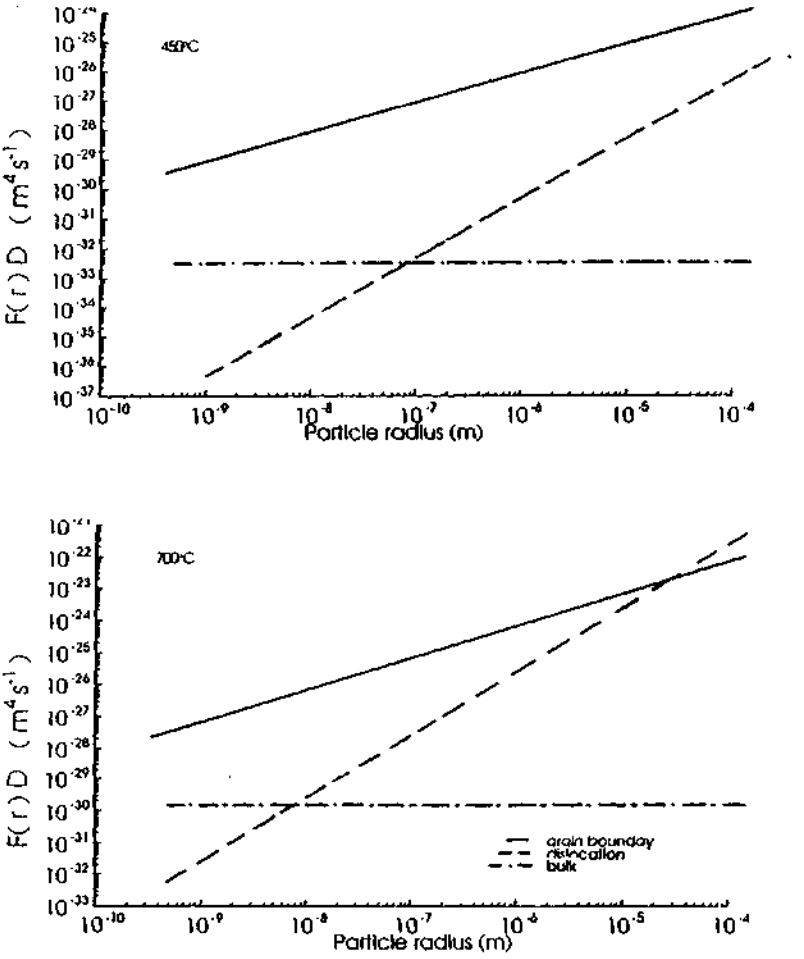

Figure V.10 F(r)D term (theoretical) for chromium particles in a copper matrix at (a) 450°C and (b) 700°C

$$N \approx \rho \lambda_v^2 \qquad (15)$$

where it is assumed that $N\lambda_v$ dislocation lengths are found in a volume of $(\lambda_v)^3$. Writing equation 15 as a function of particle radius:

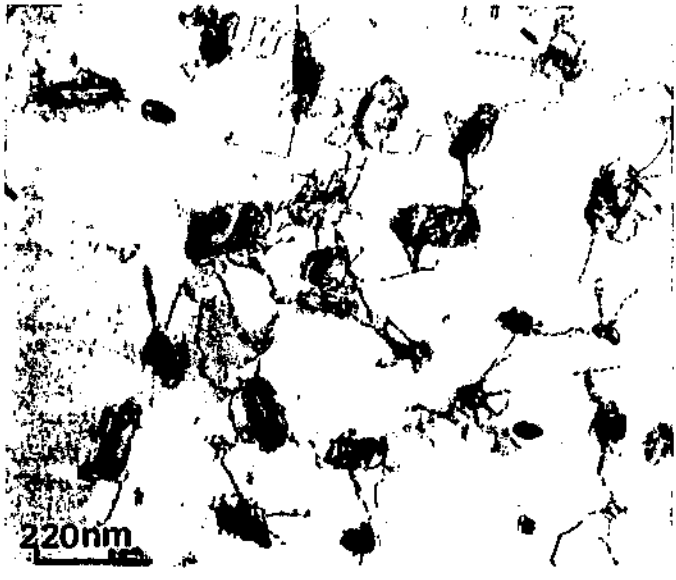

Figure V.11 Cu-Cr 1.85^{at}% ribbon melt spun at 26 ms^{-1} and annealed 4.5 h at 750°C.

$$N \approx \rho\, \alpha_v^2\, \bar{r}^2 \qquad (16)$$

where α_v is a proportionality constant defined by equation 12 in section 3.7.2.2, page 38. The transition from pipe diffusion to bulk diffusion controlled coarsening can be characterized by the condition:

$$4\pi r^2 D_{bulk} = NqD_{pipe} \qquad (17)$$

Substituting equation 16 in 17 and considering the assumptions made above with respect to bulk and pipe diffusion, a critical dislocation density for a given volume fraction and temperature can be defined:

$$\frac{1}{4\pi}\rho_{crit.}\, q\left(\frac{4\pi}{3f_v}\right)^{\frac{2}{3}} = exp\left(\frac{-Q_{bulk}}{4RT}\right) \qquad (18)$$

Dislocation densities larger than ρ_{crit} will promote pipe diffusion controlled coarsening and smaller densities promotes bulk diffusion. Figure V.12 shows the theoretical evolution of ρ_{crit} for a volume fraction of dispersion of 2^{vol}% and different bulk diffusion activation energies as a function of temperature. It can be seen that $\rho_{crit.}$ increases with temperature and decreases with increasing bulk

diffusion activation energy. Considering the experimentally observed dislocation densities (section 4.3.1, page 76), at elevated temperatures ρ_{crit} is higher ($\sim 10^{16}$ m^{-2} at 700°C and $\sim 10^{15}$ m^{-2} at 450°C) which suggests that the effect of pipe diffusion on coarsening rate of chromium particles at such temperatures can be neglected .

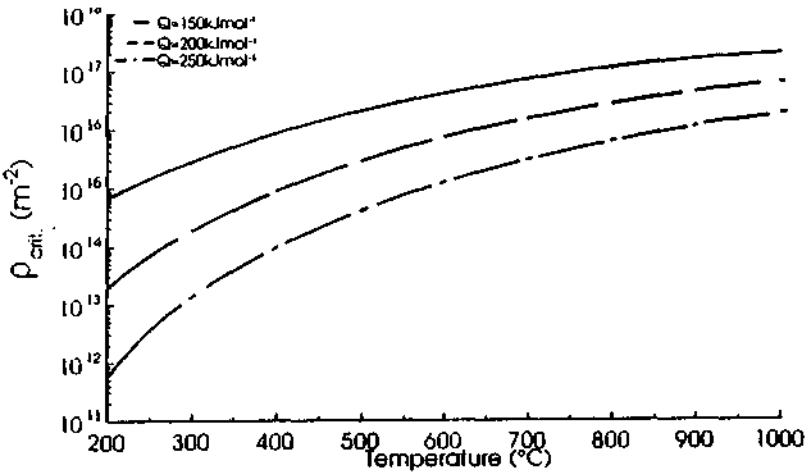

Figure V.12 Theoretical evolution of ρ_{crit} for a particle volume fraction of 2^{vol}% as a function of temperature and bulk diffusion activation energy, assuming similar frequency terms and an activation energy of pipe diffusion equal to 3/4 that of bulk diffusion.

If the annealing conditions and microstructural parameters lead to a value of ρ_{crit} close to the measured dislocation density, both pipe and bulk diffusion transport mechanisms should be considered (models for mixed transport including pipe and bulk diffusion were described by Kreye [104] and Slyozov [157]). It is only for measured densities significantly different from ρ_{crit} that one of the two transport mechanisms can be excluded.

Since the dislocation density observed in the copper-chromium ribbon was significantly less than $\rho_{crit.}$, bulk diffusion controlled coarsening will predominate and the LSW model can be used. Figure V.13 shows the evolution of size of the chromium particles at 600°C as compared to that predicted by bulk and pipe diffusion controlled coarsening, assuming an interfacial energy of chromium particles in copper of 0.2 Jm^{-2}, a molar volume of chromium of 7.32×10^{-6} m^{3}mol^{-1} a solubility of 0.1^{at}%, and for pipe diffusion controlled coarsening the same assumptions as those used for calculating $F(r)D_{pipe}$. Close agreement can be seen with the bulk diffusion controlled model.

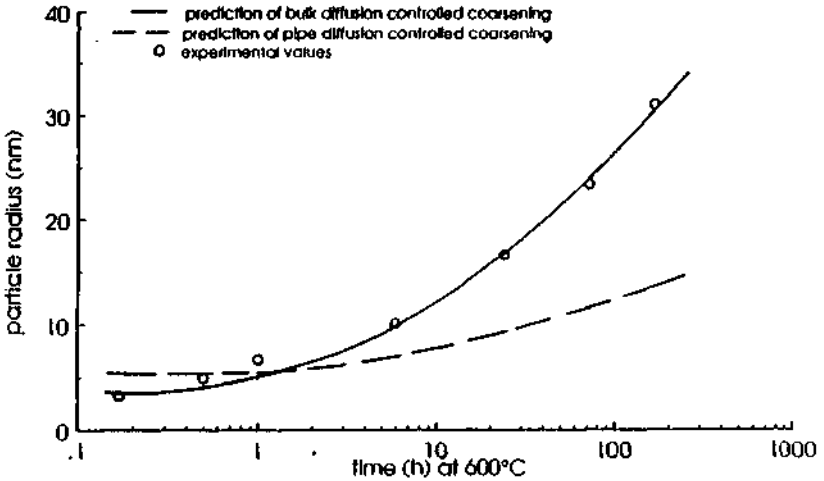

Figure V.13 Evolution of the chromium particle size at 600°C as compared to that predicted by bulk and pipe diffusion controlled coarsening models.

Figure V.14 shows a r^3-t representation for the coarsening of the chromium particles at different temperatures. Eliminating all temperature dependant terms other than the exponential term from the experimental rate constant κ_3 and plotting $\ln(\kappa_3 T/X_{\infty}(T))$ against 1/T should give a straight line of slope:

$$\frac{-\Delta H_{bulk}^{Cr}}{R} \qquad (19)$$

with an intercept of:

$$ln\left(\frac{8}{9}\frac{\gamma V_m}{R}D_o\right) \qquad (20)$$

If however, the equilibrium solubility of the rate controlling solute is not known, assuming a regular solution model, its solubility can be written as:

$$[M] = \beta\, exp\left(\frac{-\Delta H_s^M}{RT}\right) \qquad (21)$$

where [M] is the solute concentration, β a proportionality constant, equal to unity if an ideal entropy or a regular solution is assumed, and ΔH_s^M the heat of solution of the solute, M. The rate constant for bulk diffusion controlled coarsening then becomes:

$$K_3 = \frac{8}{9}\frac{\gamma V_m}{RT} D_o \beta \exp\left(\frac{-\left(\Delta H^M_{bulk} + \Delta H^M_s\right)}{RT}\right) \quad (22)$$

where the slope of the Arrhenius plot will be:

$$-\frac{Q_c}{R} = \frac{-\left(\Delta H^M_{bulk} + \Delta H^M_s\right)}{R} \quad (23)$$

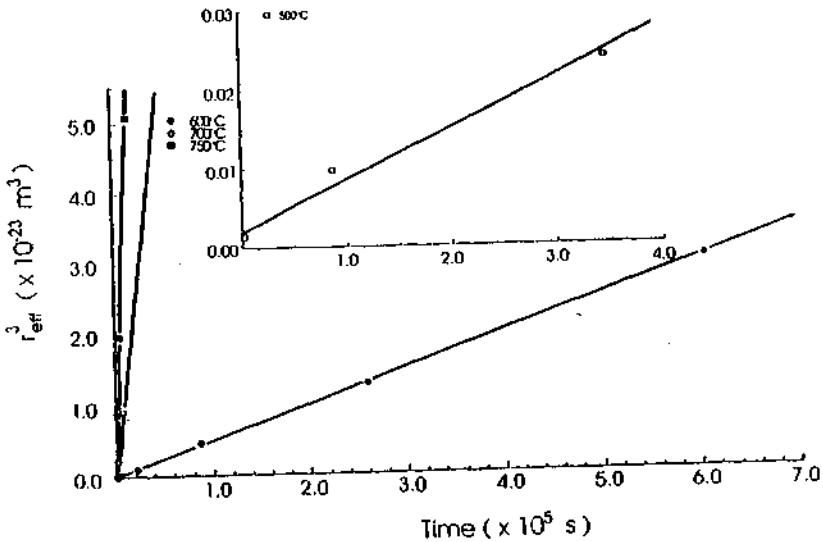

Figure V.14 r_{eff} cubed as a function of time for chromium particles in the Cu-Cr 1.85at% ribbon at various temperatures.

Sections 4.3.1 and 5.2.1.1 showed that the growth of chromium particles was unaffected by dilute additions of an extra solute. Because of the similarities in structure and composition it can be taken that chromium coarsening in the ternary chromium containing alloys was also bulk diffusion controlled. Table V.2 shows the rate constants at 600°C obtained by a r^3-t representation (figure IV.27b).

Table V.2 Coarsening rate constants (in m^3s^{-1}) at 600°C for the binary and ternary chromium-containing alloys.

Cu-Cr 1.8at%	Cu-Cr1.8at%Zrat%	Cu-Cr1.8at%Mgat%	Cu-Cr1.8at%Tiat%
4.86x10-29	2.98x10-29	2.96x10-29	3.41x10-29

If the analysis based on equations 19 and 20 is applied to the coarsening of the chromium particles in the binary as well as the ternary zirconium-containing alloy

an activation energy of, respectively, 212.5 kJmol^{-1} and 224.6 kJmol^{-1} and an intercept of 1.7x10^{-10} m^{3}s^{-1} and 7.27x10^{-10} m^{3}s^{-1} is determined (figure V.15). The values of the activation energy are in close agreement with those measured by Barreau *et al.* [154] and Saxena [155]. The virtually identical values of the activation energy for bulk diffusion of chromium in the binary and ternary alloy (as well as the similar values of the pre-exponential term) leads to the conclusion that the presence of zirconium atoms does not modify in any appreciable manner the mechanism of chromium atom transport within the copper matrix. As for the intercept, introducing the appropriate values for V_m and R gives a product of γD_o of 1-7x10^{-4} Js^{-1} which is in order of magnitude agreement with the general values of interfacial energy and diffusional pre-exponential terms.

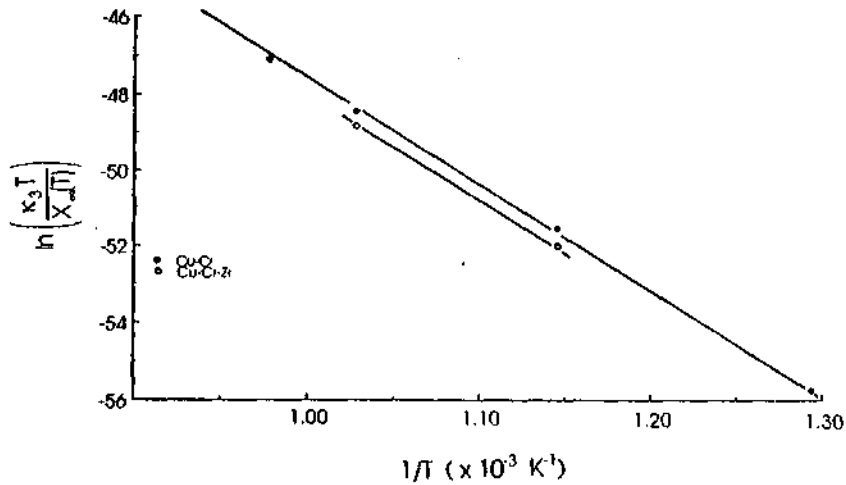

Figure V.15 Plot of $\ln(\kappa_3 T/X_\infty)$ against 1/T for chromium particles in binary and the ternary zirconium-containing alloy

5.3.1.3 Coarsening of YB_6 and Cu_6Y particles in yttrium-containing ribbons

Coarsening analysis was carried out on YB_6 particles present in the Cu-Y 0.1B^{at}%B 2.3^{at}% as well as on Cu_6Y particles in the Cu-Y0.7^{at}% alloy. The precise intermetallic phase was not determined in this study. Cubic Cu_6Y [158] is quoted as the first stable copper-rich intermetallic to form. A metastable Cu_5Y phase with a hexagonal structure has also been observed [159]. It is assumed that after annealing the equilibrium phase is obtained and that the yttrium-rich intermetallic

obtained was Cu_6Y. As shown in section 4.3.2, the as cast microstructure of the ternary alloy consisted of amorphous boron and yttrium-rich particles arranged in a cellular manner. During annealing, the initial microstructural changes were characterized by a transient period during which transformation of amorphous to crystalline boron occurred and a stable volume fraction of YB_6 particles of size 2ψ was obtained. After these initial changes the microstructure contained excess crystalline boron and YB_6 particles. Because of the composition of the dispersion the coarsening of YB_6 will be the result of the transport of both yttrium and boron atoms. By contrast the coarsening of Cu_6Y particles is determined only by the transport of yttrium atoms.

For the ternary alloy the low density of dislocations (figure IV.30) means that only bulk diffusion controlled coarsening is possible. Figure V.16 shows that the r^3-t relationship is closely followed for the coarsening of the YB_6 particles in the ternary alloy. The intercept of the r^3-t plot allows the value of ψ to be determined; the value at which steady state coarsening is considered to start. Table V.3 summarizes the values of ψ as well as the coarsening rate constants.

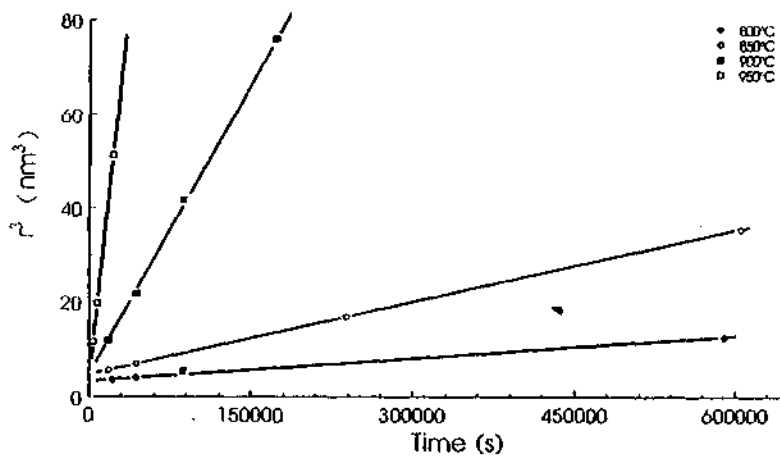

Figure V.16 r^3-t plot for the coarsening of YB_6 particles in the Cu-Y 0.18at%B 2.3at% ribbon at different temperatures

Table V.3 Coarsening of YB_6 particles in copper.

Temperature (°C)	800	850	900	950
ψ (nm)	1.5	1.7	1.7	1.6
rate constant κ_3 (m^3s^{-1})	1.49×10^{-32}	5.12×10^{-32}	4.15×10^{-31}	2.18×10^{-30}
r after 6 h (nm)	1.6	1.8	2.3	3.7

For YB_6 particles coarsening is dependent on the transport of two species, the LSW relationship is modified to

$$\kappa_3 = \frac{8}{9}\frac{\gamma V_m}{RT}\left(D_{bulk} X_\infty\right) \qquad (24)$$

where:

$$\left(D_{bulk} X_\infty\right) = \frac{D^B_{bulk} X^B_\infty \; D^Y_{bulk} X^Y_\infty}{6D^B_{bulk} X^B_\infty + D^Y_{bulk} X^Y_\infty} \qquad (25)$$

and <DX> represents the compound diffusivity-solubility of the particle in the copper matrix [160]. D^B and D^Y represent, respectively, the diffusivities of boron and yttrium in copper and X^B and X^Y, their mole fractions in equilibrium with YB_6 and excess boron. Even though the solubilities of yttrium and YB_6 in copper as well as the diffusivity of yttrium are not well known, a simple estimate and comparison with the reported solubility and diffusivity data of boron [63, 161], show that the coarsening kinetics are controlled by the concentration and diffusivity of yttrium. This conclusion is supported by the value of <DX> deduced by inserting values for γ (0.2 Jm^{-2}) and V_m ($4.2x10^{-5}$ m^3mol^{-1}) into the experimental values of κ_3: the values of <DX> are much too low for boron diffusion (table V.4). The rate constant for YB_6 coarsening can therefore be written as:

$$\kappa_3 = \frac{8}{54}\frac{\gamma V_m}{RT} D^Y_{bulk} X^Y_\infty \qquad (26)$$

Table V.4 The compound diffusivity-solubility term, <DX>, for YB_6 bulk diffusion controlled coarsening in copper.

Temperature (°C)	800	850	900	950
<DX> experimental (m^2s^{-1})	$1.06x10^{-22}$	$3.80x10^{-22}$	$3.22x10^{-21}$	$1.76x10^{-20}$
D_BX_B for boron (m^2s^{-1})	$1.5x10^{-15}$	$5.4x10^{-15}$	$1.8x10^{-14}$	$5.5x10^{-14}$

Coarsening of Cu_6Y particles was found to be much faster than that of YB_6 (figures IV.29 and IV.33). No measurement has been reported for the diffusivity of yttrium in copper. However, it has been stated [64] that rare earth elements are slow diffusers. On the basis of this assumption no clear explanation can be given for the marked difference in coarsening rates between the YB_6 and Cu_6Y particles observed in the two alloys, yttrium transport being the rate controlling element in both systems. The difference in coarsening rates seen is too large to be attributed solely to the difference in stability between YB_6 and Cu_6Y. The presence of many dislocations in the binary ribbon connecting the particles might suggest that

coarsening of the particles was not bulk, but pipe diffusion controlled. For a volume fraction of 5^{vol}% of particle and an activation energy for bulk diffusion of yttrium of 200 kJmol^{-1} (calculated by the Swalin model) the critical dislocation density at 600°C is 3x10^{15} m^{-2}. The dislocation density measured after 1 h at 600°C for the binary alloy was 3x10^{13} m^{-2}, sufficiently lower than $\rho_{crit.}$ for the coarsening of the Cu_6Y particles to be considered bulk diffusion controlled and not as might have been thought, pipe diffusion controlled. The coarsening of the Cu_6Y particles is represented by the r^3-t plot in figure V.17.

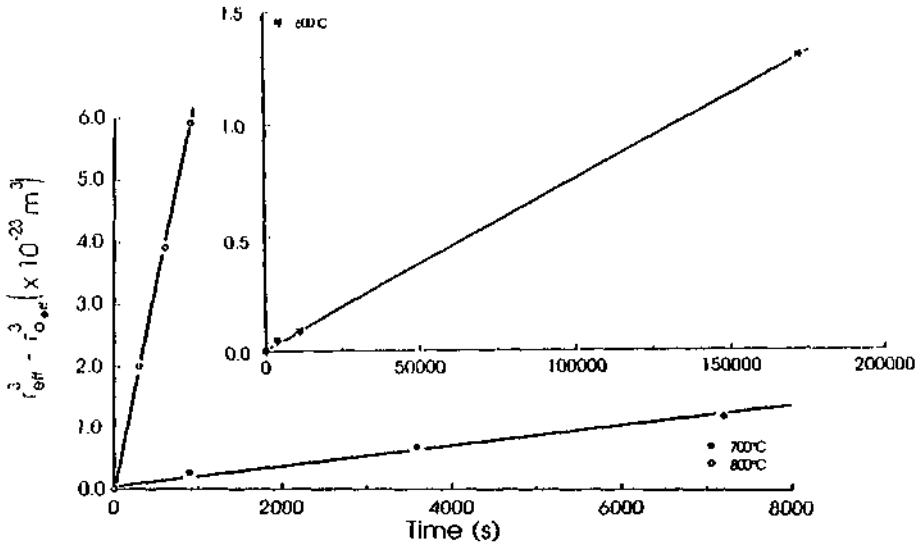

Figure V.17 r^3-t plot for the coarsening of Cu_6Y particles in the Cu-Y 0.7^{at}% ribbon at different temperatures

Plotting $\ln(\kappa_3 T)$ against $1/T$ the activation energy for coarsening will contain two terms as in equation 23, Q_c of Cu_6Y particles in copper is determined as 270 kJmol^{-1} (figure V.18). Figure V.19 shows a similar plot for the coarsening of the YB_6 particles in the ternary alloy. Q_c of YB_6 is deduced to be 410 kJmol^{-1}. For the ternary alloy the concentration of yttrium in the matrix in equilibrium with excess boron and YB_6 is not known.

Olson *et al.* [162] showed that the rate of coarsening of second phase particles can be changed by altering the composition of the alloy. If an AB dispersoid is found

in an alloy, by increasing the concentration of A in the alloy the equilibrium solubility of B is decreased by the law of mass-action. If B is rate controlling, the coarsening rate of the dispersoid can in consequence be reduced. This can be used to explain the better coarsening resistance of the YB_6 particles in the ternary alloy. The high boron concentration in the alloy forced down the equilibrium concentration of yttrium decreasing the coarsening rate of the dispersoid. In contrast to this boron-rich off-stoichiometry, the yttrium-rich off-stoichiometric ribbon showed poor thermal stability (figure IV.18).

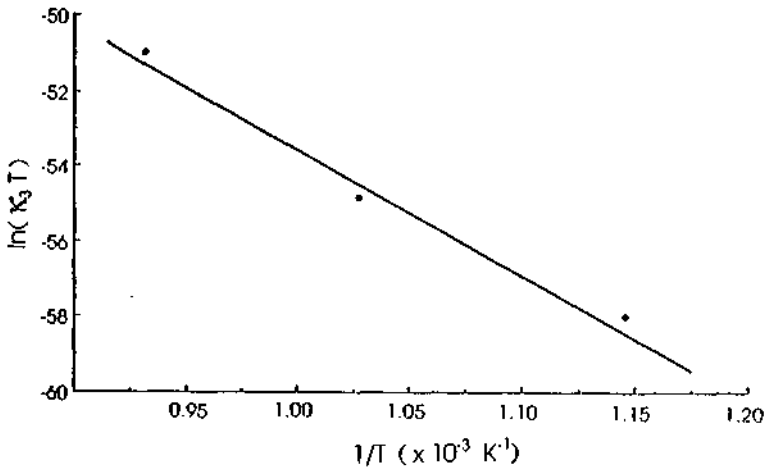

Figure V.18 ln(κ_3T) against 1/T plot for the coarsening of Cu_6Y particles.

Assuming ideal entropy of mixing and knowing the maximum solid solubilities of both boron and Cu_6Y in copper the enthalpies of solution $\Delta H_s^{Cu_6Y}$ and ΔH_s^B, of Cu_6Y and boron are calculated as 73.6 kJmol^{-1} and 62.4 kJmol^{-1} respectively. The activation energy for the coarsening of the Cu_6Y particles can therefore be written as $Q_c=\Delta H^Y_{bulk}+73.6$ kJmol^{-1} (from equation 23). Which would mean that the activation energy for bulk diffusion of yttrium, ΔH^Y_{bulk} calculated for this alloy is approximately 196 kJmol^{-1}. For the ΔH_s^Y of yttrium, the heat of formation of Cu_6Y must be known. However, no thermodynamic data on the copper-yttrium system is available. The heat of formation of YB_6 was determined by Kudinstseva *et al.* [127] as -100 kJmol^{-1}. Based on the assumption that the heat of formation is related to the melting point (the melting point of YB_6 is 2300°C and that of Cu_6Y is 910°C) the heat of formation of Cu_6Y can be neglected with respect to that of YB_6. The enthalpy of solution of YB_6 in copper following the reaction:

$$YB_6 \rightarrow \underline{Y}_{Cu} + 6\underline{B}_{Cu} \qquad (27)$$

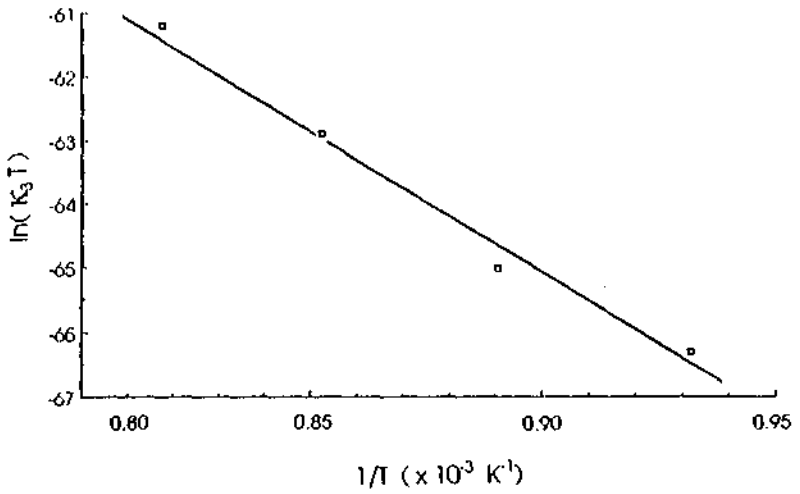

Figure V.19 ln(κ_3T) against 1/T plot for the coarsening of YB_6 particles.

can therefore be assumed to be 548 kJmol^{-1}. Hence the solubility product can be written as:

$$[Y][B]^6 = exp\left(\frac{-548\ kJmol^{-1}}{RT}\right) \qquad (28)$$

If boron is found in excess as is the case for the ternary alloy, the concentration of boron in equilibrium will be determined by the reaction B -> $\underline{B}_{Cu}$ where:

$$[B] = exp\left(\frac{-62.4\ kJmol^{-1}}{RT}\right) \qquad (29)$$

Substituting equation 29 into equation 28 gives the concentration of yttrium in equilibrium with excess boron and YB_6 as:

$$[Y] = exp\left(\frac{-173.6\ kJmol^{-1}}{RT}\right) \qquad (30)$$

This would imply that the Q_c calculated for coarsening of YB_6 can be written as $Q_c=\Delta H_Y^{bulk}+173.6$ which would mean that the ΔH_Y^{bulk} calculated for this alloy is approximately 230 kJmol^{-1}. This is in reasonable agreement with the value obtained for the binary alloy (196 kJmol^{-1}) as well as that obtained on the basis of a diffusion model developed by Swalin [56] (200 kJmol^{-1}). The large differences in coarsening rates between YB_6 and Cu_6Y particles can therefore be attributed to the

boron rich off-stoichiometry of the ternary alloy, and not to differences in coarsening mechanisms. In the light of the above findings, the thermal stability of dispersion hardened alloys can greatly be enhanced for an $A_\alpha B_\beta$ compound when: (a) the composition of the alloy is in excess of stoichiometry with respect to the faster of the two diffusing species (b) the compound has a high energy of formation (within the limits discussed in section 5.1.3) and; (c) the compound has a high β/α ratio.

5.3.1.4 Growth of boron particles in copper-boron and ternary boron-rich copper-yttrium-boron ribbons

Boron particle growth was studied in the Cu-B 2.7^{at}% and Cu-B 7.34^{at}% as well as in the boron-rich Cu-Y 0.23^{at}% B 5.66^{at}% ribbons. These ribbons were characterized by a succession of microstructural events. Initially, the amorphous particles in the as cast material showed a remarkable resistance to coarsening. Nucleation of crystalline boron particles thereafter occurred. These particles grew rapidly, draining solute from the amorphous particles and reducing their size and number. After total transformation, the crystalline particles coarsened. Thermal stability of the ternary alloy was higher than that of the binary alloys as reflected by the strengths observed after high temperature annealing (figure IV.1B) and the longer time necessary for the total transformation of amorphous to crystalline boron (figure IV.8). While not explicitly studied in the ternary alloy, no coarsening of the amorphous boron particles was seen over these longer time periods. The high-temperature stability of the binary and ternary ribbons was therefore not determined by the coarsening of the strengthening phase, as in other systems, but by the phase change that occurred. It was therefore important to understand the factors which controlled this phase change. The following paragraphs will discuss each of the above mentioned events.

This total absence of coarsening was unusual, since it was expected that, due to the small size of the boron atom, solute transport would be by interstitial diffusion resulting in rapid coarsening. Literature data on the diffusivity of boron in copper is sparse and apparently alloy dependent. The values reported by Rexer [161], used to estimate the diffusivity-solubility terms in table V.4, are based on an activation energy of 252 kJmol^{-1} and a pre-exponential term of 1.15 m^{2}s^{-1}.It should be noted that this value of activation energy is exceptionally high for interstitial diffusion, when compared to the activation energies of substitutional diffusion of chromium or yttrium (sections 5.3.1.2 and 5.3.1.3). Moreover, this value is close to the bulk diffusion activation energy of niobium (254 kJmol^{-1}) which is known to be a slow diffuser in copper. Similarly the pre-exponential term of 1.15 m^{2}s^{-1} is high with respect to generally quoted values for interstitial diffusion [63]. However, because of lack of other data, these values will be used with caution to estimate the diffusion coefficient of boron near the temperatures where they were initially measured.

The as cast microstructure of these ribbons consisted of boron particles decorating the grain boundaries as well as outlining the solidification cell structure. There was no evidence of high dislocation densities within the cell interiors although they were present along the cell boundaries. It was clearly shown in table IV.2 that no measurable change in amorphous particle size occurred during the first hours of heat treatment at 600°C or minutes at 700°C. If bulk, dislocation and grain boundary diffusion controlled coarsening models are used, this complete absence of coarsening can not be explained. Coarsening models previously discussed predict a significant change in particle size over the time-scale mentioned above, for example: (a) bulk diffusion controlled coarsening predicts a doubling of the size after 3 h at 600°C or 5 min at 700°C, (b) grain boundary controlled coarsening predicts a particle size of 1 μm after similar heat treatments and; (c) pipe diffusion controlled coarsening predicts a particle size of 200 nm.

It is therefore obvious that the rate determining step, conferring the high resistance to coarsening of the amorphous particles, is not transport of solute through the matrix, but the difficulty of solute transfer at the particle-matrix interface. Coarsening of these particles requires simultaneous boron dissolution at the particle interface, diffusion of the solute through the matrix, grain boundaries or dislocation pipes*, and re-precipitation of the solute on a growing particle. By analogy, the large crystalline boron particles which appear when heat treatment is prolonged, coarsen rapidly (table IV.2) by a combination of boron dissolution from a crystalline particle, diffusion, and re-precipitation on to another crystalline particle.

The crystalline particle growth in the ternary alloy during the transformation period can be represented by a parabolic relationship (figure V.20). At a later stage the growth rate falls. The initial stage can be taken as the diffusion controlled growth of the individual boron particles. The decay in growth rate occurs when less than 1 vol% of crystalline boron particle has formed, considerably less than the expected 2.5 vol% at the end of the phase change for the ternary alloy. The decay in growth rate can be explained by: (a) the particle size reaching the ribbon thickness and; (b) the diffusion field around each particle are beginning to interact. It is also important to note that the estimation of size of the boron crystal is only valid for small crystal sizes. As discussed in section 3.7.1, page 36, the measurement becomes erroneous for large crystals where the measurement of Φ_{max} deviates from reality as the structure of the particle becomes arborescent and the number and size of the crystal branches increases.

Growth of the crystalline phase can be considered to be the result of supersaturation where the concentration of metastable amorphous particles supposedly constitute the supersaturation. The depleted zones found in the matrix

*These are generally considered the rate determining steps of coarsening, since solute transport through the interface is usually considered rapid.

around the crystalline particles are consistent with this model (figure IV.5). Similar growth rates were observed in the binary alloys. The differences in time for the transformation to be completed between the binary and ternary systems is attributed to the differences in the number of crystalline particles formed during heat treatment.

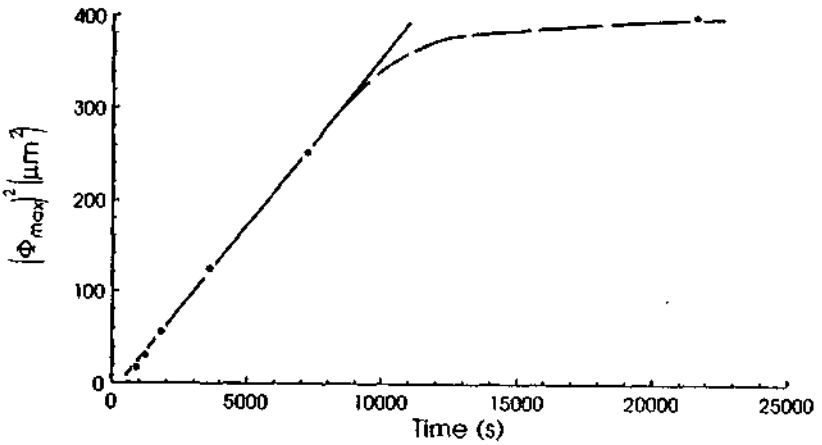

Figure V.20 Boron particle size in the Cu-Y 0.23at% B 5.66at% alloy as a function of annealing time at 750°C. The initial growth follows a parabolic size vs. time relationship.

Figure V.21 shows a TEM micrograph taken at the interface between a boron crystal and its surrounding matrix. The matrix far from the interface can be seen to contain still many amorphous boron particles. This figure also shows the depleted zone close to the crystalline boron particle, from where most of the amorphous boron has disappeared; both the size and number of amorphous particles are reduced near the crystalline phase. This micrograph was taken on the Cu-B 7.34at% sample for which the higher density of crystalline particles made it easier to find such a particle within the electron-transparent area of the thin foil. In the ternary alloy this observation would have been difficult to make because of the presence of YB_6 particles which do not alter in size during the times of this transformation, making the depleted zone less obvious. The amorphous particle size and distribution confirms that the growth of the large particles is controlled by solute diffusion from the amorphous particles distributed in the matrix.

The growth rate, dr/dt, of a particle in a saturated matrix can be described by:

$$\frac{dr}{dt} = \frac{1}{2}\frac{(X_s - X_\infty)}{(X_\beta - X_\infty)}\sqrt{\frac{D}{t}} \qquad (31)$$

where X_s is the supersaturated concentration of solute, X_∞ the equilibrium solute concentration at the temperature of heat treatment and X_β the solute concentration of the particle¶ [163]. This equation may be integrated to show the parabolic growth constant:

$$\frac{r^2}{t} = \left[\frac{(X_s - X_\infty)}{(X_\beta - X_\infty)}\right]^2 D \qquad (32)$$

Where the term in square brackets is the supersaturation. Taking logarithms gives:

$$ln\left(\frac{r^2}{t}\right) = ln\left(\left[\frac{X_s - X_\infty}{X_b - X_\infty}\right]^2 D_o\right) - \frac{Q}{RT} \qquad (33)$$

Figure V.21 represents the variation of the log of the rate constant with the reciprocal of temperature and gives an activation energy of 170 kJmol^{-1} for the transport of boron.

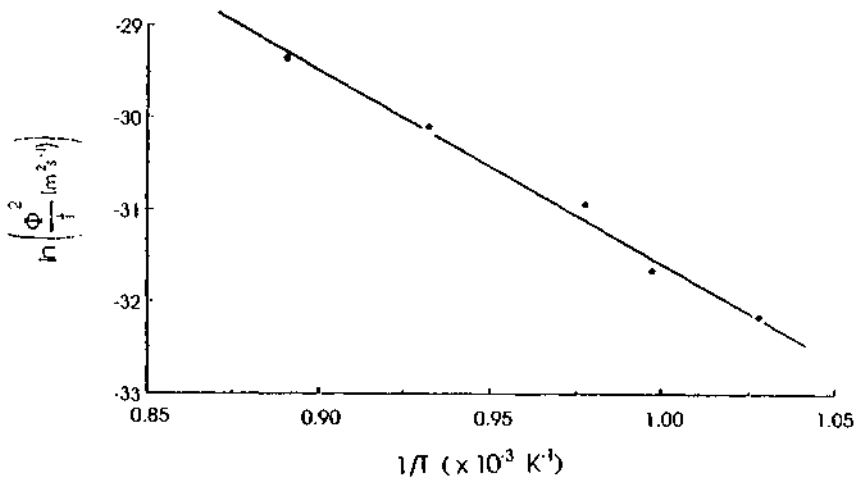

Figure V.21 Variation of growth rate (expressed as Φ^2/t) during the initial parabolic growth period, with annealing temperature for the Cu-Y 0.23^{at}% B 5.66^{at}% ribbon. The activation energy deduced is 170 kJmol^{-1}.

¶ The value of r is taken to mean the radius of a boron crystal, defined in section 3.7.2.1 as the radius of the encompassing circle $\Phi_{max}/2$ of the largest boron crystal metallographically found.

Figure V.22 shows that a concentration gradient of amorphous particles exists around each growing crystalline particle. Solute arrives to the crystalline particle by the dissolution of the amorphous ones. This step does not therefore seem to be rate determining. By comparison with slow coarsening of the amorphous particles, it is not the dissolution at the particle-matrix interface, but the re-precipitation of solute on an amorphous particle that results in the slow coarsening of the amorphous phase which was initially observed.

Figure V.22 Transmission electron micrograph of heat treated Cu-B 7.34$^{at\%}$ ribbon (20 min at 750°C). Many amorphous boron particles are present far away from the crystalline boron particle and fewer, smaller ones near the interface.

Figure V.23 shows a crystalline boron particle which consists of many branches occurring from one nucleation event. The branches look faceted but their surface remains rough suggesting that growth was not interface controlled. The arrival of solute by diffusion to the crystalline phase was therefore the rate determining step. This resulted from grain boundary, pipe or bulk diffusion. The activation energy of 170 $kJmol^{-1}$ was therefore the rate controlling transport mechanism for the growth of the crystalline particles.

The value of the intercept obtained in figure V.21 was $5x10^{-6}$ m^2s^{-1}. Taking the supersaturation (equation 33) as $2.5x10^{-2}$, based on an estimated alloy supersaturation X_s of about 5 at% (with 1 at% of boron in the YB_6 particles), together with a solid solubility X_∞ of 0.5 at% at the temperatures used and X_β equal to 100 at%, a frequency factor D_o of $8x10^{-3}$ m^2s^{-1} is obtained. This is in better agreement with the generally accepted diffusion frequency factors than the value quoted by Rexer.

The nucleation of boron crystals was examined as a function of time (table IV.2) at several temperatures in the ternary alloy. For any temperature, the volume number density of crystals remained constant; which means that growth alone occurred, and nucleation, if any, was rapid. The number of the resulting crystals varied with the annealing temperature according to an Arrhenius relationship with an activation energy of 160±50 $kJmol^{-1}$, similar to the value obtained for the transport of solute through the matrix (figure V.24). The large uncertainty in this value was due to the difficulties in measurement of particle number.

The ternary ribbon was shown to maintain good mechanical properties at temperatures up to 100°C higher than the binary ribbons. The reason for the improved thermal stability of the ternary alloy is the limited crystal nucleation occurring in this alloy when compared with the binary alloys (table IV.2). The constant number of crystalline boron particles during the transformation from amorphous to crystalline boron suggests that no nucleation takes place; only the growth of crystals at quenched-in sites. Nucleation at quenched-in sites may be temperature dependant when a distribution of sites of different activity is quenched into the ribbon during melt spinning, and if this distribution varies with quench rate. An alternative possibility, which seems more likely, is that nucleation is controlled by precipitation of the supersaturated solute of the quenched alloy. During the initial heat treatment this solute can precipitate as the equilibrium crystalline phase. Some of these precipitates will reach a size large enough to be stable relative to the metastable amorphous particles; and a distribution of stable nuclei will be created. Since more solute was retained in supersaturation near the wheel side of the ribbon, more nucleation occurred there (figure IV.7). The increase of solubility extension with wheel speed is confirmed by the increase of wheel side microhardness after peak ageing with wheel speed (figure IV.17). With higher

ribbon casting speeds, more solute remained in solution and more nuclei consequently formed. At very low wheel speeds where crystalline boron particles formed directly during solidification. Precipitation is faster and finer at higher temperatures leading to the formation of more nuclei. The lower number of boron crystals forming in the ternary alloy, as compared with the binary alloys, may be understood in terms of precipitation processes occurring. In the ternary alloy, a significant part of the excess boron solute precipitates in the form of YB_6 particles, leaving only a small amount of solute to precipitate as crystalline boron. Figure V.25.a summarizes the events occurring during transformation of amorphous to crystalline boron. Figure V.25.b schematically shows the distribution of the volume fraction of boron as a function of wheel speed. The ideal case is one where only amorphous boron particles exist in the matrix.

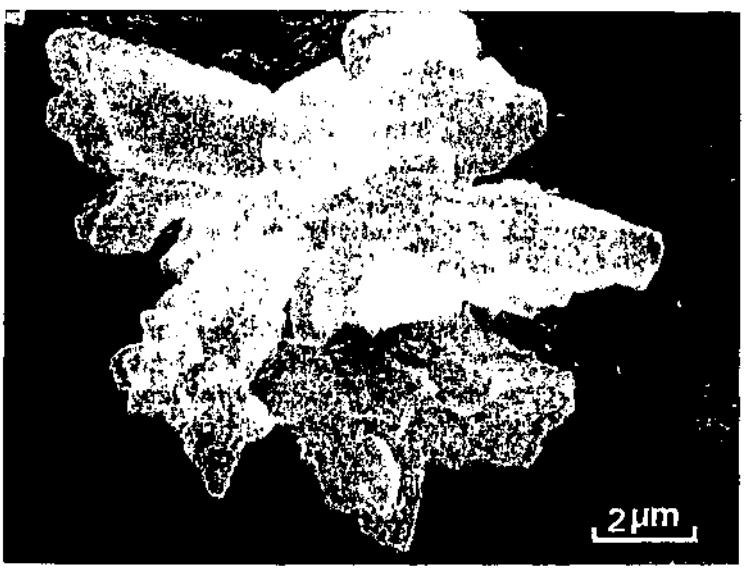

Figure V.23 Scanning electron micrograph (secondary electrons) of a boron crystal in a deeply etched sample of Cu-Y 0.23^{at}% B 5.66^{at}% (75 min at 750°C). The surface of the crystal remains rough.

Knowing the nucleation and the growth kinetics of to the crystalline particles a TTT curve can be constructed for both the binary and the ternary ribbons to underline the differences in thermal stability between the two systems. Figure V.26 shows the calculated time necessary for 50% transformation of amorphous boron in the Cu-B 7.34^{at}% and in Cu·Y 0.23^{a}% B 5.66^{at}% ribbons.

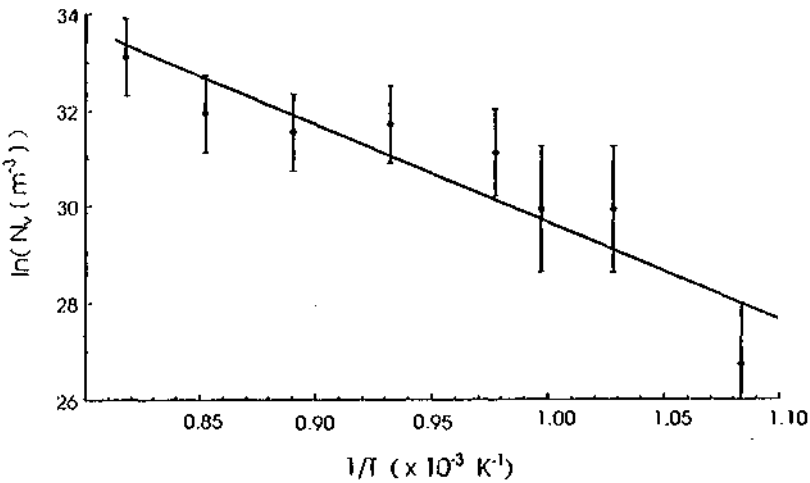

Figure V.24 Arrhenius plot of the volume number density of crystalline boron particles as a function of temperature.

After complete transformation of the amorphous boron, crystalline particles situated at the junction between several grains were found (figures IV.4, IV.5 and IV.30). Figure V.10 showed that for a large temperature range, if particles were to be found at grain boundaries, the F(r)D analysis would predict grain boundary diffusion controlled coarsening. The relation derived by Ardell [86] for grain boundary controlled coarsening is:

$$r^4 - r_0^4 = \frac{9}{32} \frac{\gamma \delta X_\infty V_m}{ABRT} D^B_{g.b.} t \qquad (34)$$

Using this relation a good fit of the experimental data is obtained for the coarsening of the crystalline boron particles in the Cu-B 7.34at% ribbon (figure V.27).

Based on the grain boundary energy being equal to the particle-matrix energy, and a fraction of grain boundary covered by particle of about 0.1, A and B are calculated as 0.2 and 1.0 respectively. With reasonable variation in physical terms it can be shown that the values vary weakly. The grain boundary diffusivity can thereby be deduced as 3×10^{-5} $m^2 s^{-1}$ and 5×10^{-5} $m^2 s^{-1}$ respectively for 750°C and 800°C.

While it may not be wise to interpret results of Arrhenius plots with only two data points, an activation energy for grain boundary diffusion is nevertheless extracted from the above data. A value of 90 $kJmol^{-1}$ representing approximately

half the value for the activation energy found for the growth and the nucleation of the crystalline particles during the amorphous transformation is found.

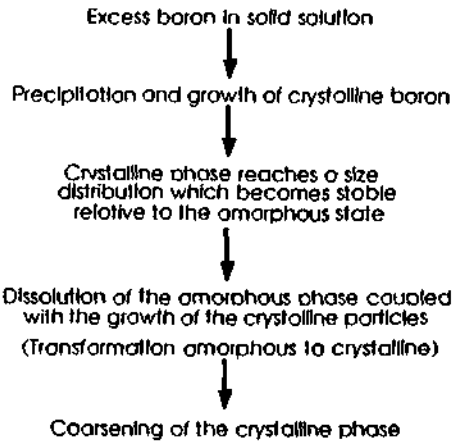

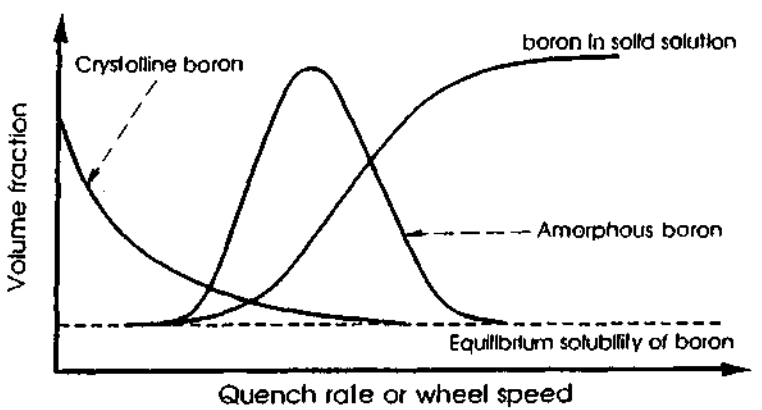

Figure V.25 Summary of the events occurring in the rapidly solidified boron-rich ribbons during annealing (a). Figure (b) shows boron solute distribution as a function of wheel speed.

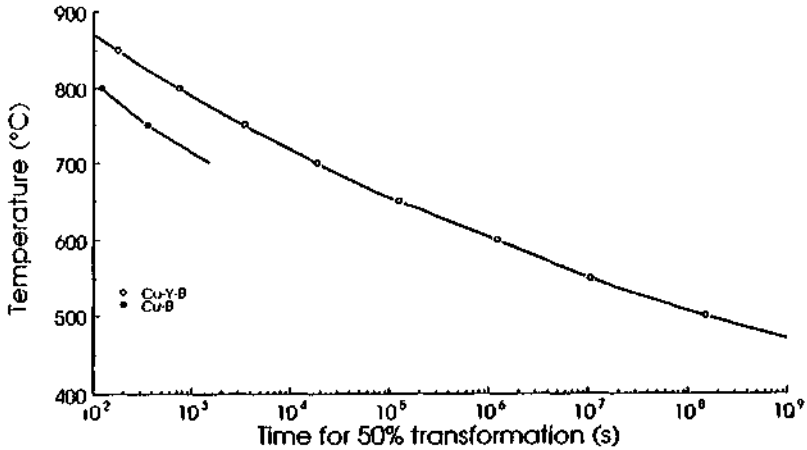

Figure V.26 TTT curve for 50% transformation of amorphous to crystalline boron in the Cu-B 7.34at% and in the boron-rich Cu-Y 0.23at% B 5.66at% ribbons. The better thermal stability of the ternary alloy is noted.

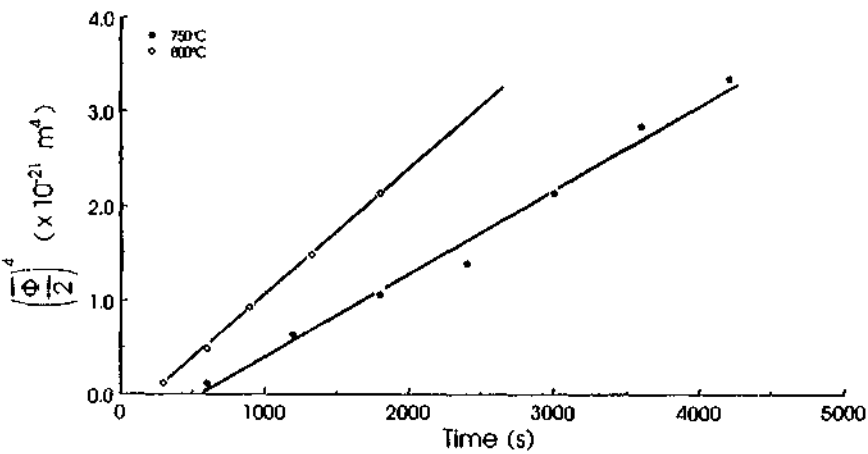

Figure V.27 r^4-t plot for the coarsening of crystalline boron particles in the Cu-B 7.34at% ribbon.

5.3.1.5 Coarsening of bimodal particle distributions

On annealing the Cu-Cr 1.85^{at}% alloy cast at a wheel speed of 8 ms^{-1} precipitation occurred resulting in a bimodal distribution of particles. Figure IV.24 showed that initially the fine precipitates coarsened independently. Further annealing resulted in the disappearance of the fine particles which initially remained with a constant volume fraction until their mean volume interparticle spacing λ_{vs} came close to the average spacing λ_{vL} of the larger particles (figure IV.25). For the coarsening of the small particles to be uneffected by the large λ_{vs} must be much smaller than λ_{vL}. This can be written as:

$$\sqrt[3]{\frac{\overline{V_s}}{f_{vs}}} << \sqrt[3]{\frac{\overline{V_L}}{f_{vL}}} \qquad (35)$$

where $\overline{V}$ is the average volume of the particles (section 3.7.2.2, page 38), f_{vs} and f_{vL} the volume fraction of small and large particles respectively.

The volume fraction and size of the small particles were measured as a function of annealing time at 500°C (figure IV.25). The small particles coarsened to 2.3 and 6.3 nm after 30 min and 24 h, respectively, which corresponded to interparticle spacing of 48 and 100 nm. The large particles (20 nm in size) had a spacing of 135 nm. After a 24 h annealing time the volume fraction of small particles decreased, the particle distribution in the alloy tending towards a single mode distribution of particles.

Coarsening of the fine particle distribution can therefore be considered to behave as expected by the coarsening models as long as the small and large particles do not interact with each other. This is the case until the fine particles have sufficiently coarsened that their spacing *i.e.* the solute transport distance, becomes equivalent to that of the large particles. At this point the differences in solubility due to differences in size is such that the smaller particles would dissolve in favour of the larger. The fine particle medium surrounding the larger particles supplies the necessary solute for growth. This may be considered similar to the growth of crystalline boron during the transformation period (section 5.3.1.4). Fine particles provide the supersaturation resulting in the growth of the large particles. This may explain the particle free zones surrounding the large inclusions in the Cu-Ni_3B ribbon (figure V.8)

In the Cu-Cr 1.85^{at}% ribbons, after complete precipitation of the chromium particles, particle free zones on either side of the grain boundary were observed. These zones (figure IV.21) increased in size with annealing time. They should be distinguished from precipitation free zones which are the result of the lack of vacancies near the grain boundaries after quenching. After several days of annealing, these particle free zones continue to grow and are therefore not the result

of these gradients. Figure V.28 shows that the width of these zones is related to the volume interparticle spacing. Considering a dissolving particle (a particle of size smaller than the critical radius), equidistant from the grain boundary and its neighboring particles in the bulk, solute would preferentially be drained towards the grain boundary than towards a growing particle in the matrix because of the higher solute solubility and the presence of larger particles at the grain boundary.

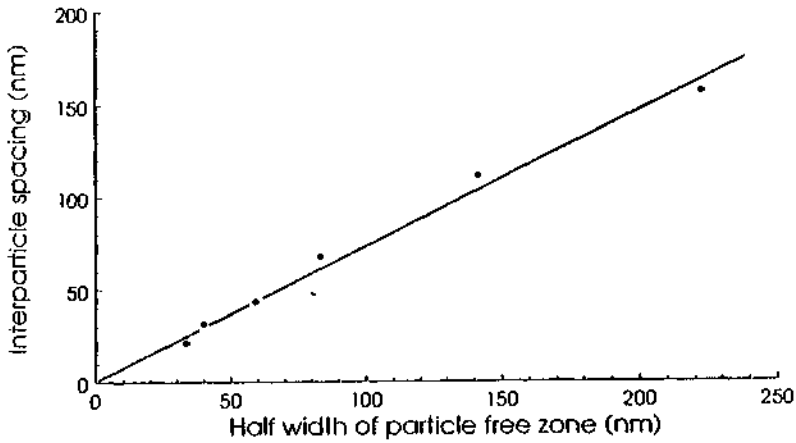

Figure V.28 Volume interparticle spacing of chromium particles as related to the width of the particle free zone.

5.3.2 Grain growth

One of the consequences of rapid solidification to be studied in this work was alloy strengthening by grain refinement. Section 5.2 showed that the increase in strength due to grain refinement for the alloys studied was small, when compared to the strength gained by fine second phase particles. During annealing the average grain size increased. Some of the ribbons studied showed slow grain growth kinetics, *e.g.* the copper-yttrium-boron ribbons, while others suffered rapid growth. These differences in kinetics were a reflection of the effectiveness of the grain boundary pinning particles in the microstructure.

The grain size of such materials is usually stabilized by grain boundary particles. Zeners' formula for the limiting grain size in the presence of second phase particles is derived by equating the pressure tending to move the grain boundary towards its centre of curvature to the retarding force produced by a second phase particle [163], thus:

$$\bar{D} = \frac{4\bar{r}}{3f_v} \qquad (36)$$

where $\bar{D}$ is the average grain diameter and $\bar{r}$ the average radius of the spherical inclusions. This equation was found to hold in many copper systems [19, 41, 47]. Under these conditions it can be seen that grain size is particle size dependent. Because of rapid grain boundary particle coarsening, pinning particles become less efficient as their size increases. This decreases the retarding force exerted by the pinning particles leaving the boundary free to migrate. The boundary will move a short distance before encountering other smaller particles which will again pin it, this pinning unpinning process results in swept up particle free zones. Figure V.29 shows this effect in two different alloys. In the Cu-Cr 1.85at% ribbon swept up zones were found after lower temperature anneals compared to the Cu-Y 0.18at%B 2.3at% ribbon, illustrating the better efficiency of YB_6 particles in grain boundary pinning, mainly due to their slower coarsening. However, in both cases the kinetics of grain boundary coarsening are much more rapid than those of bulk, permitting the grain boundary to move along by pinning and unpinning leaving behind a distribution of larger particles.

Figure V.29 Swept-up zones in Cu-Y 0.18at%B 2.3at% ribbon heat treated 48 h at 900°C (a) and Cu-Cr 1.85at% ribbon heat treated 24 h at 400°C showing the result of the unpinning-pinning of grain boundaries on the particle distribution.

In the copper-boron ribbons, before the amorphous transformation, boron particles were found only along grain boundaries and cell walls. Equation 36 should therefore be modified to consider the preferential arrangement of particles. The effective volume fraction of boundary pinning particles can be estimated knowing the grain boundary area fraction. Five hundred particles were observed per square micron of grain boundary in the columnar region of the Cu-B7.3^{at}% ribbon. Since the average particle radius was 13 nm, a critical grain size of about 0.1 μm is calculated. Smaller grains will grow to this size while larger grains will remain pinned. As the as cast grain size was 0.4 μm, it is clear that no grain growth can take place until considerable particle coarsening has occurred. It was shown that for these ribbons such growth can initially take place locally, following the crystallization of some of the amorphous boron particles (figure IV.5) where the volume fraction and the size of the amorphous pinning particles is decreased.

5.3.3 Summary

Quantification of the dislocation density or the proportion of particles situated on grain boundaries and the estimation of the F(r)D product help to understand the solute transport mode which controls coarsening. For a given temperature and volume fraction of particles, there is a critical dislocation density where higher densities favour pipe diffusion controlled particle coarsening over bulk diffusion. The combination of an estimation of $\rho_{crit.}$ and F(r)D proved to be helpful in determining the rate controlling transport path. These considerations become important when processing the rapidly solidified material, as for example during low temperature extrusion where the high dislocation density induced by deformation might promote pipe diffusion controlled coarsening.

Coarsening of chromium particles in binary Cu-Cr 1.B5^{at}% ribbon was found to be bulk diffusion controlled. The coarsening kinetics were insensitive to the presence of a third alloying element.

Yttrium was found to diffuse at a rate close to that of chromium in copper. The large differences in coarsening rates between YB_6 and Cu_6Y particles were attributed to the boron rich off-stoichiometry of the ternary alloy, and not to differences in coarsening mechanisms. It was shown that the thermal stability of dispersion hardened alloys can greatly be enhanced, for an $A_\alpha B_\beta$ compound when: (a) the composition of the alloy is in excess of stoichiometry with respect to the faster of the two diffusing species, say B, (b) the compound has a high energy of formation and; (c) the compound has a high β/α ratio.

The nature of the dispersion can greatly modify the kinetics of particle growth. Amorphous boron-rich particles were found in rapidly solidified boron-containing ribbons. The coarsening of these amorphous particles was unexpectedly slow; hindered by the difficulty of solute precipitation on the amorphous phase. Stability of these alloys was not determined by coarsening but by the transformation of the

amorphous particles. The rate of transformation was determined by the degree of solubility extension which depended on casting conditions or on ternary additions which may limit the solubility extension of the matrix.

Grain size for the rapidly solidified ribbons studied was stabilized by grain boundary pinning particles, as predicted by the Zener equation. However, because of rapid grain boundary coarsening, pinning particles become less efficient as their size increases during annealing. Their increase in size decreases the retarding force leaving the boundary free to migrate. The boundary will thereby move a short distance before encountering other smaller particles which hinder its growth. This unpinning-pinning process was observed to various degrees in most of the ribbons studied. As the grain size decreases, because of faster casting speeds or higher solute concentration, a higher volume fraction of grain boundaries will be found in the as cast material. In consequence, the proportion of particles coarsening by grain boundary diffusion will increase, leading to faster overall coarsening. Therefore from a thermal stability point of view, it would be preferable to obtain rapidly solidified materials with large grain sizes.

Grain boundaries act as solute sinks during coarsening. It was shown that solute from dissolving particles close to the boundary will preferentially drain towards grain boundary particles.

In bimodal particle distributions the coarsening of the fine particles can be considered to be unaffected by the larger particles as long as their spacing is much smaller than that of the larger particles.

CHAPTER 6
Conclusions

6. Conclusions

Rapid solidification was used to obtain microcrystalline high strength high conductivity copper alloys. Melt spinning enabled the production of small quantities of such alloys for which the microstructure, mechanical properties and thermal stability were examined. A methodology for appropriate choice of solute was established by making use of the advantages offered by rapid solidification and taking into account the requirements for conductivity, strength and thermal stability which were initially set.

The nature and distribution of the strengthening phase, casting conditions and alloy composition were all found to affect the overall quality of the alloy. The rate of microstructural and mechanical property change was found to be controlled by the transformation, precipitation and/or coarsening kinetics of the strengthening dispersion.

Melt spun ribbons of many alloys containing less than 5^{vol}% dispersion had flow strengths close to or above the 500 MPa, which was the objective. This demonstrates that rapid solidification was an interesting production method for copper alloys with high strength and conductivity. Fine particle dispersion is the result of precipitation from a metastable supersaturated solid solution or solute microsegregation. Calcium, chromium, yttrium and zirconium were used as solutes for precipitation; and boron and metal borides of nickel and yttrium, for microsegregation dispersion hardening.

Copper-chromium and zirconium ribbons, 30 μm thick, showed solubility extensions up to 2.5 and 0.3^{at}% respectively throughout the ribbon thickness The solidification rate during ribbon formation was fastest at the the wheel contact side of the ribbon. Within this region, some solubility extension of boron and yttrium was possible. For the the rest of the ribbon thickness and for high concentrations of chromium or zirconium, the ribbons were composed of a fine cellular structure, with particles decorating the cell walls and grain boundaries. Copper-chromium, cobalt and iron boride alloys showed liquid phase immiscibilities. It was suspected that the presence of boron modified the eutectic copper-metal reaction to a monotectic. Titanium and zirconium diborides were practically insoluble in liquid copper at temperatures of about 1500°C. Up to 2^{vol}% of YB_6 and 13^{vol}% of Ni_3B were finely distributed in a microsegregated cellular manner by rapid solidification. The volume fraction of dispersion was limited more by the solubility of the dispersoid in the liquid phase than by the solidification factors, which were more important in controlling the fineness of the dispersion.

The grain structure of ribbons was dependent on the wheel speed and the solidification interval of the alloy. For alloys with large solidification intervals, melt spun ribbons usually had three distinct zones and ribbon formation was momentum controlled. For small solidification intervals, the ribbons had a columnar structure and their formation was heat transfer controlled. Kinetic conditions of

solidification proved helpful for the prediction of solid solubility extension of different solutes during rapid solidification. Solutes having large $C_o^{crit.}$ showed metastable solubility extension.

Under the conditions imposed by high conductivity and by a large volume fraction of second phase particles, to be obtained by precipitation from supersaturation, it was found that the alloys were limited to those based on copper-chromium and zirconium.

The flow strength of as cast ribbons was shown to be dependant on the volume fraction of second phase and on the microstructural refinement produced by rapid solidification. The evolution of properties with temperature was directly related to the kinetics of microstructural change. The largest contribution to strengthening was due to fine particle dispersion and grain size refinement was not found to contribute significantly. Where a homogeneous distribution of particles was found, the strength could be explained by the Orowan mechanism as expected for particles which are not cut by dislocations.

Rapid solidification of boron-containing alloys resulted in the segregation of an amorphous boron-rich phase on solidification cell walls. The coarsening of these particles was unexpectedly slow and was due to the difficulty of boron precipitation on the amorphous phase. Stability of these alloys was not determined by coarsening, but by the transformation of the amorphous phase to the stable crystalline phase. The rate of transformation was determined by the degree of boron supersaturation, which depended on either casting conditions, or on ternary additions, which limited the degree of solubility extension in the matrix.

The addition of zirconium, magnesium or titanium in less than 0.3 at% to the copper-chromium alloy, modified the age hardenability of the supersaturated material. Silicon additions had no effect as expected. Upon ageing a uniform fine distribution of chromium particles was obtained where the size of the dispersion was dependent on the alloying addition. Coarsening kinetics of these particles was insensitive to the presence of the third alloying element. The activation energy of chromium bulk diffusion was unaffected by the presence of other solute atoms in the alloy, showing that the differences in mechanical properties observed during age hardening were not due to a modification of the transport mechanisms. The third element led to changes in the aspect ratio of the chromium particles during the later stages of coarsening; zirconium additions tended to keep the particles spherical, while titanium additions exaggerated the cigar-shape morphology. Additions of zirconium and magnesium modified the precipitation sequence of the supersaturated alloy. The finer particle size distribution observed at peak strength, was the result of an initial homogeneous metastable precipitation of a complex intermetallic phase. Thereafter it decomposed into bcc chromium giving a finer dispersion, in comparison to the binary alloy. Zirconium proved to be the most effective of the alloying additions increasing the maximum strength of the alloy. The

optimum zirconium concentration was close to 0.3 at%. Additions of magnesium, like zirconium, increased the peak strength of the alloy by the modification of precipitation, but its effects were lost during high temperature anneals. Titanium additions reduced the age hardenability of the ribbons to levels below the binary copper-chromium alloy. The existence of oxide particles in the as cast ribbon provoked heterogeneous nucleation of bcc chromium on these particles. Homogeneous precipitation was limited, resulting in a coarser particle size distribution at peak strength consequently reducing the strength of the material.

In microsegregated ribbons, interparticle spacing remained the most important parameter in strengthening. Particle size in these materials was larger than that in peak aged precipitation hardened ribbons. Their localization within the cell walls reduced the volume fraction of hard zones in the matrix as compared to a uniform distribution of finely precipitated particles. As a result, for the same volume fraction of dispersion, the maximum strength of precipitation hardened ribbons was considerably higher than microsegregated dispersoid hardened alloys. For the same material, the strength increased with the square root of volume fraction.

The relative importance of dislocations or grain boundaries on the coarsening of the particles was found to depend on microstructural parameters such as dislocation density, grain or particle size, and on annealing temperature. A method, based on microstructural observations, has been established to identify the transport path which dominates during coarsening. The estimation of the F(r)D term for each of the transport mechanisms enables the determination of the dominant transport mechanism. Dislocation pipe diffusion may become important for dislocation densities larger than r_{crit}. This analysis may be applicable when the microstructural changes are to be predicted under different processing conditions.

The diffusivity of yttrium was close to that of chromium in copper. Off-stoichiometric compositions of ternary alloys, rich in the element which is not rate controlling, decreases the solubility of the rate controlling element thereby increasing the stability of the alloy by decreasing the coarsening rate of the particle. The choice of dispersoid was restricted compounds with a small ΔH_f^{atom}.

Amorphous boron-rich particles were found in rapidly solidified boron-containing ribbons. These particles coarsened at a negligibly slow rate, which is believed to be due to the difficulty of interface transfer of solute. Boron dissolution from amorphous particles was rapid, but boron precipitation on the amorphous phase was slow. Stability of these alloys was determined by the transformation of the amorphous to the crystalline phase. The rate of transformation was determined by the number of boron crystals appearing during heat treatment. This number was constant over the time during transformation and depended on the degree of solubility extension of boron, itself dependant on casting conditions or on ternary additions.

In bimodal particle distributions the coarsening of the fine particles can be considered to be unaffected by larger particles as long as their volume interparticle spacing is much smaller than that of the lager particles.

Grain boundaries act as solute sinks during coarsening. During coarsening, solute from dissolving particles situated close to the boundary will preferentially be drained towards grain boundary particles than to other neighbouring particles in the bulk leaving a particle free zone on either side of the boundary.

Grain size was stabilized by grain boundary pinning particles. Rapid grain boundary coarsening of these particles reduced their effectiveness, decreased their retarding force and leaving the boundary free to migrate. A higher volume fraction of grain boundaries increases the proportion of particles that coarsen by grain boundary diffusion, leading to faster overall microstructural coarsening. As the grain size contribution to strengthening in these materials was found to negligible, it would be preferable to obtain rapidly solidified materials with larger grain size, limiting grain boundary coarsening and using more efficiently the dispersed particles. This should be taken in consideration, if possible, during choice of casting conditions or processing route.

This work has enabled the establishment of a series of guide-lines for the development of high strength high conductivity copper alloys by rapid solidification. It has demonstrated the usefulness of this technique in producing novel alloys with specific characteristics. However the use of rapid solidification requires a careful approach to processing conditions and alloy composition. It was found that many of classical metallurgical models used to explain mechanical properties and microstructural changes are applicable for rapidly solidified alloys. The importance of microstructural analysis to a localized level, and the used of these models at that level, should be emphasized in order to explain the specific metallurgical phenomenon in question.

CHAPTER 7
Bibliography

7. Bibliography

1. N.J. Grant, A. Lee and M. Lou, in *High Conductivity Copper and Aluminium Alloys*, ed. E. Ling and P.W. Taubenblat, (proc. conf.), Metall. Soc. AIME, N.Y., 1985, p.103
2. W.C. Shumay, Jr., *Advanced Materials and Processes*, **12**, 1987, p.55
3. P.W. Taubenblat, in *Copper and Copper Alloys for Fusion Reactor Application*, ed. F.W. Wiffen and R.E. Gold, (proc. conf.), Oakridge National Lab, TN, USA, 1984, p.130
4. A. Caruvana, W.H. Day, G.A. Cincotta and R.S. Rose, *Systems Status of the Water-Cooled Gas Turbine for High Temperature Turbine Technology Program*, ASME Soc. paper 79-GT-39, 1979, quoted by 1
5. W.K. Kelley, J.W. Dini and C.M. Logan, *Plating and Finishing*, March, 1982, p.54
6. D.J. Chakrabarti and D.E. Laughlin, *Bull. Alloy Phase Diagrams*, **5**, 1984, p.59
7. H. Suzuki and M. Kanno, *J. Jap. Inst. Met.*, **36**, 1972, p.13
8. R.O. Williams, *Trans. ASM*, **52**, 1959, p.530
9. H. Suzuki and M. Kanno, *J. Jap. Inst. Met.*, **35**, 1970, p.434
10. N.Y. Tang, D.M.R. Taplin and G.L. Dunlop, *Mater. Sci. Tech.*, **1**, 1985, p.270
11. M. Kanno, *Z. Metallkde.*, **10**, 1988, p.687
12. H. Suzuki, M. Kanno and H. Kitano, *J. Jap. Inst. Met.*, **36**, 1972, p.363
13. M.J. Saarivirta, *Trans. ASM.*, **55**, 1962, p.531
14. H. Suzuki, M. Kanno and I. Kawakatsu, *J. Jap. Inst. Met.*, **53**, 1969, p.628
15. V.K. Sarin and N.J. Grant, *Powder Met. Int.*, **11**, 1979, p.153
16. P.W. Taubenblat, W.R. Opie and Y.T. Hsu, *Met. Eng. Quarterly*, Nov,1972, p.41
17. M.A. Morris and D.G. Morris, *Acta Metall.*, **35**, 1987, p.2511
18. M.J. Tenwick and H.A. Davies, *Mater. Sci. Eng.*, **98**, 1988, p.543
19. D.G. Morris and M.A. Morris, *Mater. Sci. Eng.*, **104**, 1988, p.201
20. V.K. Sarin and N.J. Grant, *Met. Trans.*, **3**, 1972, p.875
21. *Binary Alloy Phase Diagrams*, ed.-in chief T.B. Massalski, ASM, Metals Park, Ohio, 1986
22. L. Arnberg, U. Backmark, N. Backström and J. Lange, *Mater. Sci. Eng.*, **83**, 1986, p.115

23. M. Blank, C Caesar and U. Koster, in *Rapidly Quenched Metals*, eds. S. Steeb and H. Warlimont, Elsevier Sci. Pub., 1, 1985, p.883

24. M.J. Saarivirta and P.W. Taubenblat, *Trans. Metall. Soc. AIME*, **218**, 1960, p.935

25. M.J. Saarivirta, *Trans. Metall. Soc. AIME*, **218**, 1960, p.431

26. V.A. Phillips, *Metallography*, **7**, 1974, p.137

27. J.A. Cheng, A. Lawley and A.J. Hickl, in *Progress in Powder Metallurgy*, vol. 42, Compiled by E.A. Carlson and G. Gaines, Proceedings of the 1986 Annual Powder Metallurgy Conference, Prinston, NJ, USA, 1986, p.517

28. R.P. Singh and A. Lawley, in *Modern Development in Powder Metallurgy*, vol. 19, Compiled by P.U. Gumeson and D.A. Gustafson, Proceedings of the 1988 International powder metallurgy conference, Orlando USA

29. Y. Nishi, H. Aoyagi, T. Suzuki and E. Yajima, in *Rapidly Quenched Metals IV* (Proc. Conf.), Eds. T. Masumoto and K. Suzuki, The Jap. Inst. Met., Sendai, Japan, **2**, 1982, p.1597

30. Y. Nishi, H. Aoyagi, T. Suzuki and E. Yajima, *Trans. J. Jap. Inst. Met.*, **23**, 1982, p.703

31. U. Kösler and C. Caesar, in *Rapidly Solidified Metastable Materials*, MRS Proc., Eds. B.H. Kear and B.C. Giessen, Elsevier Sci. Pub. Co., **28**, 1984, p.419

32. I.E. Anderson, K.M. Rusin, B.B. Rath, in *Rapid Solidification Processing-Principles and Technologies IV.*, eds. R. Mehrabian and P.A. Parish, Claitors Pub., USA, 1988, p.114

33. W. Klement Jr., *Trans. Metall. Soc. AIME*, **227**, 1963, p.965

34. W. Klement Jr., *Trans. Metall. Soc. AIME*, **233**, 1965, p.1180

35. J.V. Wood and C.J. Elvidge, *Mater. Res. Soc. Symp. Proc.*, **58**, 1986, p.451

36. W.F. Schilling and N.J. Grant, *Met. Trans.*, **3**, 1970, p.2205

37. F.N. Rhines, *Trans. AIME*, **137**, 1940, p.246

38. A.V. Nakarni, in *High Conductivity Copper and Aluminium Alloys* , ed. E. Ling and P.W. Taubenblat, (proc. conf.), Metall. Soc. AIME, N.Y., 1985, p.77

39. J.H. Swisher and E.O. Fuch, *J. Inst. Met.*, **98**, 1970, p.129

40. O. Preston and N.J. Grant, *Trans. Metall. Soc. AIME.*, **221**, 1961, p.164

41. M.A. Morris and D.G. Morris, *Acta Metall.*, **36**, 1988, p.1187

42. D.L. Ellis, G.M. Michal and N.W. Orth, *Scripta Metall. Mater.*, **24**, 1990, p.885

43. R.H. Cookey and J.V. Wood, *Int. J. Rapid Solidification*, **3**, 1987, p.319

44. V. Panchanathan, In *Rapidly Solidified Metastable Materials*, MRS Proc., Eds. B.H. Kear and B.C. Giessen, Elsevier Sci. Pub. Co., **28**, 1984, p.431

45. Y.V. Yefinov, E.M. Savitsky, T.M. Frolova, G.G. Muchin and L.A. Ryabtsev, *J. Less-Common Met.*, **92**, 1984, p.271

46. K.M. Zwilsky and N.J. Grant, *Trans. Metall. Soc. AIME*, **221**, 1961, p.371

47. M.A. Morris and D.G. Morris, *Mater. Sci. Eng.*, **111**, 1989, p.115

48. M.A. Morris and D.G. Morris, in *Proceedings 7th International BNF Conference on "The Materials Revolution Through The 90's"*, Oxford, BNF Publication, Wantage, England, 1989

49. D.G. Morris and M.A. Morris, *Scripta Metall. Mater.*, **24**, 1990, p.1701

50. G. Manfré, G. Servi and C. Ruffino, *J. Mater. Sci.*, **9**, 1974, p.74

51. P.W. Taubenblat, W.E. Smith and A.R. Graviano, in *High Conductivity Copper and Aluminium Alloys* , ed. E. Ling and P.W. Taubenblat, (proc. conf.), Metall. Soc. AIME, N.Y., 1985, p.19

52. J.D. Verhoven, W.A. Spitzig, F.A. Schmidt, P.D. Krotz and E.D. Gibson, *J. Mater. Sci.*, **24**, 1989, p.1015

53. K. Schroder, in *High Conductivity Copper and Aluminium Alloys* , ed. E. Ling and P.W. Taubenblat, (proc. conf.), Metall. Soc. AIME, N.Y., 1985, p.1

54. *Niedriglegierte Kupferlegierungen*, ed. K. Eichhorn, Deutsches Kupfer Institut, Berlin, Germany, 1966

55. C. Zener, *J. Appl. Phys.*, **22**, 1951, p.372

56. R.A. Swalin, *Acta Metall.*, **5**, 1957, p.443

57. D. Turnbull and R.E. Hoffmann, *Acta Metall.*, **7**, 1959, p.407

58. D. Lazarus, *Phys. Rev.*, **93**, 1954, p.973

59. A.D. LeClaire, *Phil. Mag.*, **7**, 1962, p.141

60. G. Neumann and W. Hirschwald, *Phys. Stat. Sol.*, **55**, 1973, p.99

61. G. Neumann and D.L. Beke, *Z. Metallkde.*, **80**, 1989, p.235

62. C.J. Smithells, *Metals Reference Book*, 6th edition, ed. E.A. Brandes, Butterworths, London, 1983

63. D.B. Butrymowics, *Diffusion Rate Data and Mass Transport Phenomena for Copper Systems*, vol.1, INCRA Series on the Metallurgy of Copper, Washington DC, 1977

64. S. Badrinarayanan and H.B. Mathur, *Indian J. Pure Appl. Phys.*, 8, 1970, p.324

65. J.C. Baker and J.W. Cahn, in *Solidification*, ASM, Metals Park, OH, 1971, p.23

66. H. Jones, *Rep. Prog. Phys.*, **36**, 1973, p.1425

67. W.J. Boettinger and S.R. Coriell, in *Science and Technology of the Undercooled Melt*, eds. P.R. Sahm, H. Jones and C.M. Adam, NATO ASI Series no.14, Martinus Nijhoff Pub., Dordrecht, 1986, p.81

68. S.R. Coriell and R.F. Sekerka, in *Rapid Solidification Processing, Principles and Technologies*, eds. R.Mehrabian, B.H. Kear and M. Cohen, Claitor, Baton Rouge, USA, 1980, p.35

69. K.A. Jackson, G.H. Gilmer and H.J. Leamy, in *Laser and Electron Beam Processing of Materials*, eds. C.W. White and P.S. Peercy, Acad. Press, N.Y., USA, 1980, p.104

70. W.W. Mullins and R.F. Sekerka, *J. Appl. Phys.*, **35**, 1964, p.444

71. M.J. Aziz, *J. Appl. Phys.*, **53**, 1982, p.1158

72. W. Kurz and R. Trivedi, in *Principles of Solidification and Materials Processing*, **1**, Eds. R. Trivedi, J.A. Sekhar and J. Mazumdar, Trans. Tech. Pub., Aedermannsdorf, Switzerland, 1990, p.67

73. H. Jones, *Mater. let.*, **6**, 1988, p.181

74. M. Greumond, *Thesis no. 885*, EPFL, Switzerland

75. B. Post, in *Refractory Binary Borides, Boron, Metallo-Boron Compounds and Boranes*, ed. R.M. Adams, Wiley Interscience, N.Y., 1964

76. U.F. Kocks, *Phil. Mag.*, **13**, 1966, p.541

77. U.F. Kocks, *Met. Trans.*, **1**, 1970, p.1121

78. A.H. Chokshi, A. Rosen, J. Karch and H. Gleiter, *Scrita Metall.*, **23**, 1989, p.1679

79. R.T. DeHoff, *Acta Metall.*, **32**, 1984, p.43

80. W.W. Mullins and J. Viñals, *Acta Metall.*, **37**, 1989, p.991

81. G.W. Greenwood, *Acta Metall.*, **4**, 1956, p.243

82. I.M. Lifshitz and V.V. Slyozov, *J. Phys. Chem. Solids*, **19**, 1961, p.35

83. C. Wagner, *Z. Elektrochemie*, **65**, 1961, p.581

84. J. Crank, in *The mathematics of Diffusion*, 2nd ed., Clarendon Press, Oxford, 1975

85. K. Tsumuraya and Y. Miyata, *Acta Metall.*, **31**, 1983, p.437

86. A.J. Ardell, *Acta Metall.*, **20**, 1972, p.61

87. R. Asimov, *Acta Metall.*, **11**, 1963, p.71

88. C.K.L. Davies, P. Nash and R.N. Stevens, *Acta Metall.*, **28**, 1980, p.179

89. A.D. Brailsford and P. Wynblatt, *Acta Metall.*, **27**, 1979, p.489

90. P.Régnier, *Acta Metall.*, **30**, 1982, p.193

91. P.W. Voorhees and M.E. Glicksman, *Acta Metall.*, **32**, 1984, p.2001

92. P.W. Voorhees and M.E. Glicksman, *Acta Metall.*, **32**, 1984, p.2013

93. P.W. Voorhees and R.J. Schaefer, *Acta Metall.*, **35**, 1987, p.327

94. Y. Enomoto, K. Kawasaki and M. Tokuyama, *Acta Metall.*, **35**, 1987, p.907

95. Y. Enomoto, K. Kawasaki and M. Tokuyama, *Acta Metall.*, **35**, 1987, p.915

96. C.S. Jyaanth and P. Nash, *J. Mater. Sci.*, **24**, 1989, p.3041

97. A.J. Ardell, *J. Phys. Chem. Solids*, **27**, 1966, p.1793

98. P.K. Rastogi and A.J. Ardell, *Acta Metall.*, **19**, 1971, p.321

99. K. Mahalingam, B.P. Gu, G.L. Liedl and T.H. Sander Jr., *Acta Metall.*, **35**, 1987, p.483

100. A.J. Ardell, *Scripta Metall. Mater.*, **24**, 1990, p.343

101. M.V. Speight, *Acta Metall.*, **16**, 1968, p.133

102. H.O.K. Kirchner, *Met. Trans.*, **2**, 1971, p.2861

103. A.J. Ardell, *Acta Metall.*, **20**, 1972, p.601

104. H. Kreye, *Z. Metallkde.*, **61**, 1970, p.108

105. A.J.B. Vincent, B.P. Bewlay, B. Cantor, R.J. Zabala, R.P. LaForce, C. Huang and L.A. Johnson, *J. Mater. Sci. Let.*, **6**, 1987, p.121

106. B.P. Bewlay and B. Cantor, *Int. J. Rapid Solidification*, **2**, 1986, p.107

107. E. Vogt and G. Frommeyer, in *Rapidly Quenched Metals*, eds. S. Steeb and H. Warlimont, 1985, Elsevier Sci. Pub., Amsterdam, 1985, p.63

108. E. Vogt and G. Frommeyer, *Z. Metallkde.*, **78**, 1987, p.262

109. Z. Sun and H.A. Davies, *Mater. Sci. Eng.*, **98**, 1988, p.71

110. S. Kavesh, in *Metallic Glasses*, ASM, Metals Park, Ohio, USA, 1976

111. D. Pavuna, *J. Mater. Sci.*, **16**, 1981, p.2419

112. H.H. Liebermann, *Mater. Sci. Eng.*, **43**, 1980, p.203

113. J.M. Robertson, M. Brouha, H.H. Stel and A.J.C. Van der Borts, in *Rapidly Quenched Metals*, eds. S. Steeb and H. Warlimont, 1985, Elsevier Sci. Pub., Amsterdam, 1985, p.79

114. Å. Östland and R. West, *Int. J. Rapid Solidification*, **3**, 1988, p.177

115. K.C. Thompson-Russel and J.W. Edington, in *Practical Electron Microscopy in Materials, Electron Microscope Specimen Preperation Techniques in Material Science*, Monograph 5, Macmillan Philips Technical Library, London, 1977

116. S.E. Kisakurek, *Metallography*, **19**, 1986, p.19

117. P. Stadelmann EMS program, I2M, EPFL, Switzerland

118. R.T. DeHoff and F.N. Rhines, in *Quantitative Microscopy*, McGraw-Hill Series in Materials Science and Engineering, NY, 1968

119. P. Hirsch, A. Howie, R.B. Nicholson, D.W. Pashley and M.J. Whelan, *Electron Microscopy of Thin Crystals*, R.E. Krieger Pub. Co., Florida, USA, 1977

120. E. Ludscheider and H. Reimann, *Monatshefte für Chemie*, **108**, 1977, p.1005

121. H.A. Calderon, M.E. Fine and J.R. Weertman, *Met. Trans.*, **19**, 1988, p.1135

122. R.K. Wyss and R.E. Sanders Jr., *Met. Trans.*, **19**, 1988, p.2523

123. A. Sodergren and D.J. Lloyd, *Acta Matall.*, **36**, 1988, p.2107

124. T.H. Sanders Jr. and K. Welpmann, *Mater. Sci. Eng.*, **76**, 1985, p.147

125. U. Dahmen, M.J. Witcomb and K.H. Westmacott, *Scripta Metall.*, **22**, 1988, p.1867

126. M.G. Hall, H.I. Aaronson and K.R. Kinsma, *Surf. Sci.*, **31**, 1972, p.257

127. G.A. Kudinstseva, M.D. Poliakova, G.V. Samsonov and B.M. Tsarev, *Fiz. Metal Metalloved.*, **6**, 1958, p.272

128. P. Villars and L.D. Calvert, in *Pearsons' Handbook of Crystallographic Data for Intermetallic Phases*, Volume 2, ASM, Metals Park, OH., 1988

129. B. Callmer, L. Tergenius and J.O. Thomas, *J. Sol. Stat. Chem.*, **26**, 1978, p.275

130. J.O. Carlson and T. Ludndström, *J. Less-Common Met.*, **22**, 1970, p.317

131. S. Andersson and B. Callmer, *J. Sol. Stat. Chem.*, **10**, 1974, p.219

132. I. Higashi, T. Sakurai and T.A. Toda, *J. Less-Common Met.*, **45**, 1976, p.283

133. R.F. Bomagala, J.J. Rauch, *Trans. ASM*, **53**, 1961, p.137

134. K.H. Buschow and A.S. Van der Goot, *J. Less-Common Met.*, **20**, 1970, p.309

135. K. Jansson and M. Nygren, *J. Less-Common Met.*, **128**, 1987, p.319

136. K. Emmerich, in *Rapidly Quenched Metals*, eds. S. Steeb and H. Warlimont, 1985, Elsevier Sci. Pub., Amsterdam, 1985, p.71

137. H.A. Davies, in *Rapidly Quenched Metals*, eds. S. Steeb and H. Warlimont, 1985, Elsevier Sci. Pub., Amsterdam, 1985, p.101

138. H.Mühlbach, g. Stephani, R. Sellger and H. Fiedler, *Int. J. Rapid Solidification*, **3**, 1987, p.83

139. L. Gránásy, *Trans. Jap. Inst. Met.*, **27**, 1986, p.51

140. L. Gránásy and Gy. Mészáros, in *Rapidly Quenched Metals*, eds. S. Steeb and H. Warlimont, 1985, Elsevier Sci. Pub., Amsterdam, 1985, p.75

141. T.W. Clyne, *Met. Trans.*, **15B**, 1984, p.369

142. H.H. Liebermann, R.E. Maxwell, R.W. Smashey and J.L. Walter, *Met. Trans.*, **14**, 1983, p.1817

143. R. Willnecker, D.M. Herlach and B. Feuerbacher, *J. Appl. Phys. Lett.*, **56**, 1990, p.324

144. L. Darken and R. Gurry, in *Physical Chemistry of Metals*, McGraw-Hill, NY, 1953, p.86

145. H. Jones, *Phil. Mag.*, **61**, 1990, p.487

146. K.C. Russel, F.H. Froes and Y-W. Kim, in *Principles of Solidification and Materials Processing*, **1**, Eds. R. Trivedi, J.A. Sekhar and J. Mazumdar, Trans. Tech. Pub., Aedermannsdorf, Switzerland, 1990, p.274

147. A.R. Miedema, P.F. de Châtel and F.R. de Boer, *Physica*, **B100**, 1980, p.1

148. J.A. Alonso, J.M. López, S. Simozar and L.A. Girifalco, *Acta Metall.*, **30**, 1982, p.105

149. W. Kurz and D.J. Fisher, in *Fundementals of Solidification*, 3rd ed., Trans. Tech. Pub., Aedermannsdorf, Switzerland, 1989

150. J.D. Verhoeven, E.D. Gibson, *J. Mater. Sci.*, **13**, 1978, p.1576

151. E. Siedschlag, *Z. Anorg. Chem.*, **131**, 1923, p.173

152. O.J. Kleppa and S. Sato, *J. Chem. Thermodynamics*, **14**, 1982, p.133

153. G.C. Weatherly, P. Humble and D. Borland, *Acta Metall.*, **27**, 1979, p.1815

154. G. Barreau, G. Brunel and G. Cizeron, *C. R. Acad. Sc. Paris*, **272**, 1971, p.618

155. M.C. Saxena, *Trans. Indian Inst. Met.*, Dec. 1970, p.56

156. N.A. Gjostein, in *Diffusion*, ASM, Metals Park, Ohio, 1974, p.241

157. V.V. Slyozov, V.V. Sagalovich and L.V. Tanatarov, *J. Phys. Chem. Solids*, **39**, 1977, p.705

158. D.J. Chakrabarti and D.E. Laughlin, *Bull. Alloy Phase Diagrams*, **2**, 1981, p.315

159. K.H.J. Buschow and A.S. Van der Goot, *Acta Cryst.*, **27**, 1971, p.1085

160. S.K. Bhattacharyya and K.C. Russell, *Met. Trans.*, **3**, 1972, p.2195

161. J. Rexer, *Z. Metallkd.*, **63**, 1972, p.745

162. G.B. Olson, H.C. Ling, J.S. Montgomery, J.B. Van der Sande and M. Cohen, in *Rapidly Solidified Amorphous and Crystalline Alloys*, MRS Proc., Eds. B.H. Kear and B.C. Giessen, Elsevier Sci. Pub. Co., **28**, 1984, p.355

163. D.A. Porter and E. Easterling, in *Phase Transformations in Metals and Alloys*, Van Nostrand Reinhold, N.Y., 1981.

Annex 1

Calculation of the effective radius of coarsening based on Wagners definition of r_{eff} [83] for cigar-shaped particles

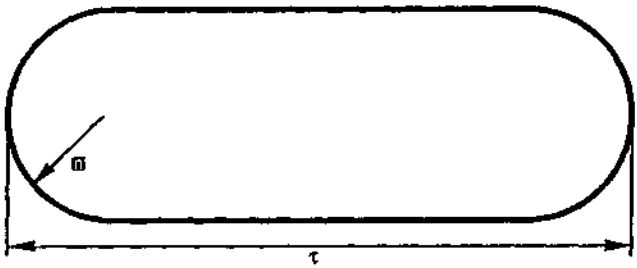

$$r_{eff} = 2\frac{dV}{dS}$$

Where V is the volume and S the surface area of the particle, all other parameters are defined by the above figure. For the surface area:

$$S = 2\pi\varpi(\tau - 2\varpi) + 4\pi\varpi^2 = 2\pi\varpi\tau$$

and for the volume:

$$V = \frac{4}{3}\pi\varpi^3 + \pi\varpi^2(\tau - 2\varpi) = \pi\varpi^2\tau - \frac{2}{3}\pi\varpi^3$$

Deriving the above equations:

$$dS = 2\pi\varpi d\tau + 2\pi\tau d\varpi = 2\pi(\varpi d\tau + \tau d\varpi)$$

and

$$dV = \pi\varpi^2 d\tau + 2\pi\varpi\tau d\tau - 2\pi\varpi^2 d\varpi = \pi\varpi^2 d\tau + 2\pi\varpi(\tau - \varpi)d\varpi$$

Dividing dV by dS gives:

$$\frac{dV}{dS} = \frac{\pi\varpi^2 d\tau + 2\pi\varpi(\tau - \varpi)d\varpi}{2\pi(\varpi d\tau + \tau d\varpi)} = \frac{\varpi^2\frac{d\tau}{d\varpi} + 2\varpi(\tau - \varpi)}{2\left(\tau + \varpi\frac{d\tau}{d\varpi}\right)}$$

Since $2\varpi\upsilon = \tau$ deriving gives $\frac{d\tau}{d\varpi} = 2\upsilon$ and substituting:

$$\frac{dV}{dS} = \frac{\varpi^2 2\upsilon + 2\varpi(\tau - \varpi)}{2(\tau + \varpi 2\upsilon)}$$

Therefore $$2\frac{dV}{dS} = r_{eff} = \frac{\varpi(3\tau - 2\varpi)}{2\tau} = \frac{\varpi(3\upsilon - 1)}{2\upsilon}$$

Acknowledgments

I would like to acknowledge:
Prof. D.G. Morris for the subject of the thesis, his help, the stimulatin discussions and the provision of research facilities that allowed me to carr out this work;
Prof. W. Form for having welcomed me in his institute;
Prof. M.A. Morris for the time and energy she spent teaching me the art an science of electron microscopy;
the "Commission d'Encouragement pour la Recherche Scientifique" (CERS for financial assistance in projects CERS/629/1474; and
the "Usines Métallurgiques Suisses" (U.M.S.) - previously "Boillat S.A." fo partial financial support and for their interest, particularly Dr. J. Flach.
Furthermore, I would also like to thank, P. A. Girard for help with the image analyses, P. Dubois for his technical assistance and the members of the Institute of Structural Metallurgy, not only for their collaboration and help, but also for their moral support.
Finally, the jury: Prof. W. Benoit, Prof. W. Form, Prof. B. Ilschner, Dr. P. Isler and Prof. D. G. Morris are thanked.